Radio Propagation for Localization and Motion Tracking In Three Body Area Network Applications

by

Yishuang Geng

A Dissertation

Submitted to the Faculty

of the

WORCESTER POLYTECHNIC INSTITUTE

In partial fulfillment of the requirements for the

Degree of Doctor of Philosophy

in

Electrical and Computer Engineering

by

September 2016

APPROVED:

Professor Kaveh Pahlavan, Major Dissertation Advisor

Professor Yehia Massoud, Head of Department

Abstract

Precise and accurate localization and motion classification is an emerging fundamental areas for scientific research and engineering developments. Such science and technology began from the broad out door area applications, and gradually grew into smaller and more complicated in-door area and more recently it is proceeding into in-body area networking for medical applications.

Localization and motion classification technologies have their own specific challenges depending on the application and environment, which are left for scientists and engineers to overcome. One major challenge is that location estimation and motion classification often use hand-held devices or wearable sensors. Such devices and sensors usually work in indoor, near body environments and the human object has certain effects on the measurements. In that situation, existing mathematical models for general environments are no longer accurate and new models and analytical approaches are required to deal with the human body effects. This has opened opportunities for researchers to tackle a number of demanding problems.

This dissertation focuses on three novel problems in localization and motion classification using radio propagation (RF) modeling, in and around the human body. (1) We develop an empirical Time-of-Arrival (TOA) ranging error model for radio propagation from body-mounted sensors to external access points, for human body tracking in indoor environment. This model reflects the effects of human angular motion on TOA ranging estimation, which enables accurate analysis for conventional TOA-based human tracking systems. (2) We use empirical data collected from a RF connection between a pair of body-mounted sensors to classify seven frequently appeared human body motions. This RF based classification approach has enabled

health monitoring applications for first responders, hospital patient, and elderly care centers and in most of the situations it can replace the costly video base monitoring systems. (3) We use radio propagation models from body-mounted sensor to medical implants and the moving pattern of micro-robots inside the body to analyze the accuracy of hybrid localization inside the human body. This analysis demonstrates the feasibility of millimeter level of accurate localization inside the human body, which opens up possibilities for 3D reconstruction of the interior of human GI tract.

Acknowledgements

In this dissertation I describe the research I conducted in pursuit of my Doctor of Philosophy Degree in Electrical and Computer Engineering in Worcester Polytechnic Institute.

Firstly, I would like to offer my sincerest gratitude to my research advisor, Professor Kaveh Pahlavan, for leading me into the world of research, for sharing his life experience, and for providing long term finacial support so that I could fully devote myself into the Ph.D. study. Professor Pahlavan is a kindly mentor and he has been so much more than that. In addition to the skills and knowledges I have learnt from him, his words of insight and sagacity encouraged me and held me in good stead. Throughout the past five years, when I feel anxious, worried, hesitated, or confused, professor Pahlavan told me that

Being a Ph.D. is like being in the Olympics. You have to fight for the gold medal! But at the end of the day, it is being at the Olympics that matters.

I could not understand the quote at the very beginning, but grinding this quote helps me calm down. Until very recently, looking at the 160 pages Ph.D. dissertation I have written, I feel confident and fulfilled, and I am happy with all the efforts I put on pursuing the doctorate degree.

An extra special thanks is due to professor Allen H. Levesque, professor Emmanuel Agu, Dr. Kamran Sayrafian, professor Lifeng Lai and professor Yehia Massoud for their thoughtful suggestions on my dissertation.

I have had the good fortune to work with a stella group of individuals at the CWINS lab. I would like to thank Dr. Jie He for guiding me for all my research work, I would like to thank Dr. Guanqun Bao for offering amazing job opportunity, I would like to thank Dr. Yunxing Ye, Dr. Dan Liu, Dr. ShiHong Duan, Dr. Yadong Wan, Dr. Yongtao Ma, Jin Chen, Ruijun Fu, Mingda Zhou, Guanxiong Liu, Bader

Alkandari, Zhouchi Li, Julang Ying for working together with me. I love the fimaly style environment you guys created.

Words can not express my gratefulness to my dear parents for their care and support and their important responsibility for enabling me in reaching this point of my life. Finally, I would like to dedicate this work to my wift Yifei for her love and support during this journey. Being with her, I get all the perseverance for facing challenges and overcoming obstacles.

Contents

List of Figures

List of Tables

Chapter 1

Introduction.

Precise and accurate localization and motion classification is an emerging fundamental areas for scientific research and engineering developments. With the thriving of pervasive computing related research fields, precise localization and motion classification received huge amount of attention from the community. Such science and technology began from the broad out door area applications, and gradually grew into smaller and more complicated in-door area and more recently it is proceeding into in-body area networking for medical applications.

Localization and motion classification technologies have their own specific challenges depending on the application and environment, which are left for scientists and engineers to overcome. One major challenge is that location estimation and motion classification often use hand-held devices or wearable sensors. Such devices and sensors usually work in indoor, near body environments and the human object has certain effects on the measurements. In that situation, existing mathematical models for general environments are no longer accurate and new models and analytical approaches are required to deal with the human body effects. This has opened opportunities for researchers to tackle a number of demanding problems.

This dissertation focuses on three novel problems in localization and motion classification using radio propagation (RF) modeling, in and around the human body. In this chapter, we discussed our novel contribution and the outline of the remainder of this dissertation.

1.1 Contribution

The dissertation consists of three major sections and the major contribution of this dissertation has been listed as follows:

- **Chapter 3**:
  - We analyzed the effect of human body on off-body radio propagation and proposed a novel TOA ranging error model that takes the effect of human body into consideration.
  - The proposed TOA ranging error model works for both wrist mounted sensors and chest mounted sensors, which are the most common situation for existing consumer electronic devices.
  - The proposed TOA ranging error model can be used for Cramer Rao Lower Bound calculation to help the evaluation of TOA based human localization systems.
  - The proposed TOA ranging error model is the first existing model in the literature that takes the human object into consideration.
- **Chapter 4**:
  - We analyzed the on-body radio propagation charactiristics between multiple body mounted sensors regarding various frequently seen human mo-

tions (standing, lyint, walking, running, climbing, crawling and running on the stairs).

  - We extract proper RF features that can represent different human motions and build a support vector machine to achieve more than 90% classification rate. The motion classification system is originally designed for first responders working in severe environment and it can be also used for patient monitoring and elderly daily monitoring.
  - The proposed motion classification application is the first existing system that uses RF chatacteristics as feature set, and the classification results can be fultered with existing techniques to further enhance the classification performance.

- **Chapter 5**:

  - We utilized the in-body radio propagation characteristics and image processing techniques to implement a hybrid localization system for Wireless Capsule Endoscopy. The hybrid localization can help improve clinical operations and has the potential to realize 3D reconstruction of small intestine.
  - We analyzed the possible source of uncertainty for Wireless Causpule Endoscopy hybrid localization and derived the formulation of Posterior Cramer Rao Lower Bound for the hybrid localization system. The Posterior Cramer Rao Lower Bound can be used as an evaluation metric for the system and facilitate its further development.
  - By using the Posterior Cramer Rao Lower Bound, we analyzed the effect of sensor number, sensor placement, system bandwidth and step estima-

tion accuracy. The analytical result can serve as a benchmark for such systems.

1.2 Dissertation Outline

The remainder of this dissertation is organized as follow: Chapter 2 introduced the research background of the entire dissertation. We start the discussion from general body area network, and then move to the radio propagation channel modeling for body area network, and finaly briefly introduced the existing applications for body area network.

Chapter 3 presented the precise indoor human tracking using TOA ranging technique based on off-body radio prapagation characteristics. We setup measurement systems to collect empirical data and perform curve fitting to obtain a universal TOA ranging error model for indoor human tracking. With the well-established model, the performance of existing indoor human tracking system can be improved.

Chapter 4 discussed the RF based human motion classification system using the support vector machine based on on-body radio propagation characteristics. We use the same system to perform measurement, extract proper feature from the collected data, and come up with a classification machenism to classify seven different frequently seen human motions. The proposed system can be used to monitor first responders and ensure their safety.

Chapter 5 proposed an evaluation metric to the wireless capsule endoscopy hybrid localization system based on in-body radio propagation characteristics. We derived the formulation of Posterior Cramer Rao Lower Bound and use the bound as an evaluation metric for the hybrid localization system to analyze the localization performance.

Finally, Chapter 6 presents the conclusion to this dissertation and discussion of the future works.

Chapter 2

Background.

2.1 Body Area Network in General

Recently, there has been increasing interest from researchers, system designers, and application developers on a new type of network architecture generally known as body sensor networks (BSNs) or body area networks (BANs), made feasible by novel advances on lightweight, small-size, ultra-low-power, and intelligent monitoring wearable sensors [Net]. In BANs, sensors continuously monitor humans physiological activities and actions, such as health status and motion pattern. Although many protocols and algorithms have been proposed for traditional wireless sensor networks (WSNs) [ASSC02], they are not well suited to the unique features and application requirements of BAN. There are several advantages introduced by using wireless BANs which include:

- **Flexibility**: Non-invasive sensors can be used to automatically monitor physiological readings, which can be forwarded to nearby devices, such as a cell phone, a wrist watch, a headset, a PDA, a laptop, or a robot, based on the application needs.

- **Effectiveness and Efficiency**: the signals that body sensors provide can be effectively processed to obtain reliable and accurate physiological estimations. In addition, their ultra-low power consumption makes their batteries long-lasting due to their ultralow power consumption.

- **Cost-effective**: With the increasing demand of body sensors in the consumer electronics market, more sensors will be mass-produced at a relatively low cost, especially in gaming and medical environments.

Compared with existing technologies such as WLANs, BANs enable wireless communications in or around a human body by means sophisticated pervasive wireless computing devices.

WBANs may interact with the Internet and other existing wireless technologies like ZigBee, WSNs, Bluetooth, Wireless Local Area Networks (WLAN), Wireless Personal Area Network (WPAN), video surveillance systems and cellular networks. Hence, marketing opportunities for services and advanced consumer electronics will thoroughly expand, allowing for a new generation of more intelligent and autonomous applications necessary for improving ones quality of life [CGV+11]. WBANs are expected to cause a dramatic shift in how people manage and think about their health, similar to the way the Internet has changed the way people look for information and communicate with each other [OMSJ05]. WBANs are capable of transforming how people interact with and benefit from information technology. WBAN sensors are capable of sampling, monitoring, processing and communicating various vital signs as well as providing real time feedback to the user and medical personnel without causing any discomfort [OMSJ05][CGV+11]. The use of a WBAN allows continuous monitoring of ones physiological parameters thereby providing greater mobility and flexibility to patients. Importantly, as WBANs provide

large time intervals of data from a patients natural environment, doctors will have a clearer view of the patients status [LBM+11]. However, formidable technical and social challenges must be dealt with to allow for their practical adoption. These challenges offer various system design and implementation opportunities with the major objectives of minimum delay, maximum throughput, maximum network lifetime and and reducing unnecessary communication related energy consumption (e.g. control frame overhead, idle listening and frame collisions). The user-oriented requirements of WBANs are equally challenging and have been defined as: ease of use, security, privacy, compatibility, value and safety [CGV+11][HPB+09].

2.2 Radio Propagation for Body Area Network

Early developments in Wireless Personal Area Networks (WPANs) were first made in the 90s by different groups working at MIT (Massachusetts Institute of Technology). Their initial aim was to interconnect information devices attached to the human body. They also intended to use electric field sensing to determine body positioning, through which the capability of modulating the electric field for data transmission throughout the body was realized.

Recent developments in wireless technologies has a major focus on increasing network throughput which shifts the focus of WPANs to short range, low power and low cost technologies [TFaNTM10]. Network lifetime has a greater importance in WBANs as devices are expected to perform over longer periods of time. Also, WPANs do not satisfy the medical communication requirements because of close proximity to the human body tissue. Thus, a standard model was required for the successful implementation of Body Area Networks addressing both its consumer electronics and medical applications.

Table 2.1: IEEE 802.15.6 radio propagation channel models.

	Description	Frequency Band	CM
S1	Implant to implant	402-405MHz	CM1
S2	Implant to body surface	402-405MHz	CM2
S3	Implant to external	402-405MHz	CM2
S4	Body surface to body surface (LOS)	13.5,50,400,600,900MHz, 2.4, 3.1-10.6GHz	CM3
S5	Body surface to body surface (NLOS)	13.5,50,400,600,900MHz, 2.4, 3.1-10.6GHz	CM3
S6	Body surface to external (LOS)	900MHz, 2.4, 3.1-10.6GHz	CM4
S7	Body surface to external (NLOS)	900MHz, 2.4, 3.1-10.6GHz	CM4

The IEEE 802 working group had a number of success stories in the realization of the international standardization for WBANs [KWM10]. A standing committee, Wireless Next Generation (WNG), was established in January 2006, within WG15 (Working Group) aiming for the examination of new topics and directions [ALK09]. In May 2006, an interest group of WBAN, namely, (IG-WBAN) was initially established. The executive committee of IEEE 802 WG15, formally approved IG-WBAN as a Study Group namely SG-WBAN [ALK09]. In January 2008, SG-WBAN was further certified as a Task Group (TG6) under 802.15 [Tg610]. The call for WBAN applications by TG6 was later closed in May 2008 and compiled all submitted application into a single document [Lew]. The IEEE 802.15.6 working group established the first draft of the communication standard of WBANs in April 2010, optimized for low-power on-body/in-body nodes for various medical and non-medical applications [KWM10]. The approved version of the IEEE 802.15.6 standard was ratified in February 2012 [ALK09] and describes its aim as follows: To develop a communication standard for low power devices and operation on, in or around the human body (but not limited to humans) to serve a variety of applications including medical, consumer electronics, personal entertainment and other.

The Channel Modeling Subgroup within TG15.6 identified seven different propagation scenarios (S1∼S7) in which IEEE 802.15.6 compliant devices may operate (Table 2.1). These scenarios are determined based on the locations of BAN nodes:

- **Implant**: Inside the human body.
- **Body Surface**: In direct contact with the skin or within 2cm distance.
- **External**: Beyond 2cm and up to 5m from the body surface

Scenarios S1, S2, and S3 correspond to implant nodes in a BAN. Two different channel models, CM1 and CM2, can be used to characterize the propagation scenarios for implant nodes. The frequency band 402∼405MHz has been allocated for medical implant communication services (MICS) by many international regulatory organizations including the Federal Communications Commission (FCC). A number of ultra-low-power medical implantable devices such as cardiac pacemakers and defibrillators already operate in this frequency band. The MICS band offers good propagation behavior through human tissues and enables the use of reasonable-sized antennas, but its limited bandwidth constrains the communication devices to low data transmission rates.

In the body area network communications, propagation paths can experience fading due to different reasons, such as energy absorption, reflection, diffraction, shadowing by body, and body posture. The other possible reason for fading is multipath due to the environment around the body. Fading can be categorized into two categories; small scale and large scale fading. Small scale fading refers to the rapid changes of the amplitude and phase of the received signal within a small local area due to small changes in location of the on-body device or body positions, in a given short period of time. The small scale fading can be further divided into flat fading and frequency selective fading. Large scale fading refers to the fading due to

motion over large areas; this is referring to the distance between antenna positions on the body and external node (home, office, or hospital).

Unlike traditional wireless communications, the path loss for body area network system (on body applications), is both distance and frequency dependent. The path loss model in dB between the transmitting and the receiving antennas as a function of the distance d based on the Friis formula in free space. The path loss near the antenna depends on the separation between the antenna and the body due to antenna mismatch. This mismatch indicates that a body-aware antenna design could improve system performance.

2.3 Applications for Body Area Network

Given the necessary background about BAN and BAN channel model, in the following chapters, we discuss three categories of applications that can be implemented on top of the BAN radio propagation characteristics. The three categories of applications works on different CMs. We start with the Indoor Human Tracking on CM4 (off-body channel), then we move on to Human Motion Detection on CM3 (on-body channel), and finaly we investigate the localization of micro-robot inside human body, which relies on CM2 (implant to body surface channel). In this section, we give a brief introduction of the existing literatures of the three categories of technology.

2.3.1 Indoor Human Tracking

Accurate, reliable and real-time indoor positioning and position-based protocols and services are required in the future generation of communications networks [VWG+03] [FFRV05]. A positioning system enables a mobile device to determine its position,

and makes the position of the device available for position-based services such as navigating, tracking or monitoring, etc. Location information of devices or users could significantly improve the performance of wireless network for network planning, network adaptation, load balancing, etc. Some position-based indoor tracking systems have been used in hospitals, where expensive equipment needs to be tracked to avoid being stolen, and the patients can get guidance to efficiently use the limited medical resources inside complex environments of the hospitals. Indoor navigation systems are also needed in a large public area to provide position indications for the users. For example, tourists need indoor navigation services in some large museums to see the artifacts in different places in sequence. In addition, position information brings benefits to self-organization and selfformation of ad hoc networks in the future communications systems.

The needs of users are highly addressed by the rapid development of integrated networks and services in personal networks (PNs) [GLN09]. Much more attention has been paid to context-aware intelligent services for personal use, which make the persons behaviors more convenient and simple. Position information in indoor environments is of course an essential part of the contexts. The uncertainty in dynamic and changing indoor environments is reduced by the availability of position information. And valuable position-based applications and services for users in PNs are enabled by location context offered by IPSs in various places such as homes, offices, sports centers, etc.

Global positioning system (GPS) is the most widely used satellite-based positioning system, which offers maximum coverage. GPS capability can be added to various devices by adding GPS cards and accessories in these devices, which enable location-based services, such as navigation, tourism, etc. However, GPS can not be deployed for indoor use, because line-of-sight transmission between receivers and

satellites is not possible in an indoor environment. Comparing with outdoor, indoor environments are more complex. There are various obstacles, for example, walls, equipment, human beings, influencing the propagation of electromagnetic waves, which lead to multi-path effects. Some interference and noise sources from other wired and wireless networks degrade the accuracy of positioning. The building geometry, the mobility of people and the atmospheric conditions result in multi-path and environmental effects. Considering these issues, IPSs for indoor applications raise new challenges for the future communications systems.

Some articles [HB01][BKKS09] have given an overview of various available technology options for the design of an IPS such as infrared (IR), ultrasound, radio-frequency identification (RFID), wireless local area network (WLAN), Bluetooth, sensor networks, ultra-wideband (UWB), magnetic signals, vision analysis and audible sound. Based on these fundamental technologies, numerous IPSs have been developed by different companies, research centers and universities. Each system takes advantage of a particular positioning technology or combining some of these technologies, which also inherits the limitations of these technologies. The designers make tradeoff between the overall performance and the complexity of the IPSs.

2.3.2 Human Motion Detection

Automatic capture and analysis of human motion is a highly active research area due both to the number of potential applications and its inherent complexity. The research area contains a number of hard and often ill-posed problems such as inferring the pose and motion of a highly articulated and self-occluding non-rigid 3D object from images. This complexity makes the research area challenging from a purely academic point of view. From an application perspective computer vision-based methods often provide the only non-invasive solution making it very attractive.

Applications can roughly be grouped under three titles: surveillance, control, and analysis. Surveillance applications cover some of the more classical types of problems related to automatically monitoring and understanding locations where a large number of people pass through such as airports and subways. Applications could for example be: people counting or crowd flux, flow, and congestion analysis. Newer types of surveillance applicationsperhaps inspired by the increased awareness of security issues are analysis of actions, activities, and behaviors both for crowds and individuals. For example for queue and shopping behavior analysis, detection of abnormal activities, and person identification.

Control applications where the estimated motion or pose parameters are used to control something. This could be interfaces to games, e.g., as seen in Eye-Toy [MHK06a], Virtual Reality or more generally: HumanComputer Interfaces. However, it could also be for the entertainment industry where the generation and control of personalized computer graphic models based on the captured appearance, shape, and motion are making the productions/products more believable.

Analysis applications such as automatic diagnostics of orthopedic patients or analysis and optimization of an athletes performances. Newer applications are annotation of video as well as content-based retrieval and compression of video for compact data storage or efficient data transmission, e.g., for video conferences and indexing. Another branch of applications is within the car industry where much vision research is currently going on in applications such as automatic control of airbags, sleeping detection, pedestrian detection, lane following, etc.

2.3.3 Inbody Micro-Robot Localization

Wireless video capsule endoscope (VCE) has been in the clinical arena for 12 years. The latest VCE devices appearing in the market are evolving into micro-robots with

mechanical legs that can stick to specific location for closer observations, precision medical delivery or other missions [PBY+12]. An endoscopy capsule provides a non-invasive wireless imaging technology for the entire gastrointestinal (GI) tract with the unique feature for medical applications in terms of observing abnormalities in the small intestine. The small intestine is a "long" curled tube with an average length of six meters. While physicians can receive clear pictures of abnormalities in the GI tract with capsule endoscopy, they have little idea of their exact location inside the GI tract [KK15]. As a result, when surgical intervention to excise a lesion is indicated, localization of the lesion can be very challenging. Exploratory clinical procedures include computed tomography (CT), planar X-ray imaging, magnetic resonance imaging (MRI). Ultrasound, laparoscopy or surgery. Radiological imaging procedures such as CT and MRI are not easily combined with capsule endoscopy because of the requirement for continuous imaging over several hours. Therefore, if we could use the RF signal radiated from the capsule to also locate these devices, not only can physicians detect lesions, but they can also locate them efficiently.

RF localization science and technology started with the global positioning systems (GPS) for outdoor areas, then it transformed into wireless indoor geolocation [PBY+12]. The next step in the evolution of this science is the transformation into RF localization inside the human body [PBM13]. However, RF localization of micro-robots inside humans is not trivial. Compared to outdoor and indoor environments, the inside of the human body is a complex environment making engineering design and visualization a formidable task. The inside of the human body is an extremely complex medium for RF propagation because it is a nonhomogeneous liquid-like environment with irregularly shaped boundaries and severe path-loss. When the signals are used for RF localization of micro-robots, things become more complex since the road map for the movements of the micro-robot is blurry and the

body mounted sensors used as references for localization are also in motion. More importantly, reliable designs need testing the hardware implementation, but we cannot easily test devices inside the human bodies. Like maps for outdoor and indoor navigation, we need a "3D map" of the human body for virtual visualization of the location of the micro-robots to observe the uncertainty in location for a medical application. To overcome these difficulties, we need to design a cyber physical system (CPS) as a testbed for performance evaluation and virtual visualization of the interior of the human body to be used for advancements in in-body RF localization science and technology.

The existing principles of science and technology for engineering design of RF localization systems for microrobots traveling inside the human body are in their infancy and there is a need for multi-disciplinary research in this area. As far as we know attempts to deploy such systems have not been successful and to date there are no clinically available systems for this purpose.

The RF localization inside the human body is a fertile area for seminal scientific research with a broad impact on a number of engineering designs for the future of the wireless health industry. From a scientific point of view, by solving the localization problem for micro-robots, we will shed light on 3D RF localization of devices with irregular patterns of motion in a non-homogeneous and non-stationary medium such as the human body. The results of this research may have a considerable impact on the evolution of navigation technology and understanding of fundamentals of localization science. From an engineering design point of view, solving the RF localization problem inside the human body will enable a number of applications ranging from localization of the endoscopy capsule, precision drug delivery, localization of the intrusive devices during surgery and localization of micro-devices to open blood clots, which are emerging in practice. One can also envision that many more

will appear as the enabling navigation and visualization technologies open the path for micro-robotic surgery inside the human body. Further advancement in research in this area requires a CPS for performance evaluation and visualization to allow design of realistic algorithms and analysis of the effects of RF radiations.

Chapter 3

Off-Body Radio Propagation and Precise Indoor Human Tracking Using TOA Ranging Technique.

Recent advancements in electronics and wireless communication have enabled the development of small and intelligent wireless wearable sensors, which can be widely used in medical and non-medical applications. For many users of wearable medical sensor, such as firefighters in burning house, soldiers in battlefield, miners in the underground environment and patients in the hospital, the real-time positions are critical information to their safety in emergency situations [MMTP11][PXM02]. For these applications, the wearable sensors should not only detect the health information, but also provide the location of the sensors in order to track the sensor holder. In outdoor area, global positioning system (GPS) is usually employed to provide the positioning service. However, the GPS is unable to work in indoor area as the signal of satellite is cut off by the wall and roof of buildings. Radio frequency (RF) measurement technologies, such as received signal strength (RSS), time of ar-

rival (TOA), angle of arrival (AOA), time difference of arrival (TDOA), provides candidate solutions to construct indoor positioning system. Superior to the other solutions, TOA-based indoor localization is famous for its extraordinary accuracy and practical features [PXM02][HGW+13][ZB12].

Ultra-wide band (UWB) and Chirp spread spectrum (CSS) technologies have been developed to implement the physical layer for centimeter-level and 1-meter-level TOA ranging respectively. However, the claimed ranging accuracy can only be achieved in line of sight (LOS) scenario in free space or outdoor area. For TOA-based distance measurement, only the propagation time of direct path (DP) pulse between transmitter (TX) and receiver (RX) represents the true distance. Therefore, the performance of TOA ranging depends on the availability of direct path signal. In multipath rich environment, such as indoor area or under ground mine, severe multipath would combine with DP pulse and shift its arrival time. Also, the non-line of sight (NLOS) type of blockage between TX and RX would significantly attenuate the signal strength and delay the propagation time. Both multipath and NLOS could leads to significant distance measurement error, which is the greatest challenge to the algorithm design and performance evaluation of TOA-based indoor geolocation system.

For the localization of wearable sensors, the target node is mounted on the surface of human skin or at most centimeters away from body surface [PYFK12]. TOA ranging performs in the wireless channel between the surface of human body and the external reference node. Such channel is defined as CM4 in IEEE 802.15.6 standard, which is designed for the communication between body area network (BAN) and local area networks (LAN)/wide area networks (WAN), thus making the remote services come true [PBY+12][Tg610][LGP12][GCP13][RXN+11]. In that situation, human body can be regarded as a smooth and bended surface on which the wire-

less signal can be diffracted and travels in the pattern of creeping wave [PPK12]. Consequently, apart from the non-line of sight (NLOS) error cause by the penetration loss of human body, the creeping wave around the surface of human body also contribute to the inaccuracy of TOA-based indoor localization. Due to the complexity of penetration and creeping process of wireless signal, it is very difficult to solely identify the NLOS error and ranging error caused by creeping wave. However, knowing the joint effect of the involvement of human body is significantly helpful in evaluating the human tracking systems performance as well as designing localization algorithms.

With the development of body area network, the effect of human body on wireless channel has been considered. However, most studies pay attentions on the effect of human body on data communication. Characterization of the channels for TOA ranging applications is different from data transmission oriented applications. For the latter, the focus is on data rate and communication coverage through the characterization of the delay spread and the path loss of the total signal energy. The former, however, requires special attention on the ranging accuracy, i.e., the statistics of the ranging error.

The behavior of TOA ranging error has been reported in [AAP09][HWZe11][AP06], which are limited to studies on the effect of multipath and NLOS scenario caused by the environment. Empirical measurements are often performed in typical indoor area without the involvement of human body. Though Ref. [GP08][TDM11] studies the localization algorithm for TOA-based human tracking, these researches are still based on traditional ranging error model, suffering from the inaccuracy caused by the human body. As a result, a comprehensive measurement and modeling work on the effect of human body regarding TOA-based ranging for wireless wearable sensor is still not available in the literature. These models are needed as the theoretical

basis for developing algorithms to reduce the effect of human body caused ranging error. Also, they are necessary for determining localization performance bounds, which can provide insights into the fundamental limitations for TOA-based human tracking application.

In this chapter, measurements have been conducted inside typical office environment with the target sensor mounted to the chest and wrist of human body, which is the common positions for smart watch or health monitor. The TOA ranging error is observed to form a Gaussian distribution and the empirical measurement results have been analyzed from the perspective of system bandwidth, signal to noise ratio (SNR) and geometrical relationship of human body, target node and reference nodes. Statistical model for the specific scenario has been built using bandwidth, SNR and geometrical information as parameters and the model coefficients have been properly calculated by curve fitting. The ranging error model is separated into LOS scenario and NLOS scenario and it also shows the minimum SNR required for successful localization. At the end of this chapter, the ranging error model has been validated.

The remainder of this section is organized as follows: Section 3.2 describes the environment, system setup and scenarios of the measurement; Section 3.3 provides the empirical measurement results and analysis; Section 3.4 present the derivation of the detailed TOA ranging error model considering the effect of human body for chest mounted sensor and wrist mounted sensor respectively. Section 3.5 presents our conclusions and comments on the future work.

3.1 Background.

For a TOA-based geolocation system, the time of flight of the direct path between a transmitter and a receiver is used to determine the intervening distance. A pulse is transmitted and the difference between the time of occurrence of the transmitted pulse and the first received pulse is used to measure the TOA [WTK+09][HAP08]. Reflections and blockage in indoor environment caused by walls, furniture and people moving inside the building cause severe multipath condition, which result in rapid fluctuations of the power of the direct path. In a multipath environment, the received waveform is combination of the pulse arriving on the direct path and pulses arriving on other paths between the transmitter and receiver. As a result, the shape of the transmitted waveform and the expected time of occurrence of the first received pulse are not preserved at the receiver. Consequently, the measured TOA of the direct path suffers from inaccuracy [ZB12]. The direct path can be blocked by large metallic objects [LGP12] and large concrete walls or its first peak used for time of flight measurements may shift due to multipath components arriving close to the direct path [PXM02]. These errors in the TOA estimation cause ranging errors that are a function of the environment and bandwidth of the measurement system [GCP13].

3.1.1 Multipath Conditions for General TOA Based Indoor Localization.

To qualitatively represent the TOA ranging error caused by the above mentioned reasons, a classification of multipath condition has been proposed in Ref. [AP06], in which the multipath environment has been partitioned into three categories including LOS-DDP, NLOS-DDP and NLOS-UDP:

- **LOS-DDP**: The direct path can be clearly detected at the receiver side. Inaccuracy comes from either the system level uncertainty, or the combination of direct path and other reflected paths, which are close to direct path.
- **NLOS-DDP**: The direct path has been blocked and attenuated by the objects such as wood or glass. In that case, the direct path can be still detected at the receiver side. It suffers similar inaccuracy as the LOS-DDP situation, plus the inaccuracy caused by the attenuated or shifted direct path.
- **NLOS-UDP**: The direct path has been completely blocked by objects such as huge metal and concrete wall. In this condition, the direct path can be no longer detected at the receiver side. Inaccuracy comes from mistakenly taking other reflected path as the direct path, which results in huge TOA ranging error.

3.1.2 Multipath Conditions for TOA Based Indoor Human Tracking.

In human localization systems, sensors are often attached to the surface of human body, leading to the different propagation characteristics of localization signal. Existing literature [CSSK+13] shows that wideband RF signal penetrating human body suffers from 6dB/cm to 8dB/cm attenuation, indicating that penetration signal hardly ever survive from the NLOS condition caused by human body. Without the penetration signal, NLOS-DDP condition no longer exists in the NLOS condition caused by human body. Instead, the transmitted localization signal travels as free space propagation from the Tx antenna and then get diffracted at the surface of human body. After that, the signal propagates along the body surface in the pattern of creeping wave until it reaches the Rx antenna. Fig 3.1 illustrates the

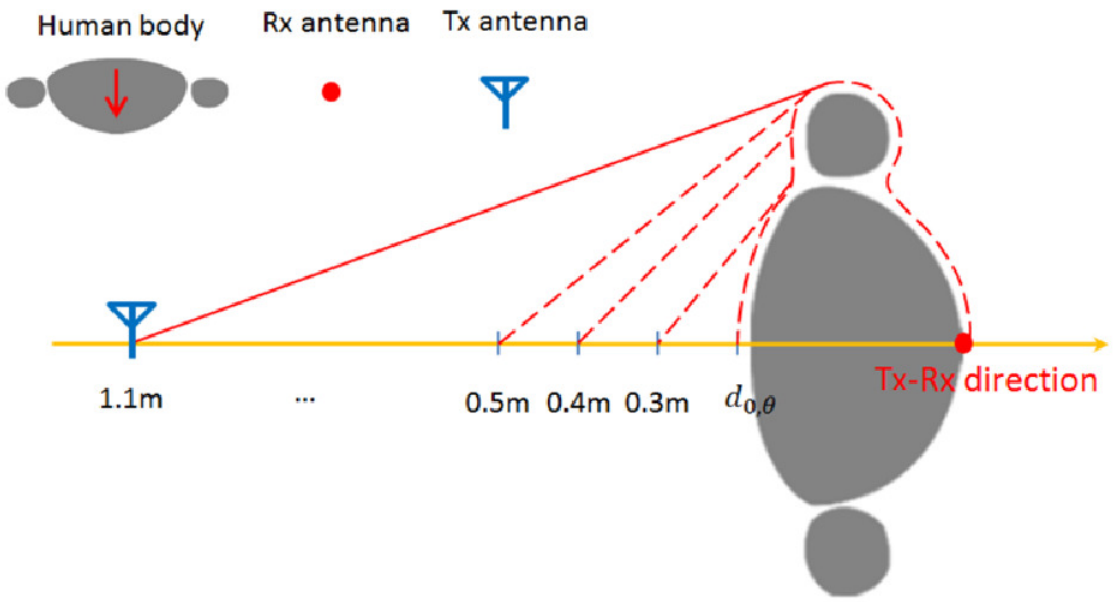

Figure 3.1: Sketch of propagation route of localization signal in the creeping wave pattern. The RX antenna is attached to the middle of human chest, at the same height of TX antenna.

creeping wave phenomenon when Tx antenna is located at different locations. There can be multiple creeping wave in the NLOS condition and the first detectable path at the receiver side will be regarded as the first path. The complex propagation characteristics becomes the source of TOA ranging error for body mounted sensors and such mechanism is thoroughly different from the undetected direct path (UDP) error introduced in Ref. [AP06]. Therefore, considering the effect of human body, the multipath condition for TOA-based indoor human localization can be again partitioned into two categories as: **LOS-DDP** and **NLOS-UDP**.

3.2 Measurement Scenario.

In order to understand the radio propagation characterristic of the previously mentioned off-body channel, it is necessary to build a measurement system, collect em-

pirical channel profile and come up with a relatively accurate TOA ranging model. In this section, we start our discussion from the measurement system and measurement scenario.

The TOA-based positioning system composes of Target Sensor (TS) mounted on the tracking target and Reference Node deployed in the known positions. Waveform propagation times among TS and RNs are measured to calculate the corresponding distances. Frequency-domain measurement techniques based on vector network analyzer (VNA) have previously been employed to characterize the channel impulse response, we select the same method to measure the channel profile in this dissertation. With the profile of the channel impulse response, the propagation time of the first detectable path in the received signal can be measured to calculate the distance between TX and RX. In this section, we use the above mentioned process to measure the effect of human body on TOA-based distance estimation in a typical office environment.

3.2.1 Measurement System.

As shown in Fig 3.2, the measurement system employs a vector network analyzer (Agilent E8363), a pair of UWB antenna (Skycross SMT-3TO10M), low loss cables and a power amplifier (3-8GHz, 30db). The receiver (RX) antenna is used as target sensor, which is mounted to the human body. The involved human objective remains standing posture during the measurement. The transmitter (TX) antenna is used as reference node and it is attached to a tripod with the same height of RX antenna.

During the measurement, S-parameter S_{21}, the transfer function of the channel, is measured by VNA in frequency domain with 1601 sample points. The received signal is transferred to time domain by inverse fast Fourier transform (IFFT) with a Hanning window applied to the time domain received channel profile to limit

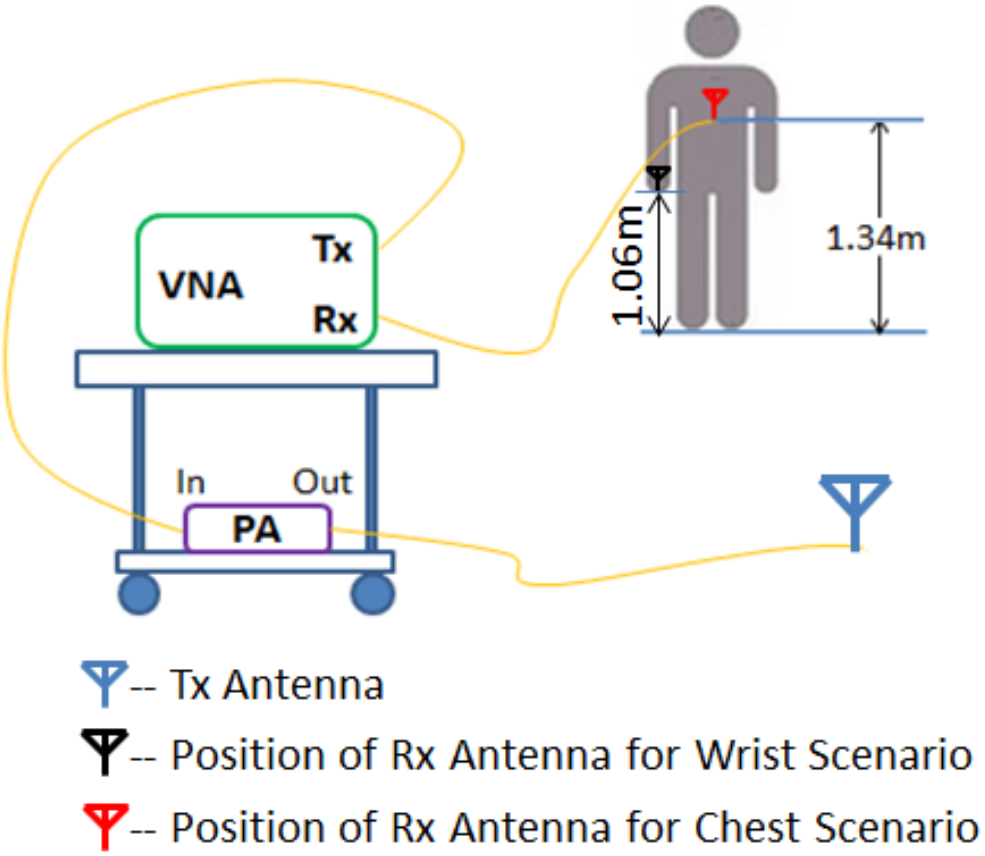

Figure 3.2: Measurement system including network analyzer, power amplifier, human body and antennas. (The components and inter-connection)

the sidelobe. The first peak can be detected by setting up proper threshold of the time domain signal strength and the propagation time of the first peak can be easily estimated. To guarantee the accuracy of the first path TOA, undesirable effects of the cables, the power amplifier, antennas and other system components are removed through system calibration. Typical recorded channel profile has been shown in Fig 3.3 in which the first detected path above the threshold arrived at time τ. Therefore, the estimated distance between target sensor and reference node can be defined as $\hat{d} = \tau \times c$ where c is the speed of radio wave propagation in the free space.

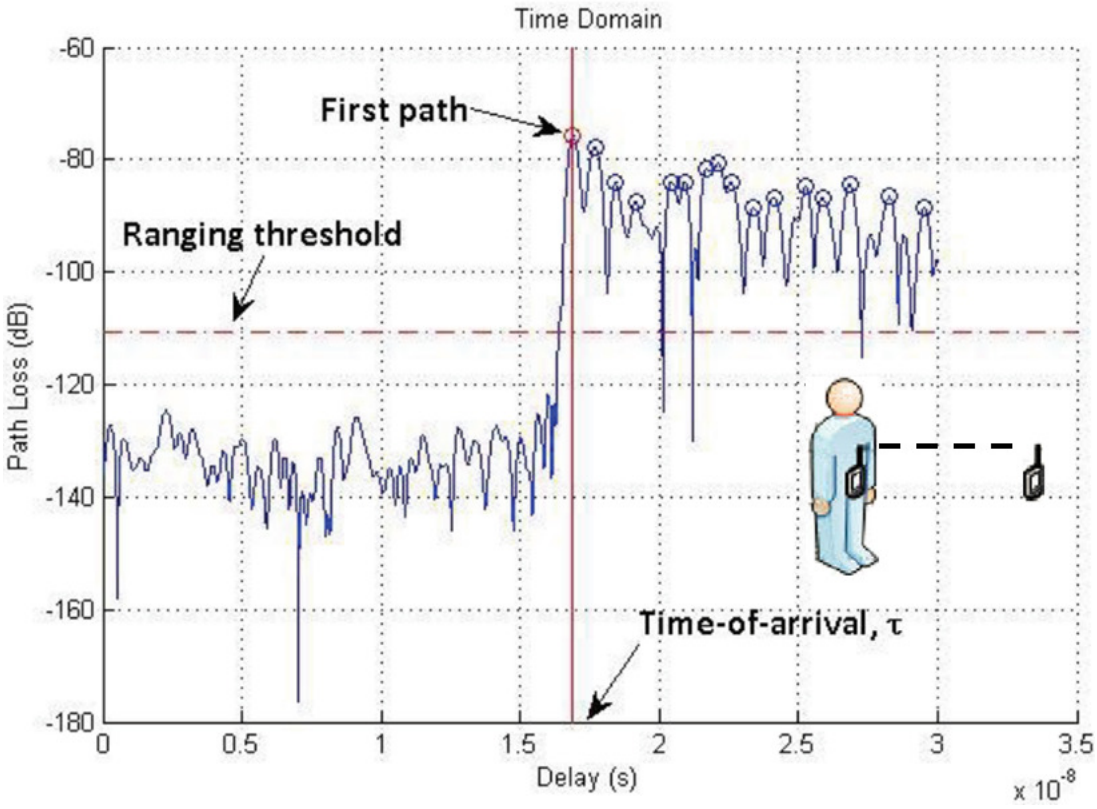

Figure 3.3: Measurement system including network analyzer, power amplifier, human body and antennas. (A sample of recorded channel profile)

3.2.2 Settings.

The measurement was performed in Room 233 of Atwater Kent Laboratory, an office building located in Worcester Polytechnic Institute, Worcester, MA, US. As shown in Fig 3.4 and Fig 3.5, this room is medium size with dimensions of approximately 18×12 meters and filled with desks, chairs, large windows and blackboards. The TX antenna is located near the wall and the distance between TX and RX antenna is fixed to 5m. TOA ranging error e can be then defined as:

$$e = \hat{d} - d \tag{3.1}$$

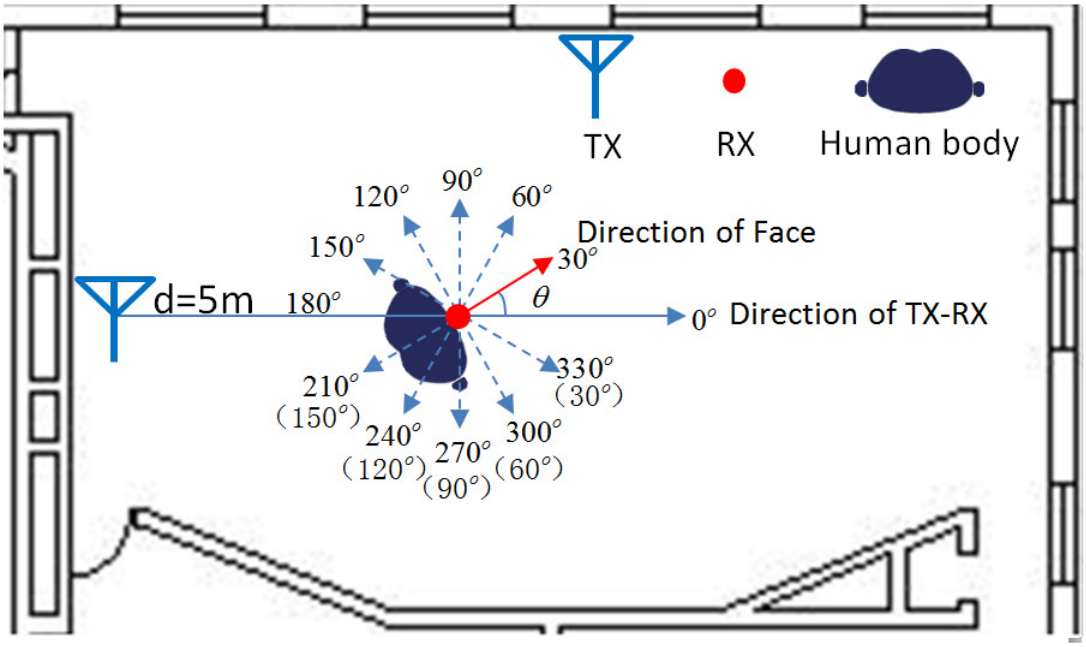

Figure 3.4: Measurement scenario with the angle θ defined as the horizontal angle between human facing direction and the TX-RX direction.(a):Chest Mounted Sensor.

where $\hat{d}$ is the distance estimation in our measurement and d is the actual distance, 5m.

Considering the effect of the position of target sensor, TOA ranging for chest mounted sensor and wrist mounted sensor are performed and analyzed separately, as shown in Fig 3.4 and Fig 3.5. These two figures illustrate the measurement scenarios of chest mounted sensor and wrist mounted sensor respectively. The measurement cases can be described using a scenario-based approach. A measurement case set, denoted by:

$$Case = \{\mathrm{P}, \theta, \mathrm{SNR}_{\mathrm{LOS}}, W\} \tag{3.2}$$

It consists a subset P which is the position of the target sensor, a subset W which is the indoor human tracking system bandwidth, a SNR subset $\mathrm{SNR}_{\mathrm{LOS}}$ which is the SNR before taking into account the effects of human body and an angle subset θ

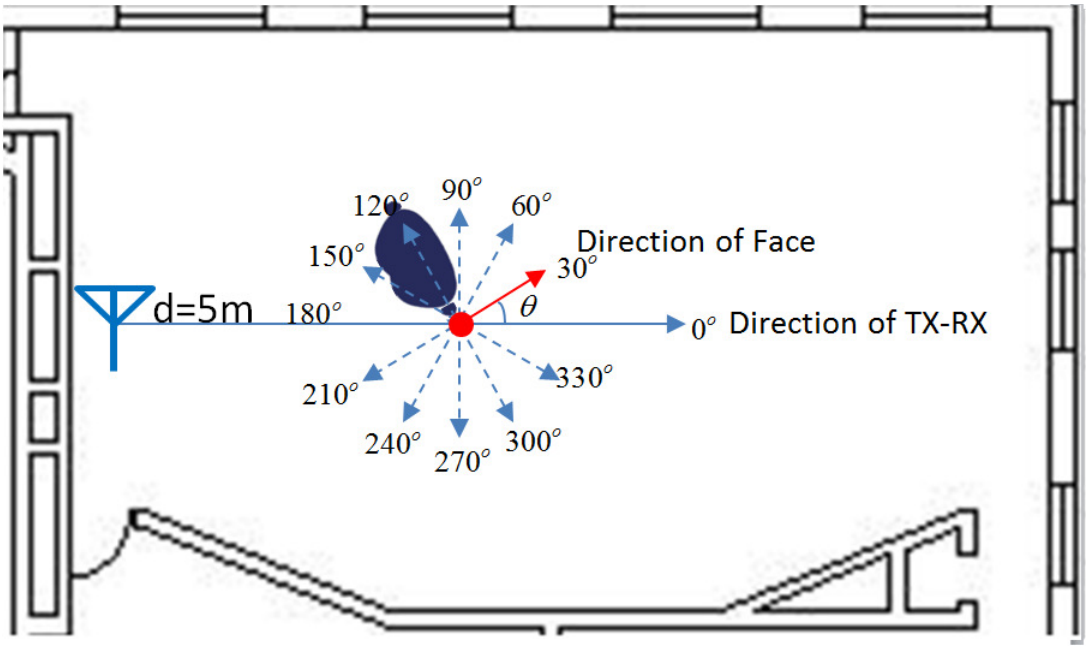

Figure 3.5: Measurement scenario with the angle θ defined as the horizontal angle between human facing direction and the TX-RX direction.(b):Wrist Mounted Sensor.

which represents the geometrical relationship of human body and TOA-based localization sensors. A specific case of our measurement can be $\{Chest, 30^o, 62.0dB, 1GHz\}$. For each measurement case, over 600 samples of TOA ranging errors are obtained to guarantee the validity of the measurement result and definition and settings of three subsets are introduced as follow:

Sensor Positions P.

The positions of sensor include chest and wrist. In chest-mounted scenario, the RX antenna is amounted in the middle of chest of human body with the height of 1.34 meters; in wrist-mounted scenario, the RX antenna is attached to the left wrist of

human body at the height of 1.06m. The subset P is given by:

$$P = \{Chest, Wrist\} \tag{3.3}$$

Geometric Relationship θ.

As shown in Fig 3.4 and Fig 3.5, the geometric relationship among human body, TX and RX is defined as the horizontal angle between the facing direction of the human body and the direction of TX-RX. Measurements are performed in every 30^o as shown in Fig 3.4 and Fig 3.5 and the subset θ is given by:

$$\theta = \{0^o, 30^o, 60^o, 90^o, ..., 300^o, 330^o\} \tag{3.4}$$

Measurement scenarios can be partitioned into LOS-DDP or NLOS-UDP condition by whether the human body is blocking the direct line between TX and RX or not. The relationship between θ and the channel condition is as follow:

- **Chest mounted scenario**: while $\theta \in [0^o, 90^o)$ or $\theta \in (270^o, 360^o]$, the channel condition is NLOS-UDP; while $\theta \in [90^o, 270^o]$, human body does not block the direct line of site, the multipath condition is LOS-DDP.
- **Wrist mounted scenario**: while $\theta \in [0^o, 180^o)$, the channel condition is NLOS-UDP; while $\theta \in [180^o, 360^o)$, human body does not block the direct line of site, the multipath condition is LOS-DDP.

Signal to Noise Ratio $\mathbf{SNR_{LOS}}$.

In the measurements, the transmit power P_{TX} of VNA has been set from 0 to -40 dBm by 10dBm per step to model the effect of human body on TOA ranging error in different SNR condition. In order to obtain $\mathrm{SNR_{LOS}}$, RX antenna is attached

to a tripod with the same height of TX antenna in the same position as depicted in Fig 3.2 and the pure background noise in the typical indoor environment of our measurement has been measured. $\mathrm{SNR_{LOS}}$ is then calculated by using P_{TX} and the background noise. The SNR subset $\mathrm{SNR_{LOS}}$ is defined as follows:

$$\mathrm{SNR_{LOS}} = \{71.5dB, 62.0dB, 52.4dB, 42.3dB, 32.4dB\} \tag{3.5}$$

System Bandwidth W.

Four popular UWB bandwidths ranging from 500MHz up to 5GHz are used in our measurements to analysis the effect of bandwidth on TOA ranging error for indoor human tracking. The system bandwidth subset W can be given by:

$$W = \{5GHz, 3GHz, 1GHz, 500MHz\} \tag{3.6}$$

3.3 Result Analysis.

In order to accurately model the measured TOA ranging errors, it is necessary to understand the pattern of these ranging errors from the statistical point of view. We randomly select multiple measurement cases and try to fit the ranging error samples into the probability distribution function (PDF) of existing random distributions. The general observation for our measurement is that the TOA ranging for every measurement case forms Gaussian distribution no matter in LOS-DDP or NLOS-UDP condition. The curve fitting result for sample result has been shown in Fig 3.6 in which the Gaussian PDF has been proved to be the best fit line. With this general observation, we started to analyze the impact of each different aspects among P, θ, $\mathrm{SNR_{LOS}}$, W.

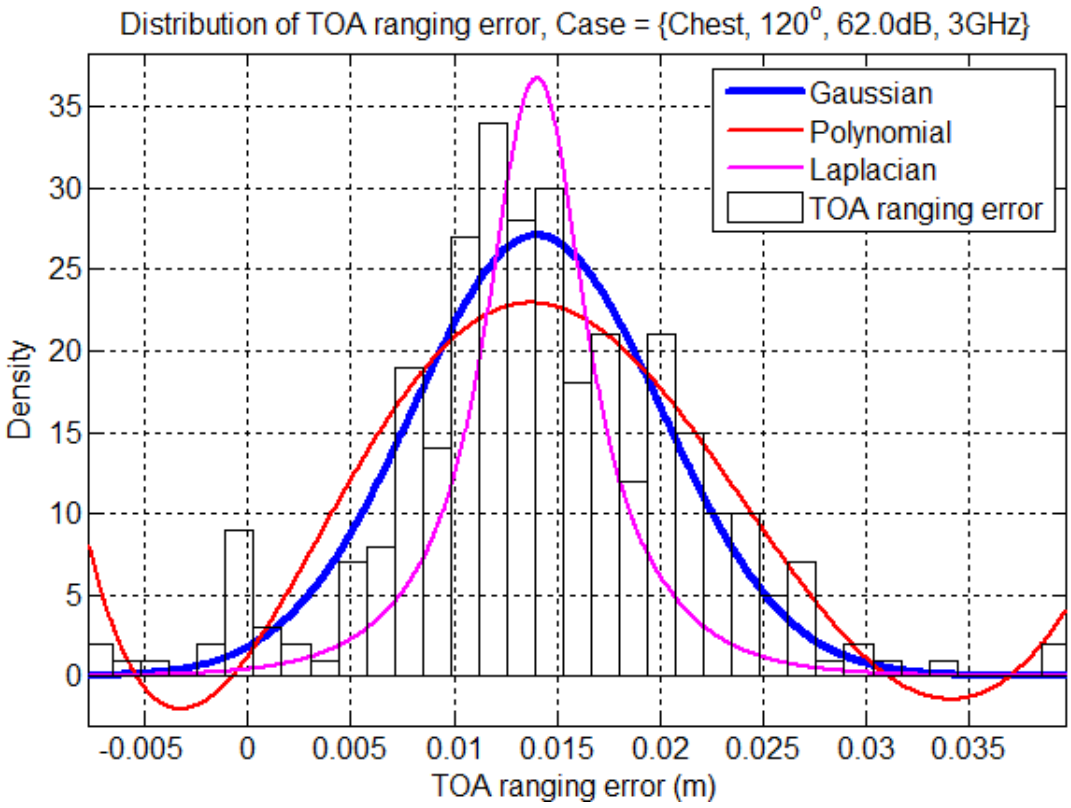

Figure 3.6: Sample distribution of TOA ranging error with PDF curve fitting, $Case = \{Chest, 120^o, 62.0dB, 3GHz\}$.

3.3.1 Effect of Geometrical Relationship θ.

To better understand the effect of geometrical relationship (θ) on TOA ranging error, the mean and variance of the Gaussian distribution have been further investigated.

Fig 3.7 and Fig 3.8 shows the relationship between the mean and variance of TOA ranging error and the horizontal angle θ in chest-mounted scenario. Because the RX antenna is mounted in the middle of the chest, as shown in Fig 3.4, the effect of human body on TOA ranging of target sensor while

$$\theta = \{180^o, 210^o, 240^o, 270^o, 300^o, 330^o, 360^o\}$$

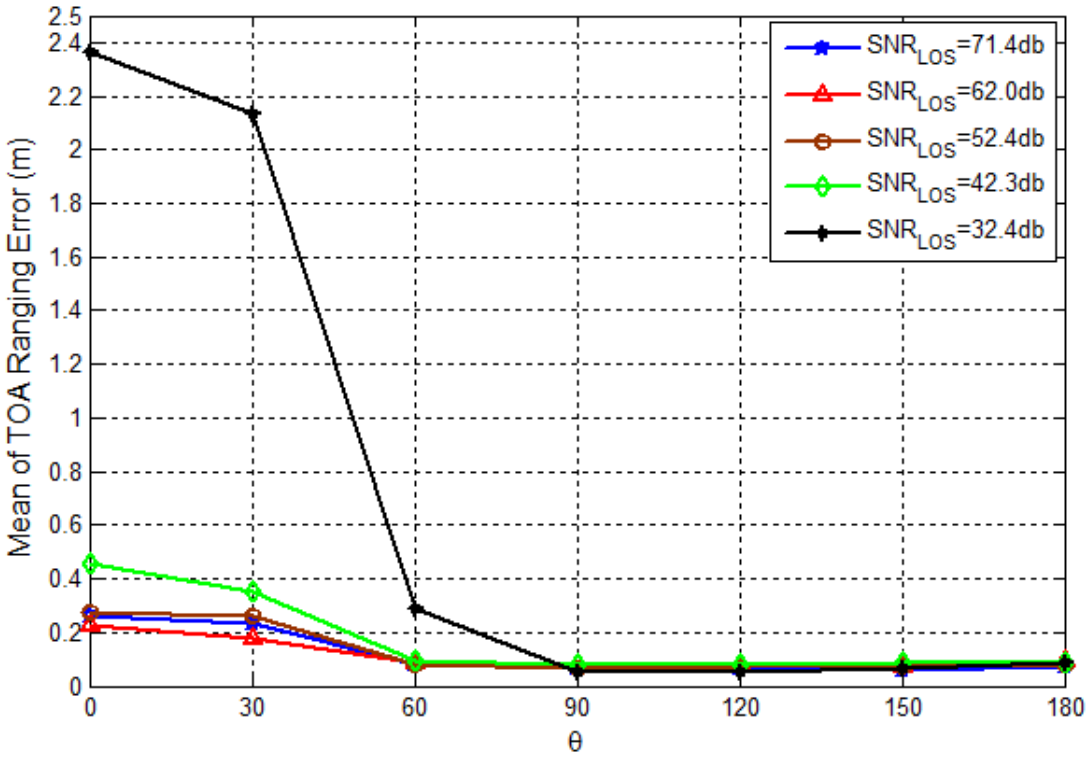

Figure 3.7: Effect of θ on TOA ranging in chest-mounted scenario. (a):Mean of the mean of TOA ranging error.

is equal to the effect while

$$\theta = \{180^o, 150^o, 120^o, 90^o, 60^o, 30^o, 0^o\}$$

To make the result more clearly, only the result of $\{0^o, 30^o, 60^o, 90^o, 120^o, 150^o, 180^o\}$ is shown in Fig 3.7. As is mentioned in the previous sections, when $\theta \in [90^o, 180^o]$, we define it as the LOS-DDP condition, which means the human body is not blocking the direct line between TX and RX. In that condition, both mean and variance of the TOA ranging error are relatively stable, indicating that the horizontal angle θ has little effect on the TOA ranging error distribution because the direct path always exists and the first path we observed in the time domain channel profile can

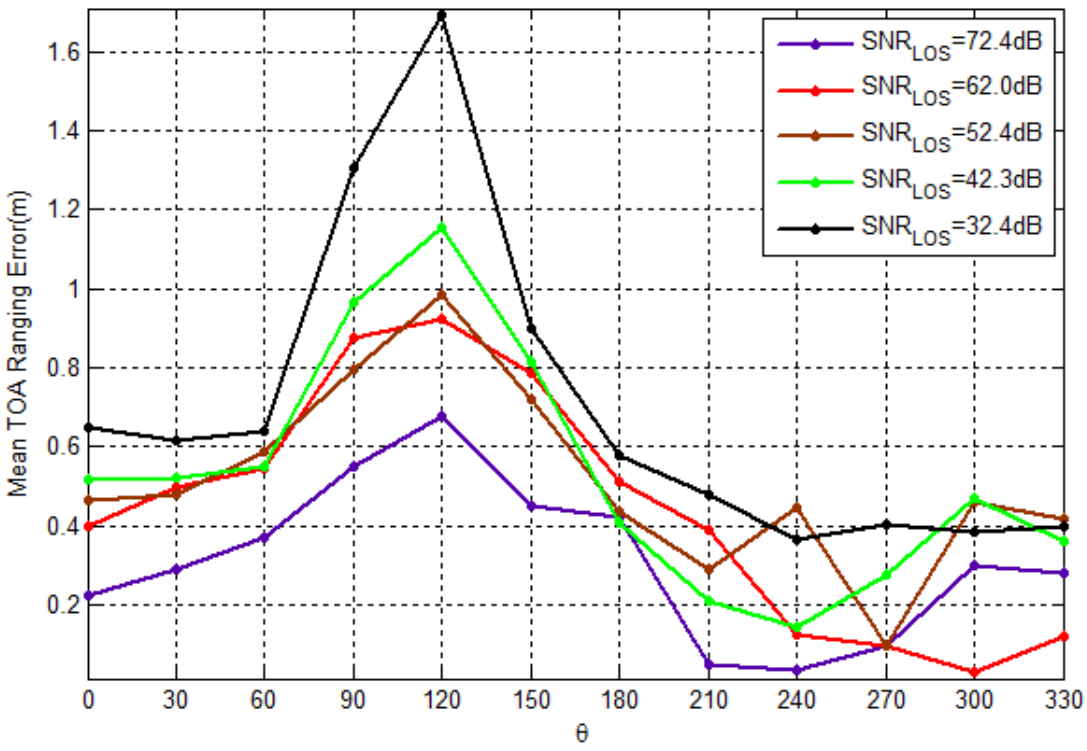

Figure 3.8: Effect of θ on TOA ranging in chest-mounted scenario. (b):Variation of the variance of TOA ranging error.

be regarded as the direct path itself. In NLOS-UDP condition, where $\theta \in [0^o, 90^o)$, dramatic change of both the mean and variance can be found. The distance measurement error increases significantly while θ varies from 90^o to 0^o, which indicates that the effect of human body becomes increasingly severe in the process.

Fig 3.9 and Fig 3.10 shows the relationship between the mean and variance of TOA ranging error and the horizontal angle θ in wrist-mounted scenario. Similar to chest-mounted scenario, the mean and variance of TOA ranging error are relatively small and stable in LOS-DDP condition, while $\theta \in [180^o, 360^o)$. The mean and variance also change dramatically in NLOS-UDP condition, while $\theta \in [0^o, 180^o)$. Since the asymmetric between chest and back of human body, the most seriously effect of human body on TOA ranging in wrist-mounted scenario occurs while $\theta \approx$

120^o, which is different from the $\theta = 90^o$ result in the case of chest-mounted sensor.

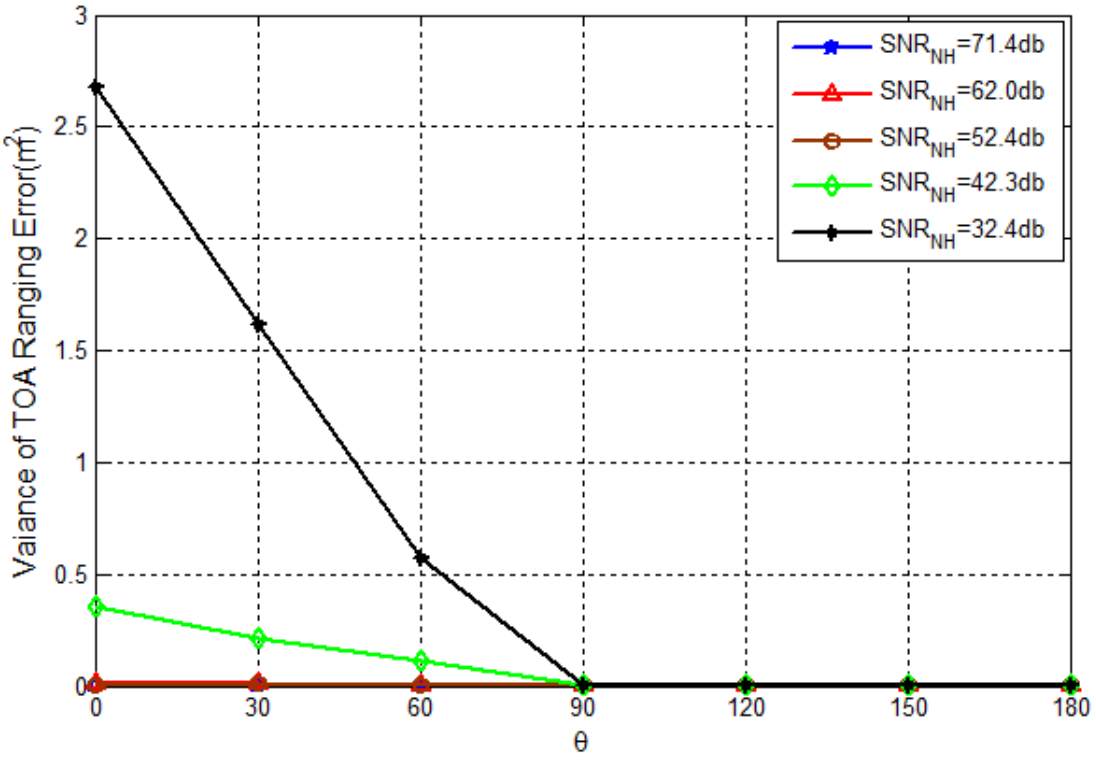

Figure 3.9: Effect of θ on TOA ranging in wrist-mounted scenario. (a):Variation of the mean of TOA ranging error.

3.3.2 System Bandwidth.

Bandwidth is a critical feature to the precision of TOA based localization system. Lager bandwidth leads to narrower pulse and enhances the capability of reducing the effect of multipath. When the time-domain pulse width is narrow enough, it is very difficult for the adjacent path to combine with each other, thus the direct path can be easily isolated. Given 5GHz System bandwidth, the pulse width can be limited within 2ns, making the peak detection process much easier. To further analyze the effect of bandwidth on TOA ranging error, additional measurement has

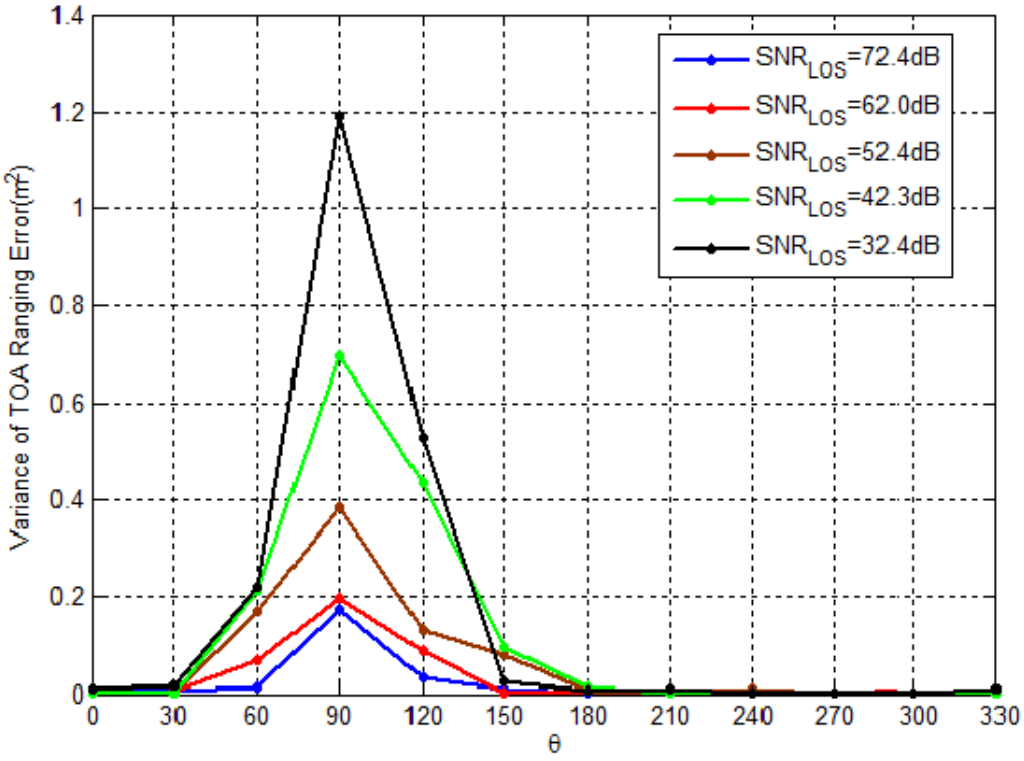

Figure 3.10: Effect of θ on TOA ranging in wrist-mounted scenario. (b):Variation of the variance of TOA ranging error.

been conducted at different system bandwidth, including:

$$\{50MHz, 100MHz, 200MHz, 300MHz, 500MHz, 1GHz,$$

$$1.2GHz, 1.5GHz, 2GHz, 2.5GHz, 3GHz, 3.5GHz, 4GHz,$$

$$4.5GHz, 5GHz\}.$$

Fig 3.11 and Fig 3.12 show the variation of mean and variance of TOA ranging error in LOS condition while the bandwidth changes from $50MHz$ to $5GHz$. As we expected, when the bandwidth drops, both mean and variance of TOA ranging error increase. As shown in Fig 3.11, given 5GHz system bandwidth, the mean of ranging

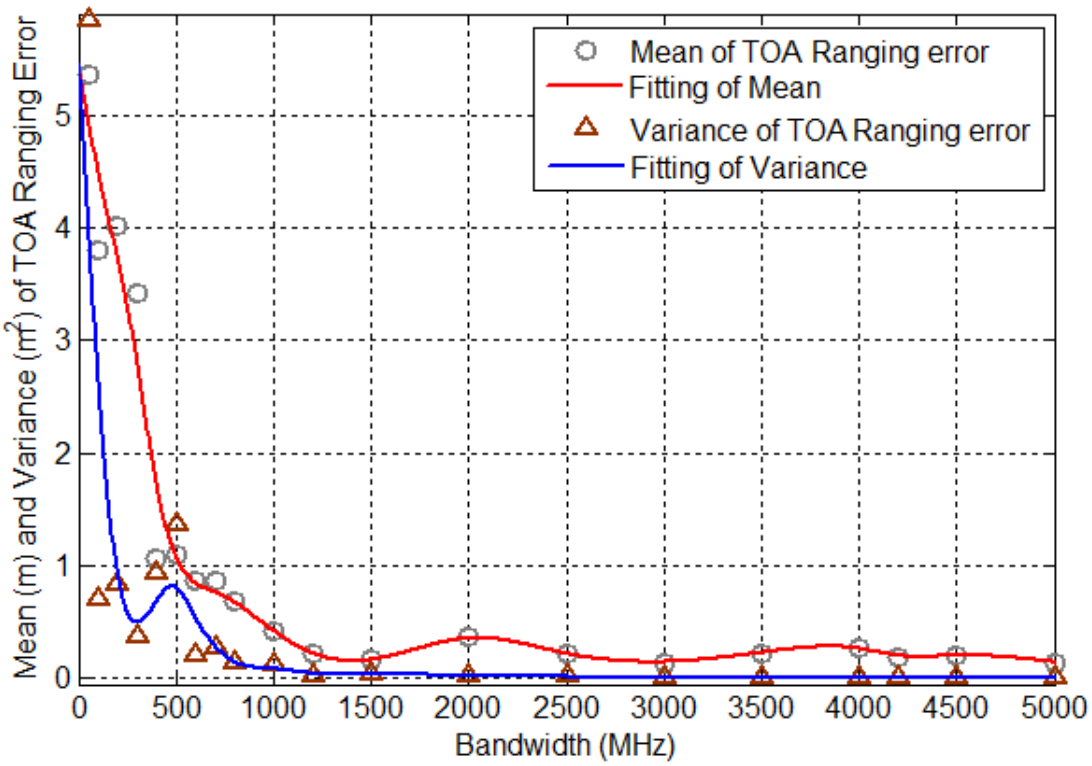

Figure 3.11: Effect of Bandwidth on TOA ranging for body mounted sensor. (a):Chest-mounted scenario.

error can be limited within 0.1934 meters while given only 50MHz bandwidth, the mean error raises up to several meters. The various of variance shows similar trend.

It is worth mentioning that for chest-mounted sensors in Fig 3.11, both mean and variance of the TOA ranging error get stable when the bandwidth is larger than 1.5GHz, meaning that for the given system deployment and multipath environment, using 5GHz of bandwidth is not that necessary. Similar situation can be seen from the wrist-mounted sensor cases in Fig 3.12. When the system bandwidth goes beyong 2GHz, both mean and variance of TOA ranging error converge.

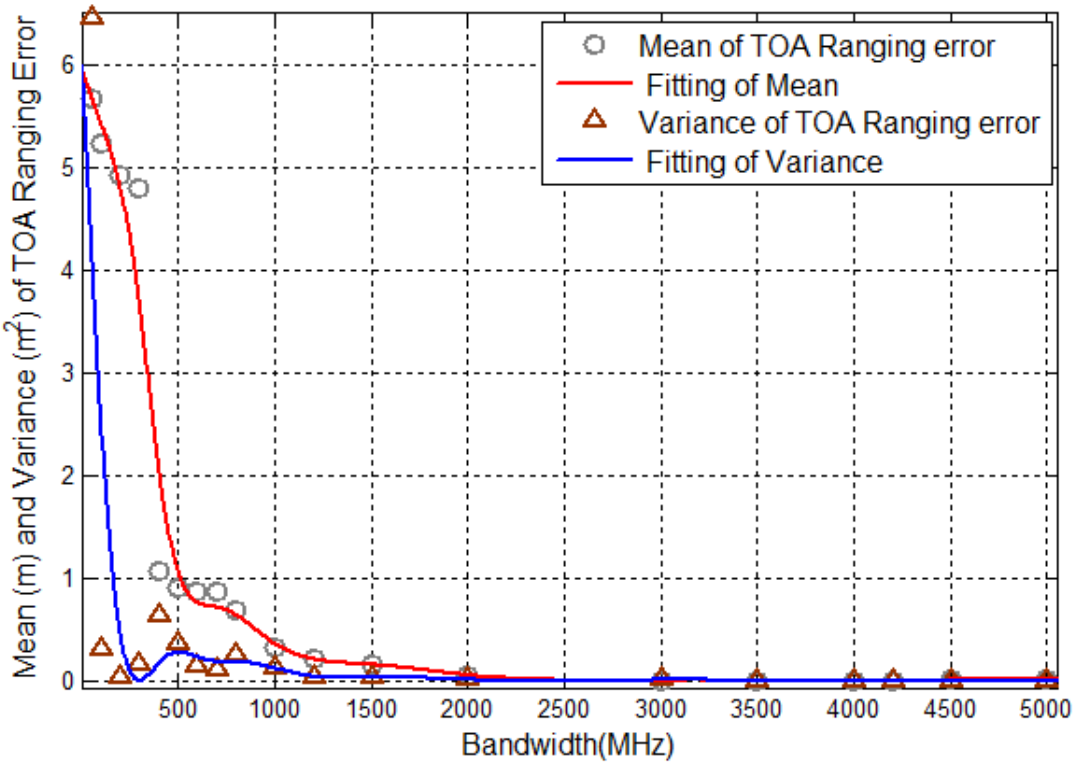

Figure 3.12: Effect of Bandwidth on TOA ranging for body mounted sensor. (b):Wrist-mounted scenario.

3.3.3 Transmit Power.

Signal to noise ratio is another important influence factor to TOA ranging. The higher SNR reduces the effect of multipath on detection of arrival time of first path pulse and thus improve the ranging accuracy. As can be seen from Fig 3.13 and Fig 3.14, the signal to noise ratio also has a strong influence on the TOA ranging performance. In LOS-DDP condition, the changes of SNR_{LOS} has little effect on TOA ranging accuracy; however, in NLOS-UDP condition, since human body would block the direct path and cause creeping wave noise, ranging error increase rapidly with the decrement of SNR_{LOS}. To demonstrate the effect of SNR_{LOS} more clearly, we show the typical curves, which reflect the relationship between SNR_{LOS} and

mean/variance of NLOS-UDP TOA ranging error, in Fig 3.13 and Fig 3.14.

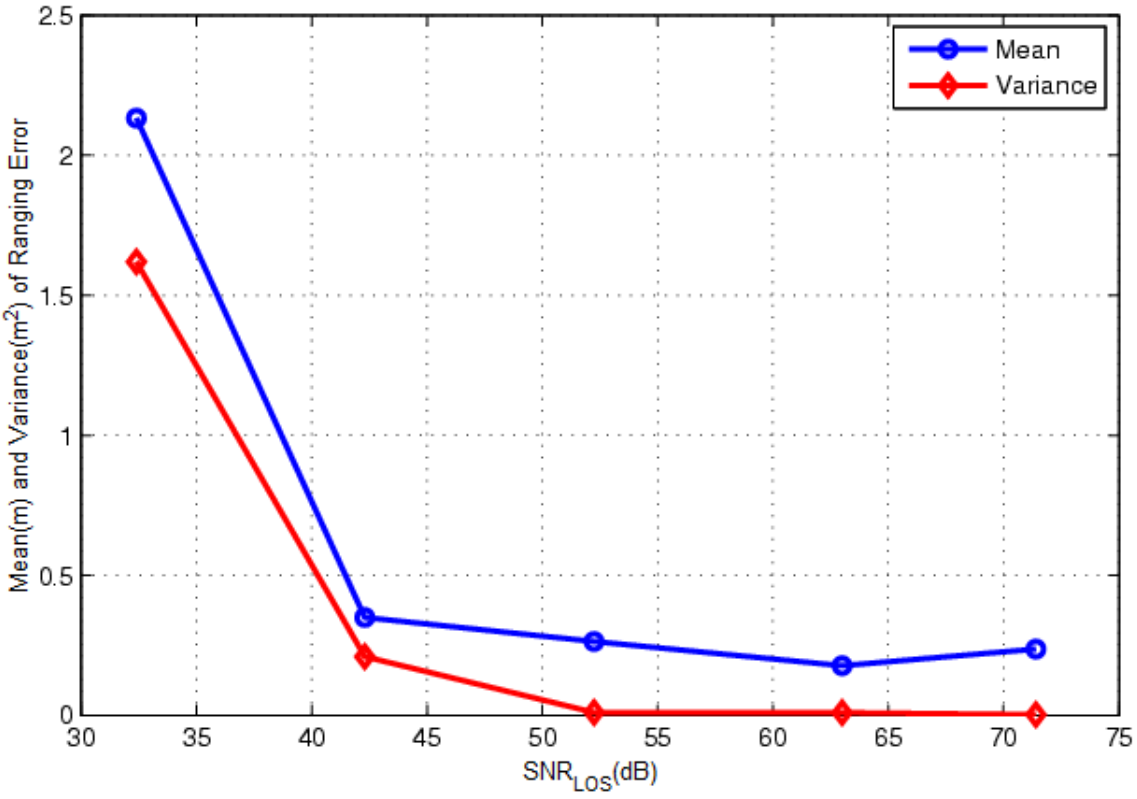

Figure 3.13: Effect of SNR on TOA ranging in NLOS-UDP condition for body mounted sensor. (a):Chest-mounted scenario.

3.4 Modeling the TOA Ranging Error.

The previous section provides general explanation on the effect of human body on the indoor TOA based human tracking system. However, to facilitate the design and evaluation of practical applications, quantitative explanation is required. To fulfill the demand, we build mathematical model for the effect of human body on TOA ranging error.

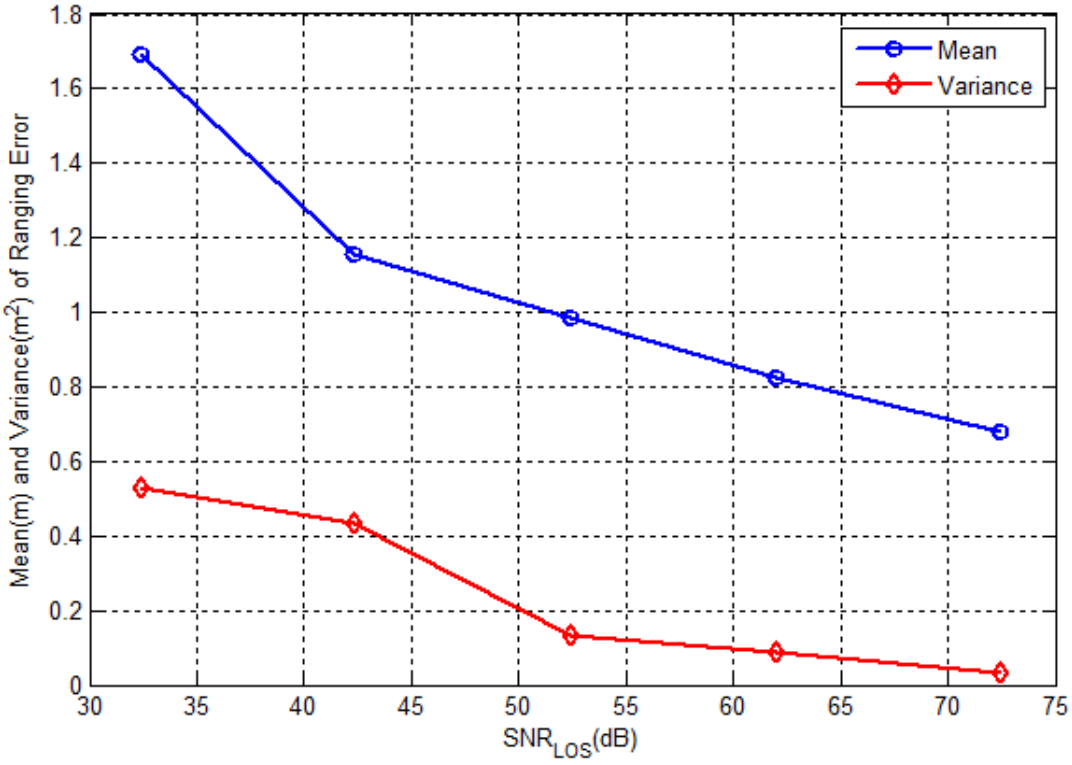

Figure 3.14: Effect of SNR on TOA ranging in NLOS-UDP condition for body mounted sensor. (b):Wrist-mounted scenario.

3.4.1 General Model of TOA Ranging Error.

Based on the above discussion in Section 3.2, the overall TOA ranging error for indoor human tracking can be partitioned into two categories:

- **Multipath error**, always exists in both LOS-DDP and NLOS-UDP condition;
- **UDP error**, which only exits in NLOS-UDP condition.

As a result, the TOA ranging error is given by:

$$e = \epsilon_M + \xi_{\mathbf{UDP}} \times \epsilon_{\mathbf{UDP}} \tag{3.7}$$

where ϵ_M is multipath error that always exists in both LOS-DDP and NLOS-UDP

condition, $\epsilon_{\mathbf{UDP}}$ is UDP error that only exits in NLOS-UDP condition. $\xi_{\mathbf{UDP}}$ is the impulse function, which performs like a switch to determin if the UDP error exists. It takes value of "1" upon the occurrence of NLOS-UDP condition and "0" otherwise.

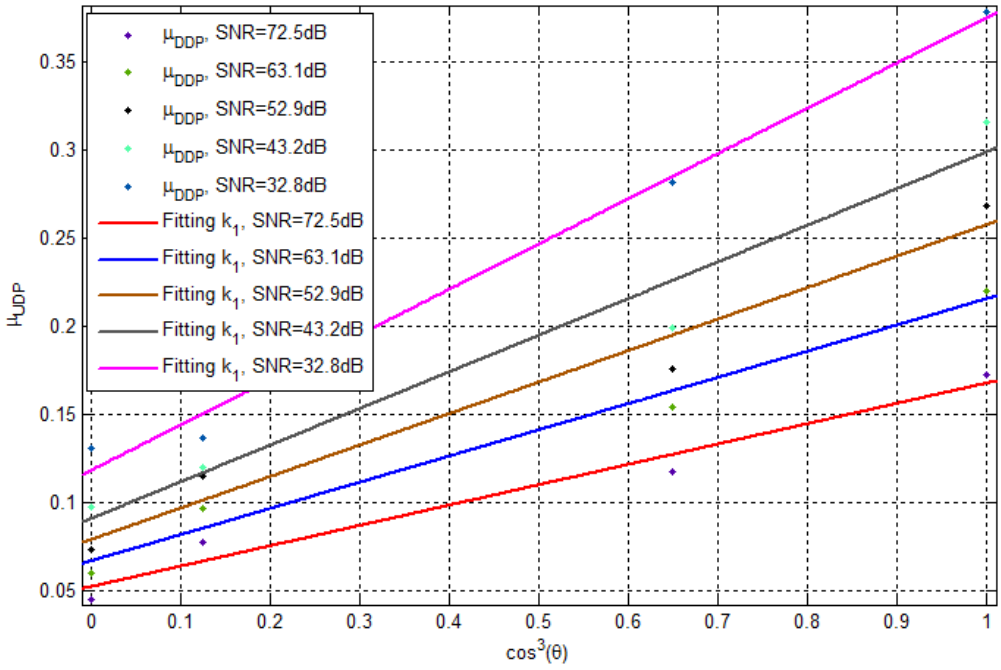

Figure 3.15: Linear fitting results of $\mu_{\mathbf{UDP}}$ and $\sigma^2_{\mathbf{UDP}}$ vs. $\cos^3(\theta)$ in chest-mounted scenario.(a): $\mu_{\mathbf{UDP}}$ vs. $\cos^3(\theta)$.

Multipath error ϵ_M

According to equation (3.7), in the LOS-DDP scenario, the TOA ranging error equals to multipath error. Therefore,ϵ_M can be modeled based on the TOA ranging errors obtained in LOS-DDP scenario. Our measurement result shows that for each bandwidth employed in the subset W, the ranging error forms a Gaussian random variable. Therefore the multipath error can be modeled as:

$$\epsilon_M = G(\mu_{M,W}, \sigma^2_{M,W}) \tag{3.8}$$

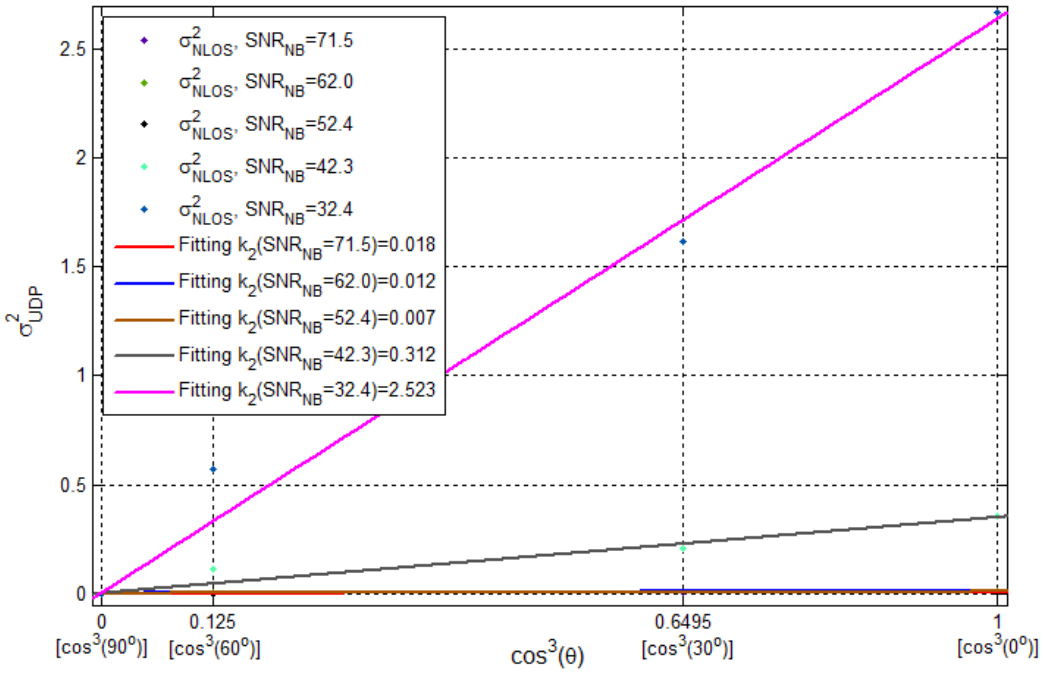

Figure 3.16: Linear fitting results of $\mu_{\mathbf{UDP}}$ and $\sigma^2_{\mathbf{UDP}}$ vs. $\cos^3(\theta)$ in chest-mounted scenario. (b): $\sigma^2_{\mathbf{UDP}}$ vs. $\cos^3(\theta)$.

where G is a Gaussian random variable with mean $\mu_{M,W}$ and variance $\sigma^2_{M,W}$. The values of $\mu_{M,W}$ and $\sigma^2_{M,W}$ varies according to the system bandwidth.

UDP error $\epsilon_{\mathbf{UDP}}$

According to equation (3.7), the TOA ranging error $\epsilon_{\mathbf{UDP}}$ can be given by:

$$\epsilon_{\mathbf{UDP}} = e_{\mathbf{NLOS}} - \epsilon_M \tag{3.9}$$

where $e_{\mathbf{NLOS}}$ is the ranging error in NLOS-UDP condition. Based on our previous observation, both $e_{\mathbf{NLOS}}$ and ϵ_M correspond with Gaussian distributions. Therefore, $\epsilon_{\mathbf{UDP}}$ can be also modeled as a Gaussian random variable, given by:

$$\epsilon_{\mathbf{UDP}} = G(\mu_{\mathbf{UDP}}, \sigma^2_{\mathbf{UDP}}) \tag{3.10}$$

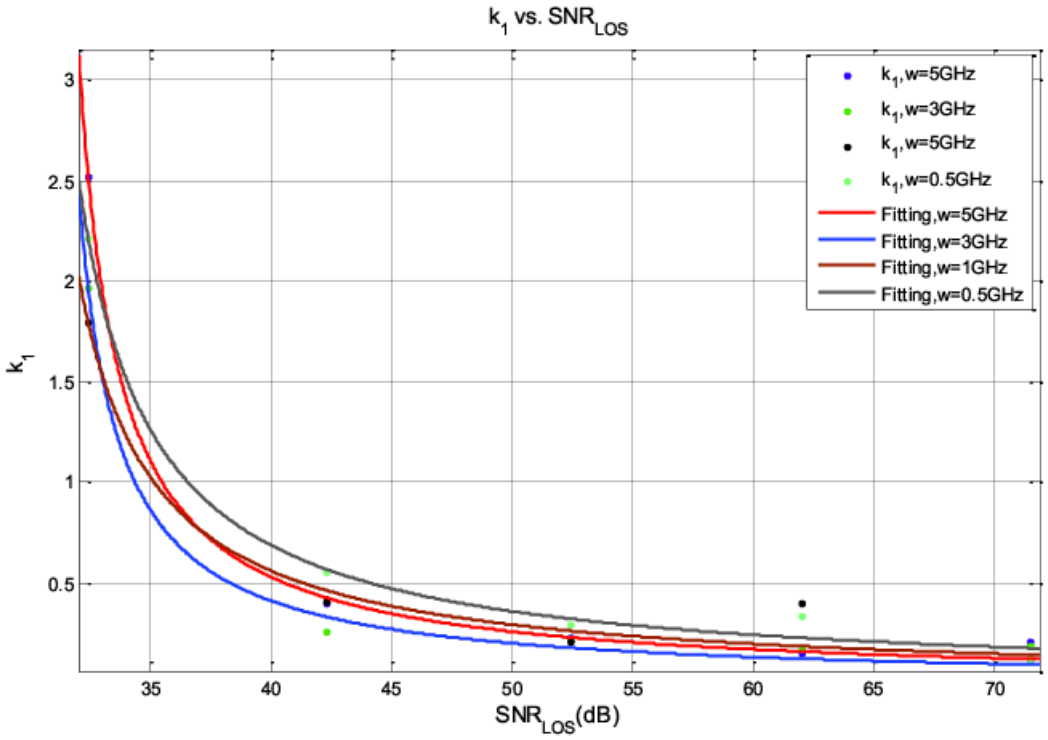

Figure 3.17: Rational fitting results of k_1 and k_2 vs. $\mathrm{SNR_{LOS}}$ in chest-mounted scenario. (a): k_1 vs. $\mathrm{SNR_{LOS}}$.

where the mean and variance of the random variable, $\mu_{\mathbf{UDP}}$ and $\sigma^2_{\mathbf{UDP}}$ can be given by:

$$\mu_{\mathbf{UDP}} = \mu_{e_{\mathbf{NLOS}}} - \mu_M \tag{3.11}$$

$$\sigma^2_{\mathbf{UDP}} = \sigma^2_{e_{\mathbf{NLOS}}} - \sigma^2_M \tag{3.12}$$

where $\mu_{e_{\mathbf{NLOS}}}$ is the mean of $e_{\mathbf{NLOS}}$ and $\sigma^2_{e_{\mathbf{NLOS}}}$ is the variance of $e_{\mathbf{NLOS}}$.

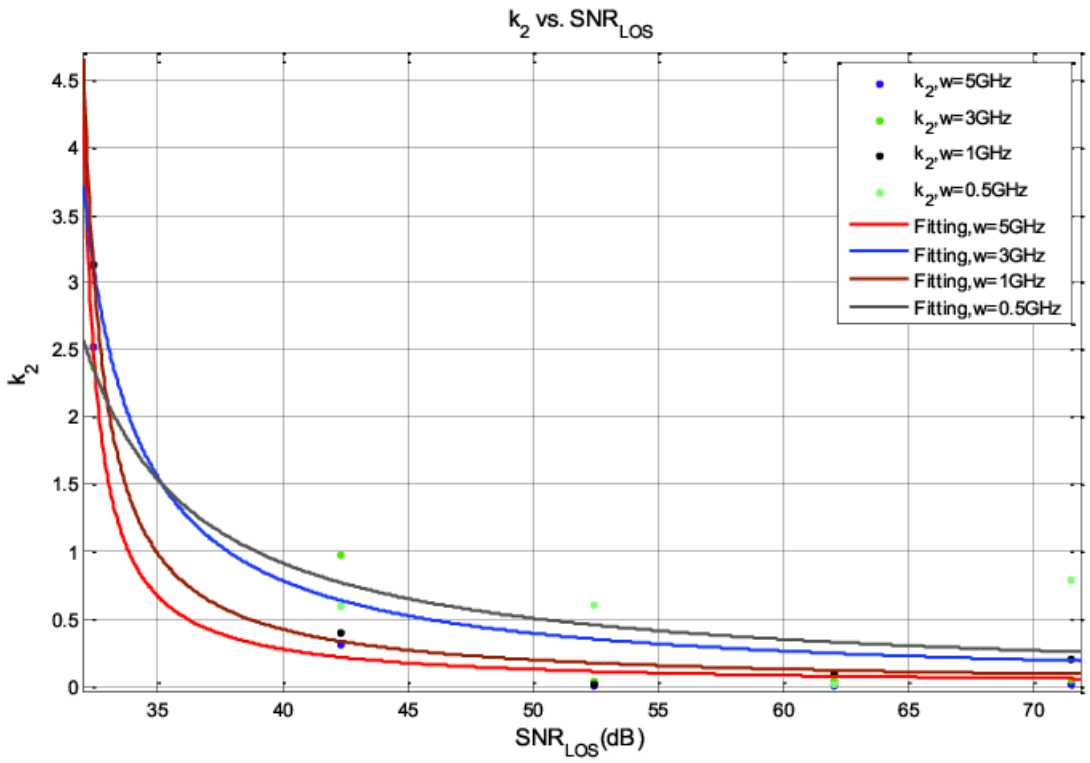

Figure 3.18: Rational fitting results of k_1 and k_2 vs. $\mathrm{SNR_{LOS}}$ in chest-mounted scenario. (b): k_2 vs. $\mathrm{SNR_{LOS}}$.

General Model

According to analysis and the fitting results above, the overall model of TOA ranging error can be given by:

$$e = G(\mu_{M,W}, \sigma^2_{M,W}) + \xi_{\mathbf{UDP}} \times G(\mu_{\mathbf{UDP,\ W}}, \sigma^2_{\mathbf{UDP,\ W}}) \tag{3.13}$$

The parameters of equation (3.13), including $\mu_{M,W}$, $\sigma^2_{M,W}$, $\xi_{\mathbf{UDP}}$, $\mu_{\mathbf{UDP,\ W}}$ and $\sigma^2_{\mathbf{UDP,\ W}}$, should be estimated or formulated to complete the TOA ranging error model. Based on our measurement results in chest-mounted scenario and wrist-mounted scenario, we obtained the values or fitting functions of these parameters for chest-mounted sensor and wrist-mounted sensor respectively.

Table 3.1: Parameters of the TOA ranging error model for chest-mounted sensor.

W(GHz)	$\mu_{M,W}$(m)	$\sigma^2_{M,W}$(m)	a_W	b_W	$\text{SNR}_{Thre,W}$(dB)
5	0.010	0.005	5.10	5.49	30.4
3	0.009	0.001	3.98	6.69	30.4
1	0.072	0.058	6.21	11.76	29.0
0.5	0.138	0.143	14.69	10.62	27.5

Table 3.2: Parameters of the TOA ranging error model for wrist-mounted sensor.

W(GHz)	$\mu_{M,W}$(m)	$\sigma^2_{M,W}$(m)	c_W	d_W	e_W	f_W	bias_W
5	0.085	0.0002	10.01	5.64	27.04	328.3	0.0808
3	0.090	0.0002	9.43	-11.40	16.41	156.6	0.0849
1	0.155	0.006	22.27	-2.51	15.78	135.3	0.1736
0.5	0.324	0.0034	21.68	-13.6	15.24	114.4	0.4309

3.4.2 TOA Ranging Model for Chest Mounted Sensors.

$\mu_{M,W}$ and $\sigma^2_{M,W}$

For chest-mounted scenario, $\mu_{M,W}$ and $\sigma^2_{M,W}$ for the selected bandwidths are estimated based on the measured data while $\theta \in [90^o, 270^o]$, which indicates the channel is with LOS-DDP condition. Typical values have been listed in Table 3.1.

Impulse Function $\xi_{\mathbf{UDP}}$

In chest-mounted scenario, it can be defined as:

$$\xi_{\mathbf{UDP}}(\theta) = \begin{cases} 1, & \theta \in [0^o, 90^o) \textbf{ or } \theta \in (270^o, 360^o] \\ 0, & \theta \in [90^o, 270^o] \end{cases} \tag{3.14}$$

UDP Parameter $\mu_{\mathbf{UDP}}$ and $\sigma^2_{\mathbf{UDP}}$

As can be seen from Fig 3.7 and Fig 3.8, the plot of both $\mu_{\mathbf{UDP}}$ and $\sigma^2_{\mathbf{UDP}}$ in chest-mounted scenario result share a similar trend with the function $\cos^a(\theta)$. Con-

sequently, after mathematical work, for given W and $\mathrm{SNR_{LOS}}$, we model both $\mu_{\mathbf{UDP}}$ and $\sigma^2_{\mathbf{UDP}}$ as a linear function of $\cos^3(\theta)$ as follows:

$$\mu_{\mathbf{UDP}} = k_1 \times \cos^3\theta \tag{3.15}$$

$$\sigma^2_{\mathbf{UDP}} = k_2 \times \cos^3\theta \tag{3.16}$$

where k_1 and k_2 are the slope of the linear functions. Fig 3.15 and Fig 3.16 shows the fitting results of $\mu_{\mathbf{UDP}}$ and $\sigma^2_{\mathbf{UDP}}$ versus θ when $W = 5GHz$. As depicted in Fig 3.17 and Fig 3.18, k_1 and k_2 increase as $\mathrm{SNR_{LOS}}$ declines, indicating that the effects of body-caused UDP error is relatively severe in low SNR conditions. We believe that in low SNR situation, path detection is rather challenging because of the difficulty in properly setting up a threshold. In such low SNR situation, detection failure occurs more frequently. The coefficients k_1 and k_2 can be then modeled as a rational function of $\mathrm{SNR_{LOS}}$ as follows:

$$k_1 = \frac{a_W}{\mathrm{SNR_{LOS}} - \mathrm{SNR}_{\mathbf{Thrd,\ W}}} \tag{3.17}$$

$$k_2 = \frac{b_W}{\mathrm{SNR_{LOS}} - \mathrm{SNR}_{\mathbf{Thrd,\ W}}} \tag{3.18}$$

where a_W, b_W and $\mathrm{SNR}_{\mathbf{Thrd,\ W}}$ are the coefficients depend on system bandwidth W. One thing worth mentioning is that $\mathrm{SNR}_{\mathbf{Thrd,\ W}}$ shows the threshold of $\mathrm{SNR_{LOS}}$ for TOA ranging in body-caused NLOS-UDP scenario. If the SNR goes below the threshold in our model, reception failure of the reference nodes dramatically increases and peak detection becomes very difficult. Values of a_W, b_W and $\mathrm{SNR}_{\mathbf{Thrd,\ W}}$ are calculated by curve fitting are shown in Table 3.1. Fig 3.17 and Fig 3.18 show the fitting results of k_1 and k_2 versus $\mathrm{SNR_{LOS}}$ when system bandwidth $W = 5GHz$.

If we put together equations (3.15),(3.16),(3.17) and (3.18), $\mu_{\mathbf{UDP,\ W}}$ and $\sigma^2_{\mathbf{UDP,\ W}}$

can be finally given by:

$$\mu_{\mathbf{UDP,\ W}} = \frac{a_W}{\mathrm{SNR_{LOS}} - \mathrm{SNR_{\mathbf{Thrd,\ W}}}} \times \cos^3(\theta) \tag{3.19}$$

$$\sigma^2_{\mathbf{UDP,\ W}} = \frac{b_W}{\mathrm{SNR_{LOS}} - \mathrm{SNR_{\mathbf{Thrd,\ W}}}} \times \cos^3(\theta) \tag{3.20}$$

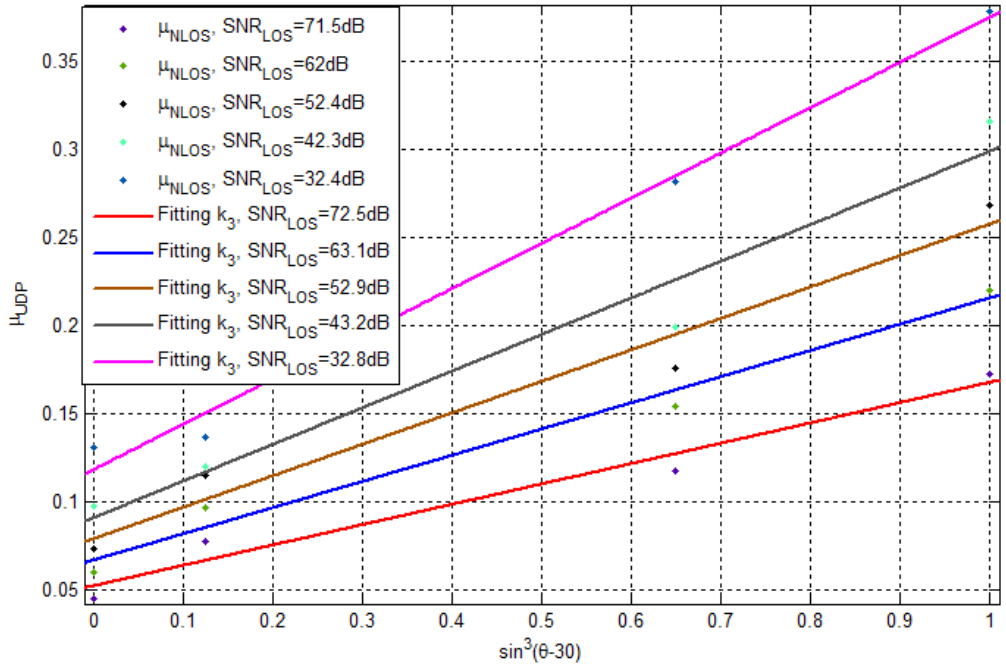

Figure 3.19: Linear fitting results of $\mu_{\mathbf{UDP}}$ and $\sigma^2_{\mathbf{UDP}}$ vs. θ in wrist-mounted scenario.(a): $\mu_{\mathbf{UDP}}$ vs. $\sin^3(\theta - 30)$.

3.4.3 TOA Ranging Model for Wrist Mounted Sensors.

$\mu_{M,W}$ and $\sigma^2_{M,W}$

Similar to chest-mounted scenario, values of these two parameters for wrist-mounted sensor are estimated based on the measured data of LOS-DDP condition, while $\theta \in [0^o, 180^o)$. The typical values have been listed in Table 3.2.

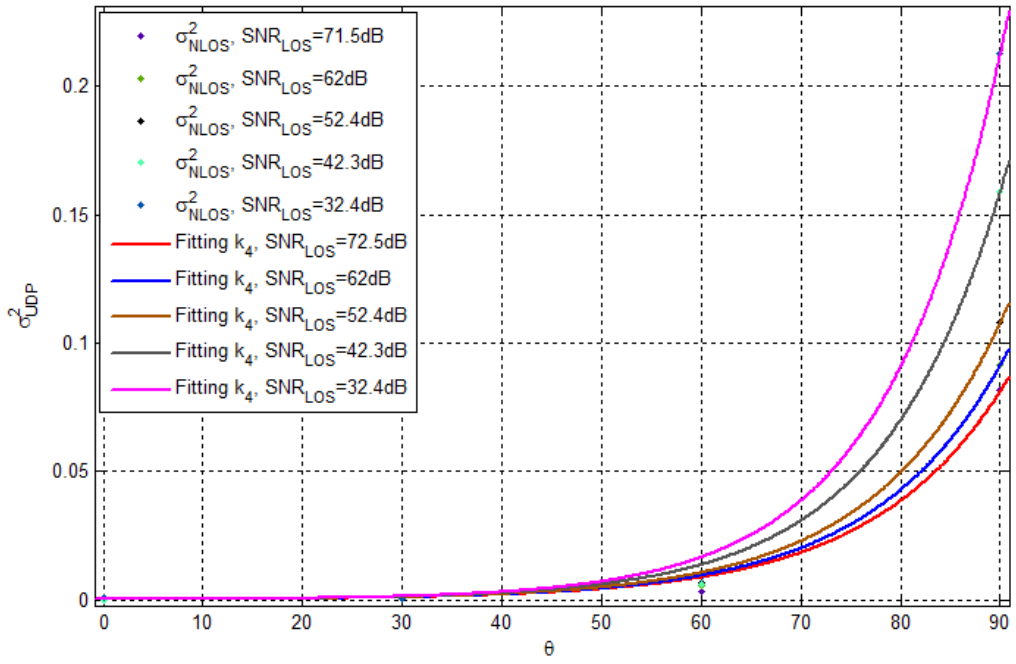

Figure 3.20: Linear fitting results of $\mu_{\mathbf{UDP}}$ and $\sigma^2_{\mathbf{UDP}}$ vs. θ in wrist-mounted scenario. (b): $\sigma^2_{\mathbf{UDP}}$ vs. θ.

$\xi_{\mathbf{UDP}}$

In wrist-mounted scenario, $\xi_{\mathbf{UDP}}$ can also be defined as a function of θ:

$$\xi_{\mathbf{UDP}}(\theta) = \begin{cases} 1, & \theta \in [0^o, 180^o) \\ 0, & \theta \in [180^o, 360^o) \end{cases} \tag{3.21}$$

UDP Parameter $\mu_{\mathbf{UDP}}$ and $\sigma^2_{\mathbf{UDP}}$

As can be seen from Fig 3.9 and Fig 3.10, in the NLOS-UDP part of our measurement result, both $\mu_{\mathbf{UDP}}$ and $\sigma^2_{\mathbf{UDP}}$ are symmetric of specific angle. The symmetry axis of $\mu_{\mathbf{UDP}}$ is around 120^o and symmetry axis of $\sigma^2_{\mathbf{UDP}}$ is obviously 90^o. Moreover, due to the symmetry feature of NLOS-UDP part of Fig 3.9, it can be easily modeled by using symmetric functions.

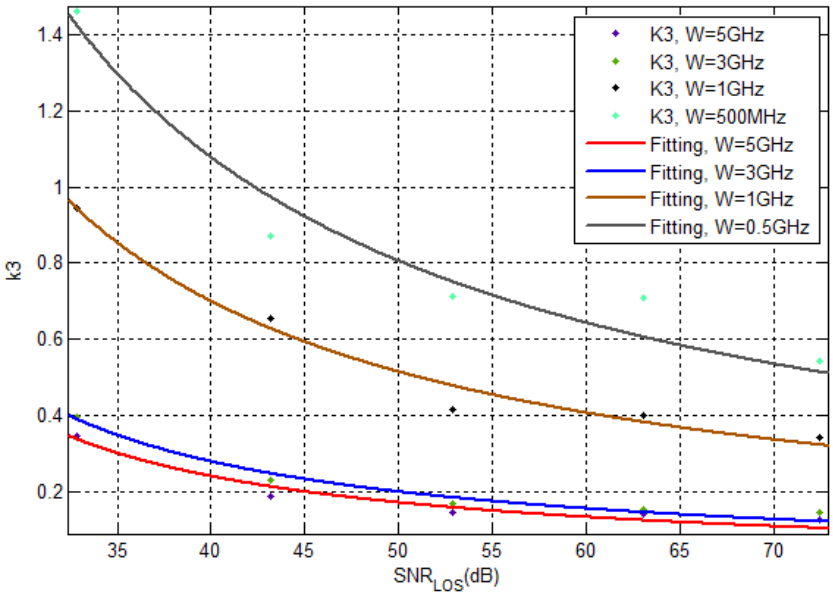

Figure 3.21: Rational fitting results of k_3 and k_4 vs. $\mathrm{SNR_{LOS}}$ in wrist-mounted scenario. (a): k_3 vs. $\mathrm{SNR_{LOS}}$.

For given W and $\mathrm{SNR_{LOS}}$, $\mu_{\mathbf{UDP}}$ has the same shape of function $sin^3(\theta - 30^o)$, which indicates that it can be linearly modeled by $sin^3(\theta - 30^o)$. For given W and $\mathrm{SNR_{LOS}}$, the shape of $\sigma^2_{\mathbf{UDP}}$ is too sharp to be modeled by $sin^3(\theta)$, that we use exponential function to model it. The expression for $\mu_{\mathbf{UDP}}$ and $\sigma^2_{\mathbf{UDP}}$ are given as follow:

$$\mu_{\mathbf{UDP}} = k_3 \times \sin^3(\theta - 30^o) + bias_W \tag{3.22}$$

$$\sigma^2_{\mathbf{UDP}} = 10^{-5} \times e^{k_4 \theta} \tag{3.23}$$

in which k_3 is the slope of linear function, $bias_W$ is the intercept of linear function and k4 is the exponent. Fig 3.19 and Fig 3.20 shows the fitting results of $\mu_{\mathbf{UDP}}$ vs. θ and $\sigma_{\mathbf{UDP}}$ vs. θ with a fixed bandwidth of 5GHz. The fitting result shows that the coefficient k_3 and k_4 increase with the decrease of $\mathrm{SNR_{LOS}}$, indicating that the blockage of human body increases in low $\mathrm{SNR_{LOS}}$ condition. Coefficients k_3 and k_4

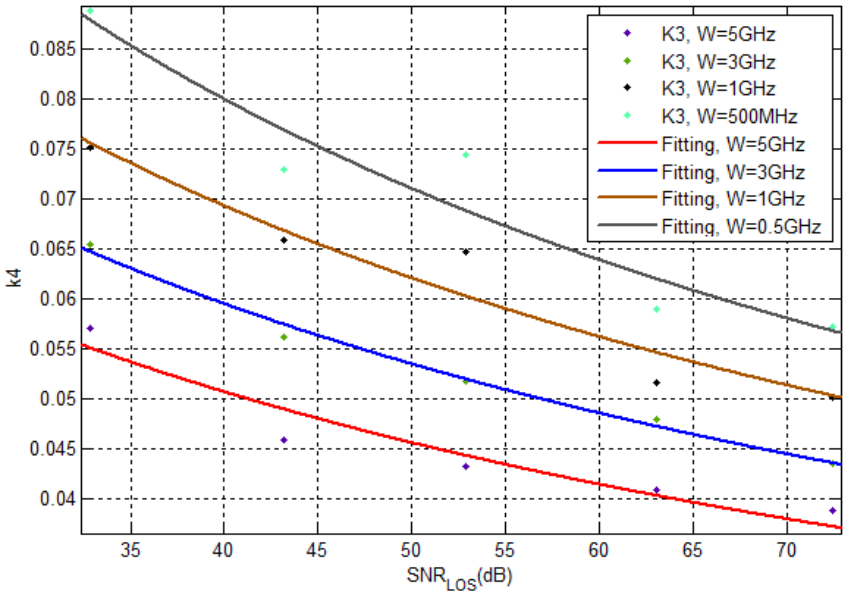

Figure 3.22: Rational fitting results of k_3 and k_4 vs. $\mathrm{SNR_{LOS}}$ in wrist-mounted scenario. (b): k_4 vs. $\mathrm{SNR_{LOS}}$.

are worked out as a rational function of $\mathrm{SNR_{LOS}}$ as follow:

$$k_3 = \frac{c_W}{\mathrm{SNR_{LOS}} - d_W} \tag{3.24}$$

$$k_4 = \frac{e_W}{\mathrm{SNR_{LOS}} - f_W} \tag{3.25}$$

in which c_W, d_W, e_W and f_W are parameters based on system bandwidth W in our model. The curve fitting results for k_3 and k_4 are shown in Fig 3.21 and Fig 3.22, and all these parameters are listed in Table 3.2. According to equation (3.22), (3.23), (3.24) and (3.25), then we get:

$$\mu_{\mathbf{UDP}} = \frac{c_W}{\mathrm{SNR_{LOS}} - d_W} \times \sin^3(\theta - 30^\circ) + bias_W \tag{3.26}$$

$$\sigma^2_{\mathbf{UDP}} = 10^{-5} \times e^{\frac{e_W}{\mathrm{SNR_{LOS}} - f_W} \times \theta} \tag{3.27}$$

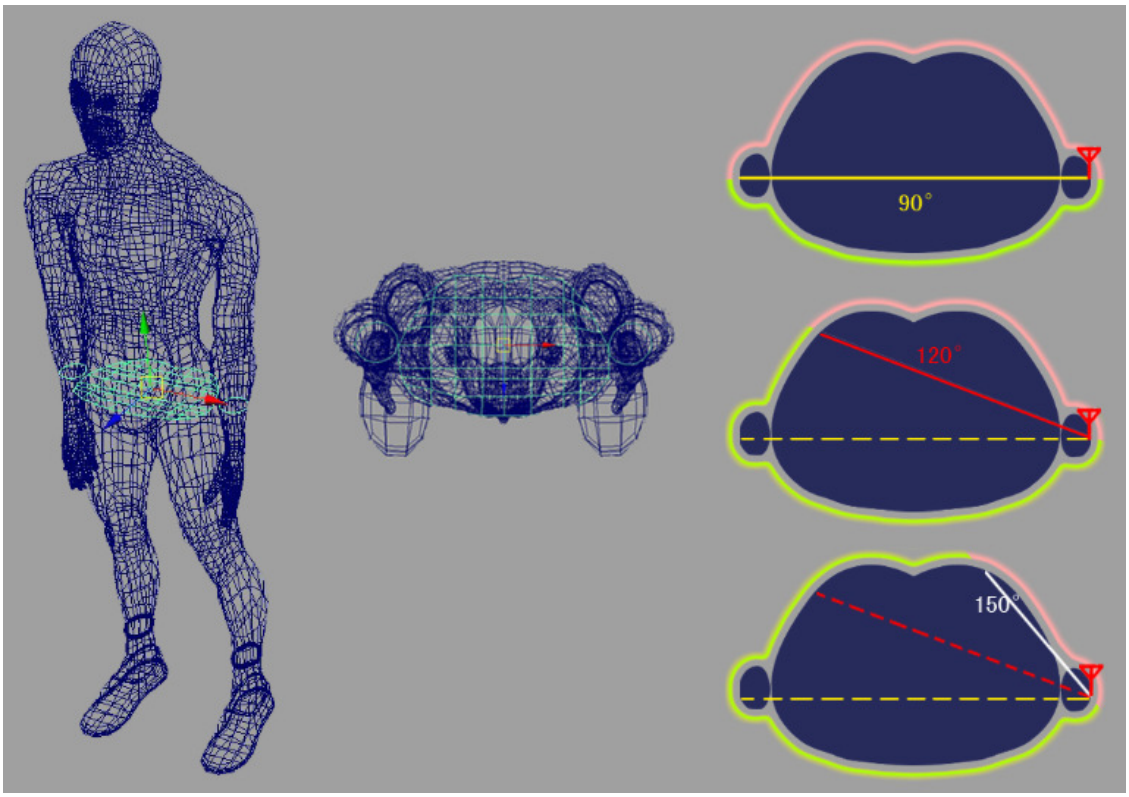

Figure 3.23: Creeping Wave Around Human Body.

3.4.4 Comparison and Validation.

Comparison.

By comparing equation (3.19) and equation (3.26), it is easy to notice that the wrist has a 30^o bias on the symmetry axis and an extra intercept on the expression of mean value for all bandwidth options. To explain the bias on symmetry axis, sectional view of human body is provided in Fig 3.23 with two major creeping waves around human body in green and pink. From Fig 3.23 we see that different from human chest scenario, when the antenna is attached to human wrist, the sectional view is no longer symmetric. The maximum mean error is supposed to appear at the time when two major waves travels the same distance. However, at 90^o, the pink wave

travels a lot more than the green one. Due to the fact that the midpoint is located at approximately 120^o, the maximum mean error appears at that angle. Apart from that, the intercept on mean value may come from the undesirable propagation channel between human wrist and human trunk.

As for the different expression pattern of variance, at 90^o and 150^o there is only a mere part of human body blocking the direct line of sight between TX and RX, resulting in a relatively small variance and the change of variance is too sharp to be modeled by $sin^3(\theta)$, resulting in an exponential function.

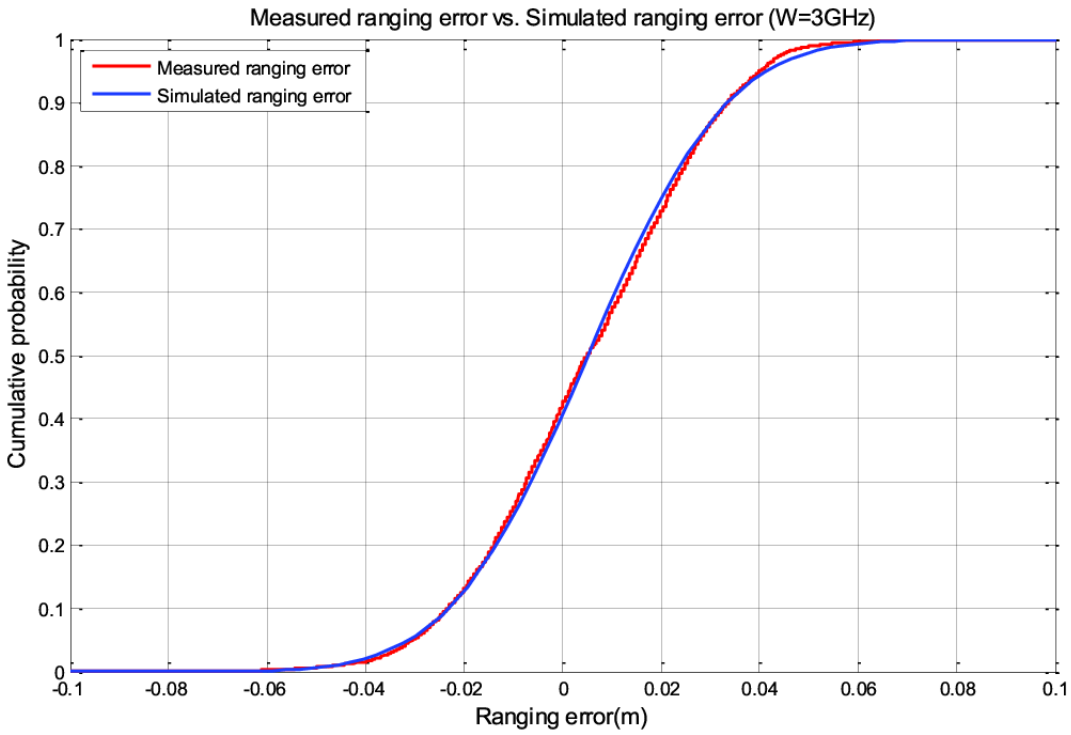

Figure 3.24: Comparison between empirical measurement result and software simulation result using the model presented above. (a): Comparison of CDF in LOS-DDP condition.

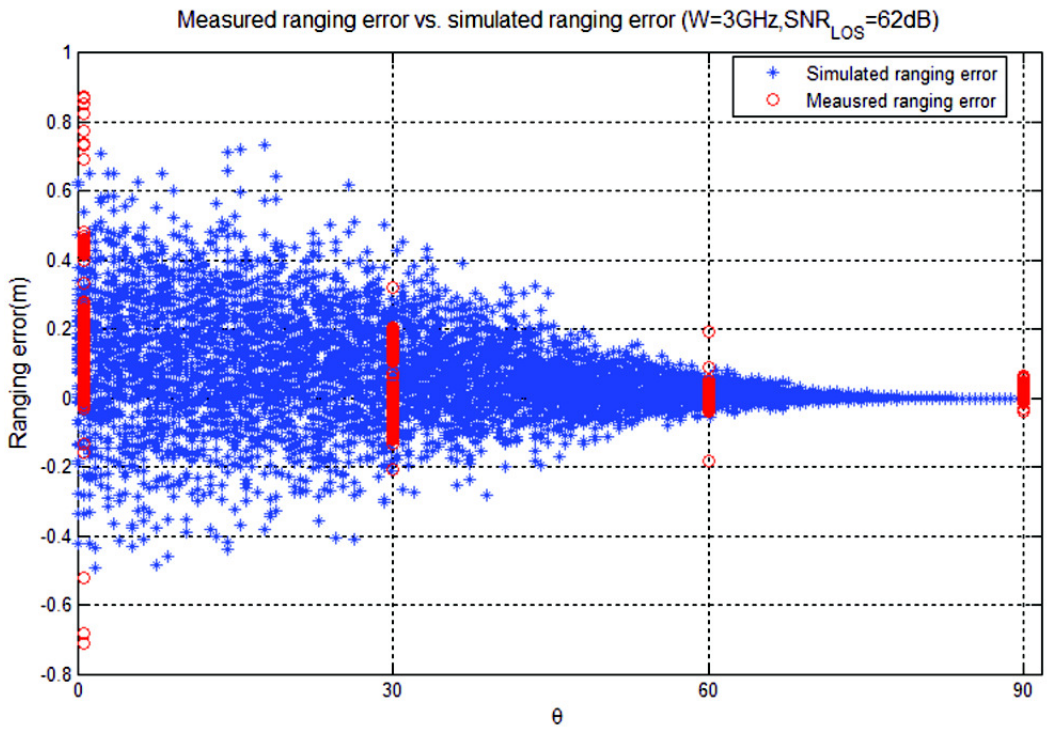

Figure 3.25: Comparison between empirical measurement result and software simulation result using the model presented above. (b): Comparison of TOA ranging error in NLOS-UDP condition.

Validation.

Comparison between simulated result from our model and empirical measurement data has been made in the purpose of model validation. CDFs of ranging error for both LOS-DDP and NLOS-UDP condition are presented in Fig 3.24, in which we take $\{Chest, W = 3GHz, SNR = 62dB\}$ case as an example. The validation result in Fig 3.24 shows that for LOS-DDP condition, our model perfectly matches the measurement data. For NLOS-UDP condition, as shown in Fig 3.25, we simulate 10000 ranging errors(blue star), θ of which randomly varies from 0^o to 90^o. The original measured ranging errors(red circle) with $\theta = 0^o, 30^o, 60^o, 90^o$ are also plotted in the figure to show a whole vision of comparison. Close agreement between

simulation and measurement result still exists.

3.5 Summary.

In this section, we measured and analyzed the effect of human body on TOA ranging of its mounted sensor in a typical office environment. Specially, both chest-mounted sensor and wrist-mounted sensor, results shows that the ranging error of NLOS-UDP condition is significantly related to the angle between facing direction and direction of TX-RX; the ranging error of LOS-DDP condition is almost not influenced by the human body. Then, the ranging error of chest-mounted sensor and wrist-mounted sensor are modeled based on the statistical result of the original measured data. This model separates the ranging error into multipath error and UDP error, which is caused by the penetration loss of the human body and the creeping wave around human body. Both multipath error and UDP error are modeled as a Gaussian random variable. The distribution of multipath error is related to bandwidth of the system while the distribution of UDP error is related to the angle between the human facing direction and the direction of TX-RX, $\mathrm{SNR}_{\mathrm{LOS}}$ and bandwidth of the system, which clearly shows the effects of human body on TOA ranging. The comparison between the empirical ranging error and simulated ranging error depicts close agreement, proving the validity of the TOA ranging error for body mounted sensors.

The contribution of this section is three-folded. First and foremost, this work is the first one that considers the effect of human body on TOA ranging error of indoor human tracking system. Secondly, creeping wave phenomenon has been discussed in the result analysis section. Last but not the least, it is the first time that the horizontal angle θ has been selected as a parameter instead of the frequently used

distance between TX and RX in the literature. We are currently at the initial phase of this research and our ultimate goal is to fully understand the effect of human body and eliminate the inaccuracy raised by human body. As for future work, since with a chest mounted sensor, the human body can be regarded as a symmetric structure and the range of angle θ can be limited within 180^o. Whenever the sensors are attached to human wrist and ankle or even located in the pocket, the symmetry will no longer exist. We intend to research how the location of target sensor influences the TOA ranging error in the coming future. Moreover, wireless channel model for typical indoor environment has been widely used in current localization applications. To further improve the localization accuracy and especially enable the ray-tracing technique with human body module, we also plan to model the combined channel with human body for UWB frequency band.

Chapter 4

On-Body Radio Propagation and Human Motion Classification Using Support Vector Machine.

The rapid advancements in wireless technology, implantable medical devices and pervasive computing give birth to a booming era of body area network (BAN) as well as its most distinguished application, real-time on-body health monitoring systems [IJZ04]. Such monitoring networks consist of a set of low power, small size, wearable sensors measuring physiological signals of the subject and a central unit that collects data from the sensors through the wireless connection [PB10]. Smart phones and PDAs are often selected as the central unit for their natural wireless functionality, computational capability and access to local/wide area network.

Real-time health monitoring is of great help to people suffering cardiac and kidney diseases. The real-time physiological status reports and notifications facilitate physicians. Early detection of abnormal motion guarantees that the patients get immediate treatment in emergency situations [VRTH09]. The health monitoring

system not only exhibits promising performance in the hospital setting, but also can be assigned to first responders working in harsh environments. Take the Physiological Health Assessment System for Emergency Responders (PHASER) [GCP13] as an example[1]. Such out-of-hospital applications are an unprecedented advancement in systematic risk identification, prioritization, and intervention. First responder (emergency responder) in this work denotes a person who has completed a course and received certification in providing pre-hospital care for medical emergencies such as police officers and firefighters. The monitoring system in this work is primarily designed for firefighters. When firefighters work in a burning house, it is essential not only to monitor their physiological condition but also to detect behavioral abnormalities that demand attention and assistance.

The physical demands placed on first responders make it challenging to design motion classification systems for them. Clearly, to guarantee that the normal activities of first responders are not hindered or even affected by the motion classification devices, it is necessary to minimize the size, weight and count of on-body sensors. Such requirements restrain the use of traditional approaches with cumbersome accelerometers [SJ04][LSH+09] or gyroscopes [ARZ+13][CJ13], and instead, necessitating the exploration of highly compact sensor nodes or even existing infrastructure. The one sensor class that defines the minimum sensor set naturally available in almost all on-body health monitoring devices is the radio frequency (RF) transceiver which communicates between sensor nodes and the central unit [PB10]. It is capable of establishing waveform transmission and sensing changes or fluctuations in a received RF signal. Radio waves can be blocked, reflected or scattered at different parts of the human body and the signal components from distinct propagation paths

[1]Physiological Health Assessment System for Emergency Responders (PHASER) is a program conducted by University of California Los Angeles (UCLA). PHASER program is sponsored by Department of Homeland Security (DHS), details can be found at http://phaser.med.ucla.edu/.

add up to form a channel profile [GHDP13][AKKM14][GHP13]. When specific body movement occurs, the changes in the propagation environment generate characteristic patterns in the received channel profile accordingly [FYP12]. By identifying and interpreting these patterns, it is possible and promising to detect and classify human motions.

In this study, we define the proposed RF-based motion classification approach as an application which recognizes various human motions using analysis of on-body radio signals while the person himself is not required to carry any extra devices other than the health monitoring system. We focus on classification for both static and dynamic motion of individuals, specifically first responders, by exploiting RF signals collected from the on-body health monitoring sensor network. Empirical measurement of the on-body propagation channel has been conducted with the subject wearing standard fire-proof clothing and equipment. The subject performed seven frequently appearing motions of firefighters including standing, walking, running, lying, crawling, climbing and running on the stairs. A time domain channel profile of the on-body sensor network has been recorded to calculate candidate RF features for motion classification. A multi-class Support Vector Machine (SVM) using Gaussian Kernel has been implemented and achieved a general true classification rate of 88.69%.

Compared with preliminary results on general human motion classification approaches posted in recent research [SSS+14][KL09][SSK13], it is worth mentioning that the novel contributions of this study are three-folded:

1. This study proposes the first motion classification application designed for first responders in emergency operations that does not require any system deployment in advance.

2. This study achieves the first complete implementation of a motion classification scheme on top of on-body health monitoring sensor networks, utilizing characteristics of on-body RF propagation.

3. This study provides the first in-depth investigation on motion classification accuracy with respect to the effects of various candidate human motions and multiple sensor locations.

The majority of features considered in this study are Received Signal Strength (RSS), Doppler spectrum, channel fluctuation coefficients and the higher order statistics of the coefficients. Related values are captured by contemporary transceiver hardware and can be obtained from any existing implementation of an on-body monitoring system by nature. With the rapid commercialization of wearable physiological sensor products, such approach can be even generalized to various applications beyond first responders.

Our further discussions are structured as follows. Existing literature toward human motion classification with a particular focus on RF features is reviewed in section 4.1. Typical user-case scenario, candidate motions, available sensor locations and experimental systems are discussed in section 4.2. The RF features utilized in this study are introduced, analyzed and discussed in section 4.3. A correlation check and an all-data-at-once SVM implementation are discussed in chapter 4.4 based on the extracted RF feature vectors. Most significantly, the classification performance is reported and carefully investigated in section 4.5 and the effects of different candidate motions and different sensor locations are analyzed. Section 4.6 summarizes the overall work and closes our discussion.

4.1 Background.

Motion detection and classification is a typical way to recognize human motion by utilizing various sensor readings. A broad and general definition of sensor has been applied for this task. Traditionally, devices with inertial sensors have been the most commonly used equipment for motion detection due to their convincing classification rate and simplified practical implementation [GJP10][CMP+13]. General research challenges such as automated recognition system design [PHR+12], accurate classification on noisy data captured in the real world [BI04] and adaptability to inter subject behavior difference [CSSK+13] attracted enormous attention from the research community. In recent works, approaches using temporal transition models have been proposed to optimize the systematic performance [WDX07][JLT09]. A major issue with the traditional approach is that readings of inertial sensors or gyroscopes are not complex enough to fully capture the characteristics of complicated human motions to the point that most of the applications can only distinguish a single specific human motions from all the other activities in daily life, such as fall detection in most cases [LSH+09][ARZ+13][CJ13][GJP10][CMP+13].

The various challenges raised by the traditional motion classification system has led to the revolution of environmental sensing modality. Vision based applications employing image processing technique have been adopted since the beginning of the 2000s [MHK06b][Pop10]. They lit up the booming era of human activity monitoring in which even the Microsoft Kinect concepts were employed by researchers and scientists for motion detection and classification [LL13][BLA08]. Significant improvement on classification rate has been achieved by various elegantly designed algorithms [LRE10][GLY11][DC13] and multi-motion classification was made available. However, the scalability of that approach was naturally limited by the requirement

of pre-installation of the entire system. As a result, vision based motion detection and classification turned out to become a site-specific approach deployed only for critical cases [MSKS13][RMSAR11][AMSA+11]. To avoid the pre-deployment process and maximize the utilization of existing infrastructures, researchers started to explore alternative sensing methods based on a readily available medium.

With the gracefully structured theoretical foundations, RF signals are considered an ideal medium for remote sensing and they have been recently utilized for motion classification from different perspectives [WWZ+13][WWL12][XFM13][PBT+14]. Sigg et al. [SSS+14] for instance, proposed a motion classification scheme for a device-free radio-based activity recognition system. Exploiting 900MHz and 82.5Hz RF signals, the classification scheme achieved around a 75% average classification rate in 2.2m proximity by simply locating a RF receiver in the environment. Through-wall imaging radar [SYL05][SSP08] is another frequently used approach that employ wide band signal transmission to achieve high-resolution imaging in the down-range dimension and therefore track the real-time human motion. In addition, Lin and Ling [LL07] proposed a doppler radar scheme as an excellent approach for detecting and classifying human movements while suppressing stationary clusters in the background. Such approaches can be implemented by low-cost, off-the-shelf components or even single-chip modules available in the market. More recently, the appearance of the micro-doppler signature has been reported containing valuable information related to non-rigid-body movements. Attempts were widely made to exploit the micro-doppler feature for motion detection [KL09][Ote05].

Though the off-body RF features have been heavily investigated as a tool for motion classification, little work can be found investigating the usefulness of on-body RF signals the open literature. As a branch of BAN, the on-body radio propagation channel model has been studied heavily [WTK+09][FDD+06], which provides es-

sential parameters including pathloss gradient, shadowing factor, path arrival rate, etc. [MF04][Tg610][GHWP13]. Moreover, dynamic on-body channel characteristics such as doppler spread, coherence time, etc. have been also reported by Fu et al. in [FYP12]. In this presented study, we pose a different research question, namely, whether or not it is possible to distinguish various human motions based on the on-body RF propagation channel characteristics. The reliable classification of simple human motions may be the first step toward addressing the complicated yet important question of determining human intent.

4.2 Methodology.

4.2.1 Candidate Motions.

The frequently appearing motions for firefighters include standing, walking, running and etc. To safe life and properties, they may also climb ladders, crawl on the floor and run up/down stairs. In some extreme scenario, firefighters may get injured, lying on the floor and unable to move. It is of great value to monitor the real-time behavioral status of firefighters and classify their motions. We can guarantee the safety of firefighters and on the other hand provide necessary aid in time. The ultimate goal of this chapter is to classify seven frequently appeared motions defined as follows:

- **Standing:** The subject remain standing still with transmitter and receiver antenna attached to specific location on body surface. Only respiratory and palpitation occur. Subconsciously movement of limbs are possible and subconsciously movement of human torso can be ignored.

- **Walking:** The subject is expected to walk with arms and feet moving peri-

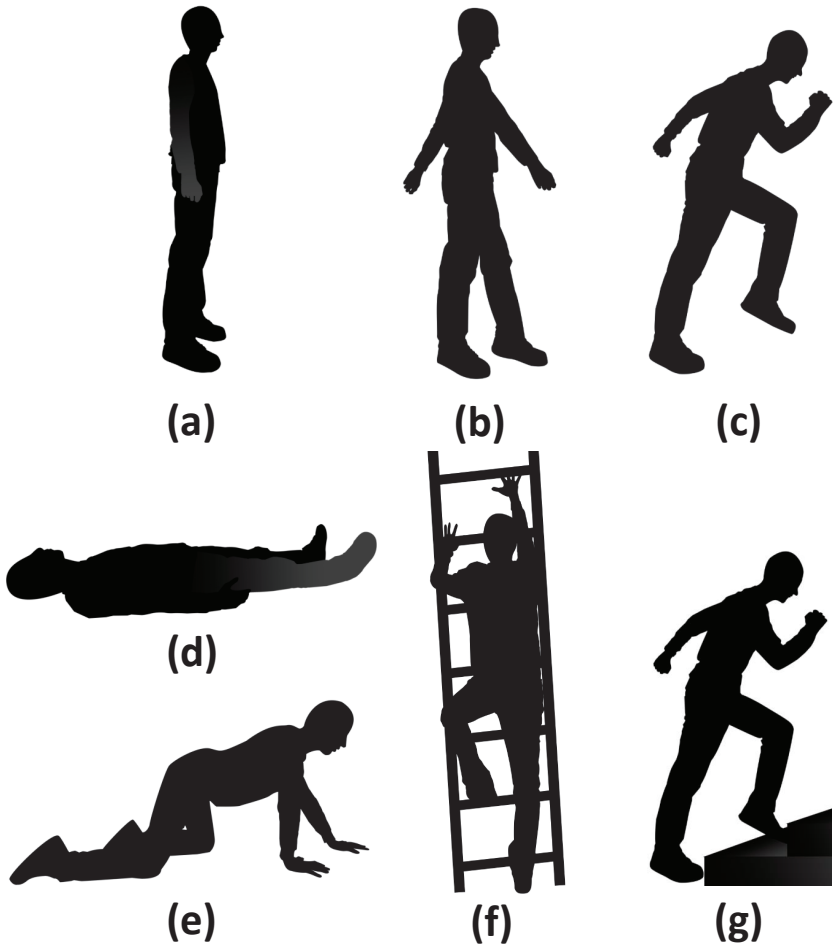

Figure 4.1: Sketch of the seven candidate motions included in the *Motion* set. (a): *Standing*. (b): *Walking*. (c): *Running*. (d): *Lying*. (e): *Crawling*. (f): *Climbing*. (g): *On-the-Stair*.

odically and slowly in a small and proper scale.

- **Running:** The subject move his arms and feet quickly and the scale is larger then walking. The arms of subject bent approximately 90 degrees.

- **Lying:** The subject remain lying on the floor with arms and feet relaxed, face up. Subconsciously movement of both limbs and torso can be neglected.

- **Crawling:** The subject get down to the floor with his knees and hands touch-

ing the floor. The human body curled slightly and his arms and feet moves relatively quickly.

- **Climbing:** The subject climbing upward a ladder with his hands and feet touching the beams of the ladder. The human body stretched slightly and his arms and feet moves relatively quickly.

- **OnTheStair:** The subject running upward stairs with his arms and feet moving quickly and periodically. The arms of subject bent approximately 90 degrees.

Seven candidate motions have been depicted in Fig 4.1 and based on the above definition, the motion case set from a scenario based approach can be given by:

$$Motion = \{Standing, Walking, Running, ...$$

$$...Lying, Crawling, Climbing, OnTheStair\}$$

4.2.2 Sensor Location.

For on-body monitoring network designed for firefighters, remote services is necessary and smart phones often serve as the relay nodes that provide remote connection. For our empirical measurement system, transmitter is fixed to the location of left trouser pocket while the receiver is attached to multiple locations that are often used to measure the physiological signals. Receiver locations include middle of chest, middle of forehead, right wrist and right ankle. The sensors mounted to forehead and chest are often used to record cardiac signal such as ECG and EEG; The sensors mounted to wrist and ankle can be used to measure the pulse and blood

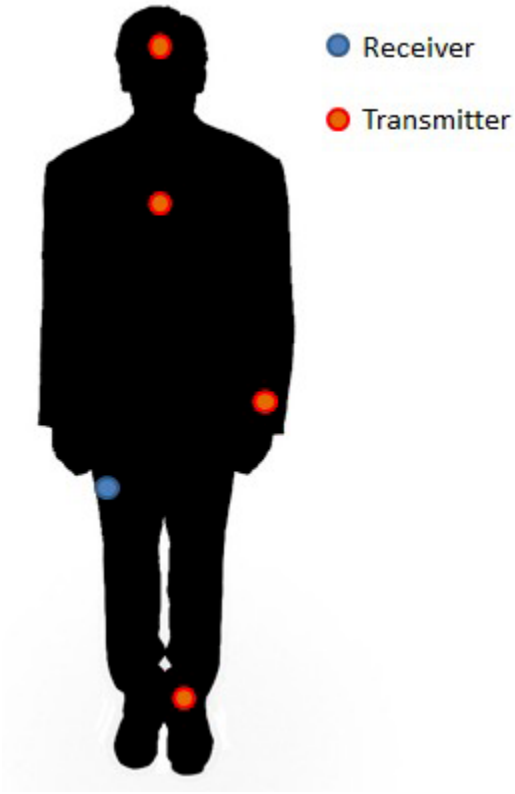

Figure 4.2: Sensor positions on human body. Blue dot represents the smart phone in pocket and red dots represent wearable sensors.

pressure. The sensor location case set can be defined as:

$$Location = \{Chest, Forehead, RightWrist, RightAnkle\}$$

On body position of both sensors and smart phone have been illustrated in Fig 4.2.

4.2.3 Data Recording.

The empirical measurement for wireless channel from body surface to body surface has been performed in an anechoic chamber with the size of $2.32m \times 2.41m \times 2.29m$. The chamber shields the reflections and avoid outside signals. The measurement

system employed in this work consists of a vector network analyzer (VNA, Agilent E8363), a pair of low loss cable, and a pair of small size ISM quarter wavelength antenna. Medium size male has been selected as the subject of the measurement. The receiver antenna (serves as the smart phone or relay node) has been attached to the left trouser pocket at the height of $0.89m$ and it is connected to the RX port of VNA; The transmitter antenna (serves as the on-body sensor node) has been connected to the TX port of VNA and it has been located at different on-body locations throughout the measurement. The VNA continuously sent out single tone waveform at the frequency of 2.45 GHz. Since the antenna-body interaction is an integral part of the overall propagation characteristic, the influence of antenna has been included as part of the channel.

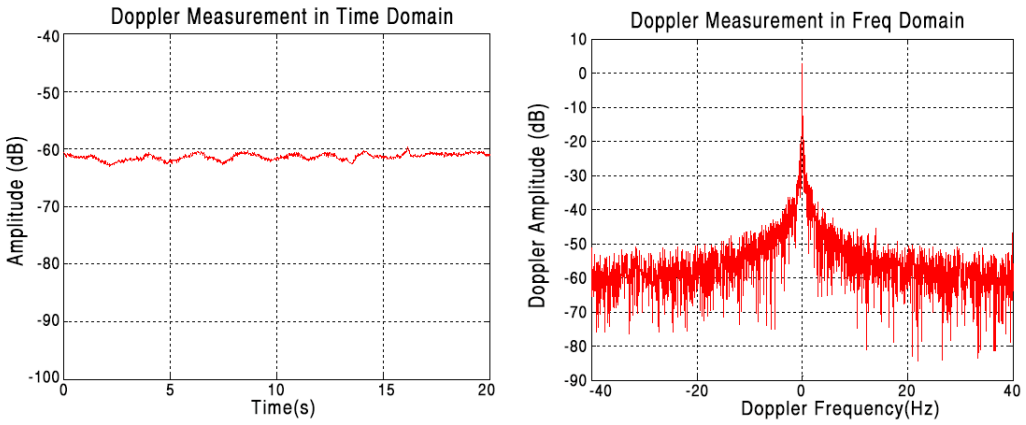

Figure 4.3: Time domain channel profile and frequency domain doppler spread for different human motions when receiver antenna is attached to *Chest*. (a): *Standing*.

4.3 RF Feature Extraction.

Numerous RF characteristics in both time and frequency domain can be potentially extracted from our empirical measurement data to form a concrete feature set for

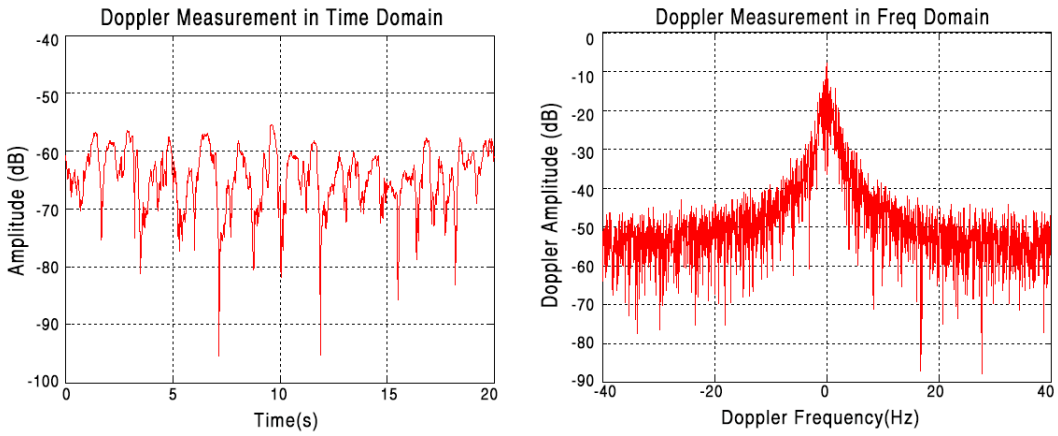

Figure 4.4: Time domain channel profile and frequency domain doppler spread for different human motions when receiver antenna is attached to *Chest*. (b): *Walking*.

future classification. The most prioritized instantaneous RF signal is the Received Signal Strength RSS(t). The Received Signal Strength provides the distance between TX and RX at a specific time according to radio propagation channel models. After that, RSS expectation μ_{RSS} has been included to describe the average TX-RX distance. RSS variance σ^2_{RSS} reflect the scale of human motion, usually a dramatic motion results in large σ^2_{RSS}. RSS skewness γ_{RSS} can be also selected due to the fact that human motions are not always symmetric and skewness describes the asymmetry of distribution. The received single tone $r(t)$ brings the phase of RF signal into the picture and peak to peak value $A_{\text{peak-to-peak}}$ indicates the maximum TX-RX distance for specific human motion. Moreover, Doppler Power Spectrum $D(\lambda)$ and root-mean-square Doppler spread $B_{\text{D,rms}}$ can be independent measurements of intensity of the human motions. In addition, we also considered temporal RF signals such as level crossing rate $N(\rho)$ and fading duration $\tau(\rho)$ in order to model the frequency of repetitive human motions. All these analyzed RF features may serve as the feature set of the following motion classification. In this section, we provide the feature extraction method as well as their detailed mathematical definition.

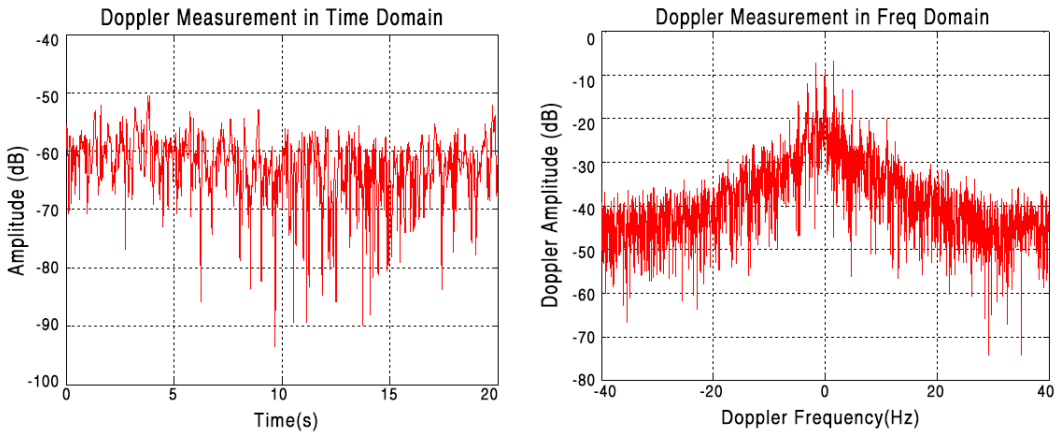

Figure 4.5: Time domain channel profile and frequency domain doppler spread for different human motions when receiver antenna is attached to *Chest*. (c): *Running*.

Based on the previously mentioned measurement system, the single tone cosine signal is continuously broadcasted from the TX antenna and the received signal is sampled 20 times per seconds at distinct time intervals $t = 1, 2, ...$ at the RX side. For each distinct sample, the time domain channel profile $h(f_c; t)$ is recorded as a measurement snapshot, which contains 201 sample points[2] evenly distributed on each sampling interval. For the channel profile, t and f_c denote to the sampling interval and center frequency respectively.

To obtain the statistical information of our RF feature set, 4200 snapshots have been recorded for each one of the four candidate sensor location, in which 600 snapshots are recorded for each specific candidate motion. In this way, an overall sample space of 16800 snapshots forms the dataset for both training and testing.

We consider all above mentioned RF features as the possible support vectors for motion classification and a fixed length sliding window L with the window size of $|L|$ has been established for averaging purpose. For individual snapshot, the Received

[2]Considering fixed VNA performance, there is a trade-off between sampling frequency and number of sample points. Less points achieve higher sampling rate while result in lower resolution. In this work, we select 201 points as the best option.

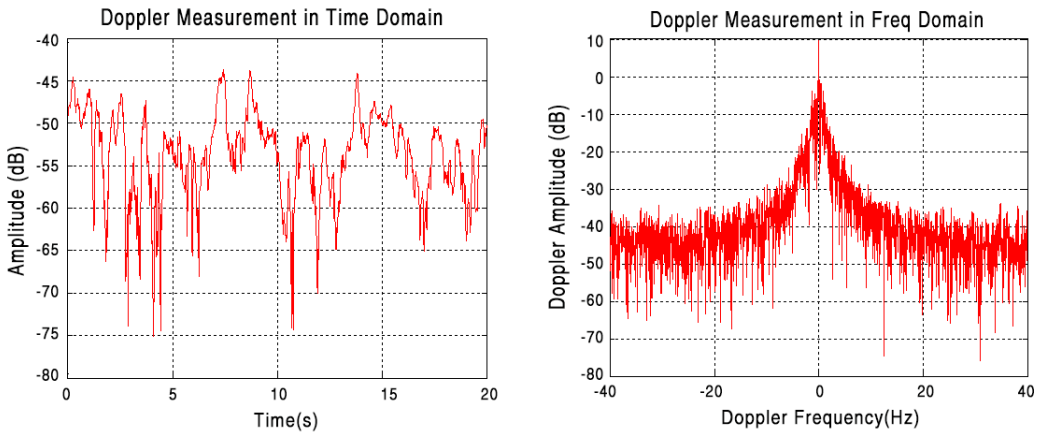

Figure 4.6: Time domain channel profile and frequency domain doppler spread for different human motions when receiver antenna is attached to *Chest*. (d): *Climbing*.

Signal Strength of the single tone is an essential feature that can be directly obtained from $h(f_c; t)$ as follows:

$$\mathrm{RSS}(t) = -20 \log_{10}(\frac{1}{N_s} \sum_{n=1}^{N_s} h(f_c; t)) \tag{4.1}$$

where $\mathrm{RSS}(t)$ is the average pathloss for specific snapshot, N_s is the number of sample points in each snapshot which is 201, and $h(f_c; t)$ is the time domain S_{21} reading at each sample point from the VNA. Typical time domain measurement can be seen in Fig 4.3, Fig 4.4, Fig 4.5 and Fig 4.6.

The expectation value of RSS over a sampling window is also employed as a reference to compare with the real-time RSS reading, which is given by:

$$\mu_{\mathrm{RSS}} = \frac{\sum_{t=1}^{|L|} \mathrm{RSS}(t)}{|L|} \tag{4.2}$$

Higher order statics of the empirical measurement results are also considered as possible support vector. We calculated the second central moment of RSS data as

the variance σ^2_{RSS} and the third central moment as the skewness γ_{RSS}.

$$\sigma^2_{\text{RSS}} = \frac{\sum_{t=1}^{|L|}(\text{RSS}(t) - \mu_{\text{RSS}})^2}{|L|}$$

$$= E(\text{RSS}(t) - \mu_{\text{RSS}})^2 \tag{4.3}$$

The variance σ^2_{RSS} shows the scale of RSS deviation from the μ_{RSS} and the skewness γ_{RSS} is used to determine if the RSS distribution leans to a specific side of μ_{RSS}.

$$\gamma_{\text{RSS}} = E(\text{RSS}(t) - \mu_{\text{RSS}})^3 \tag{4.4}$$

In the above equations, $E[\bullet]$ represents the expectation value of given distribution. In addition to the statistics of RSS, we could also model the received single tone as:

$$r(t) = Re[\sqrt{\text{RSS}(t)}e^{j2\pi f_c t}e^{j\phi_r}] \tag{4.5}$$

where the ϕ_r denotes to the phase of arrived single tone, which is related to the propagation path and is directly available from VNA.

Utilizing the amplitude of received single tone, the difference between maximum and minimum amplitude of received signal within individual sampling window can be therefore given as:

$$A_{\text{peak-to-peak}} = \max_{t \in L}(r(t)) - \min_{t \in L}(r(t)) \tag{4.6}$$

such difference is also known as the peak-to-peak amplitude. The observation of empirical measurement results shows that the RSS at the on-body receiver varies from $-44.43dB$ to $-92.11dB$, indicating that the above mentioned, amplitude related features can be effective identifier for specific motions.

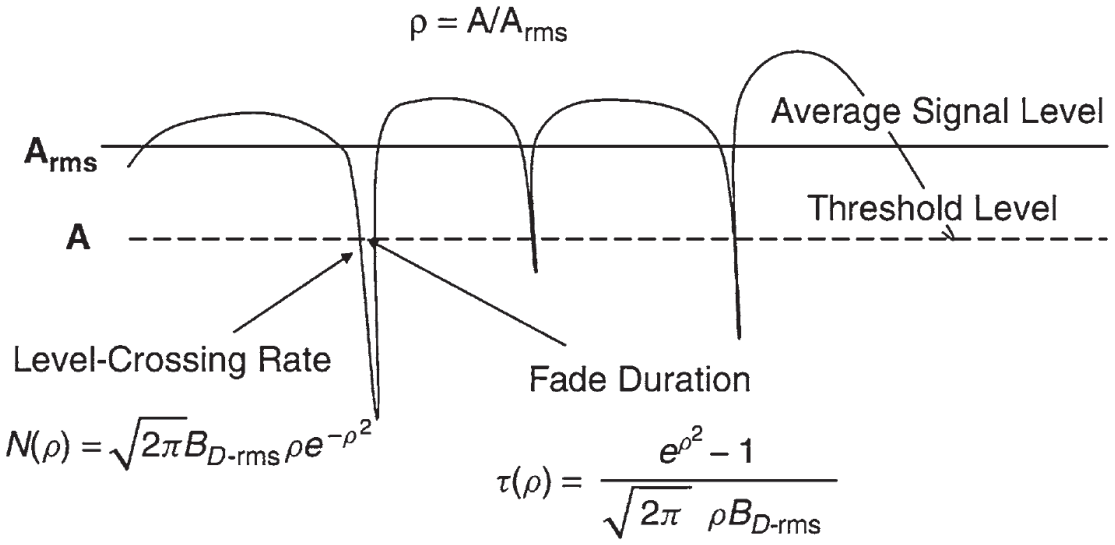

Figure 4.7: Definition of level crossing rate $N(\rho)$ and fading duration $\tau(\rho)$ with normalized threshold depicted in the figure.

Apart from those time domain features, the frequency domain characteristics of RF signal also benefits the accuracy of motion classification. Since the doppler power spectrum represents the temporal variation of the on-body channel and it is caused by the relative movement of transmitter and receiver, we assume that the channel we operates in can be represented by wide sense stationary (WSS) process at a minimum. The doppler power spectrum $D(\lambda)$ can be obtained by applying a Fast Fourier Transform (FFT) to the recorded time domain channel response $h(f_c; t)$ as:

$$D(\lambda) = \sum_{n=1}^{N_s} h(f_c; t) e^{-j\frac{2\pi}{N}\lambda t} \tag{4.7}$$

As we know that the doppler power spectrum is a symmetric function with zero mean and is always bounded by the maximum doppler shift, that A threshold of $-25dB$ has been also applied to $D(\lambda)$ to get the final reading. It comes to the conclusion that the doppler spread varies from $0.1539Hz$ to $18.0884Hz$ in respect of the motion of the human body as well as location of receiver antenna. By horizontal compar-

ison among human motion, for *Standing* and *Lying* cases, the minimum doppler spread can be observed as low as $0.1539Hz$ while for *Running* and *OnTheStair* cases, the maximum doppler spread goes up to $18.0884Hz$. By vertical comparison among different receiver antenna location for same human motion, we observe that when receiver antenna is located at the *Chest*, the doppler spread remains below $14.1345Hz$ for all human motion, indicating that the doppler spread is closely related to the movement intensity of the place we attach the receiver antenna.

In addition to the doppler power spectrum, root-mean-square (rms) doppler spread is also calculated as another feature indicating the pattern of relative movement between transceivers. The rms doppler spread is also known as the second central moment of doppler power spectrum, it is given as:

$$B_{\mathrm{D,rms}} = \sqrt{\frac{\sum_{-f_M}^{f_M} \lambda^2 D(\lambda)}{\sum_{-f_M}^{f_M} D(\lambda)}} \tag{4.8}$$

where $\pm f_M$ denotes to the maximum doppler shift, which can be obtained from calculation of $D(\lambda)$ since $D(\lambda)$ is always bounded by $\pm f_M$.

The fading rate and fading duration of the on-body channel have been also explored to help the later on motion classification. Level crossing rate is an indicator of fading rate and is defined as the average number of downward crossings of a certain threshold per second. The level crossing rate $N(\rho)$ is calculated by:

$$N(\rho) = \sqrt{2\pi}\rho B_{\mathrm{D,rms}} e^{-\rho^2} \tag{4.9}$$

where $\rho = A/A_{\mathrm{rms}}$ is the normalized threshold for counting the crossings; A and A_{rms} denotes to the amplitude and rms-Amplitude of $r(t)$ respectively. Another parameter representing the duration of fade is the fading duration $\tau(\rho)$ which is

given as:

$$\tau(\rho) = \frac{e^{\rho^2} - 1}{\sqrt{2\pi}\rho B_{\mathrm{D,rms}}} \tag{4.10}$$

Definitions of $N(\rho)$ and $\tau(\rho)$ are also shown in Fig 4.7.

4.4 Classification.

A correlation check on all the listed RF features has been applied, followed by a SVM to classify the seven candidate human motions. Since typical SVM is a binary classifier developed for non-linear boundary problem [CV95][BP12], an All-data-at-once approach has been implemented to perform as the core for multi-motion classification.

4.4.1 Correlation Check.

For all possible pair wise combinations of available features, we implement correlation check to limit the redundancy in classification process. Correlation coefficient has been utilized as the evaluation metric and formulation of correlation coefficient is given as

$$r_{x_p,x_q} = \frac{\sum_{i=1}^{l}((x_p)_i - \bar{x_p})((x_q)_i - \bar{x_q})}{(l-1)s_{x_p}s_{x_q}}$$

$$p, q \in \{1, 10\} \text{ and } p \neq q \tag{4.11}$$

where x_p and x_q represents element in different RF feature vectors, notation $\bar{\bullet}$ denotes to the average of feature vector and s_{x_p}, s_{x_q} denotes to the standard deviation of the feature vector.

The calculated pair wise correlation coefficient has been depicted in Table 4.1 where only half of the matrix has been presented due to the symmetric nature. The blue and red area label the intra-correlation of time domain feature pairs and fre-

Table 4.1: Pair wise correlation check for all available RF features. Coefficients greater than 0.4 are labeled in bold font.

	RSS	μ	σ^2	γ	$r(t)$	$\mathrm{A_{pp}}$	$D(\lambda)$	B_{D}	$N(\rho)$	$\tau(\rho)$
RSS	1	**.758**	.305	.279	**.469**	**.414**	.185	.204	.179	.098
μ		1	.313	.325	**.584**	.395	.212	.276	.291	.244
σ^2			1	.191	.303	**.617**	.388	.358	.287	.302
γ				1	.221	.352	.216	.297	.282	.293
$r(t)$					1	.384	.231	.149	.225	.247
$\mathrm{A_{pp}}$						1	.392	.311	**.409**	.373
$D(\lambda)$							1	**.472**	.388	**.406**
B_{D}								1	**.414**	.377
$N(\rho)$									1	**.816**
$\tau(\rho)$										1

quency domain feature pairs respectively. The blank area labels the inter-correlation between time feature and frequency domain feature. We consider a correlation coefficient over 0.4 as the indicator of inadequate efficiency and label these feature pairs in bold font. Several valuable observations raise from the correlation check: 1) For frequency domain features, the level crossing rate $N(\rho)$ and fading duration $\tau(\rho)$ are highly correlated. That observation is expected since by definition, $N(\rho)$ and $\tau(\rho)$ tend to be inversely related to each other; 2) For time domain features, peak-to-peak amplitude $A_{\text{peak-to-peak}}$ and RSS variance σ_{RSS} suffers relatively strong correlation, which can be implied from the fact that RSS variation is proportional to the peak-to-peak amplitude according to respective channel variation caused by

different human motions; 3) The inter domain correlation is very low, which to some scale support the mechanism for feature extraction in previous sections. Such correlation check provides potential space for further optimized feature selection, which is discussed later in chapter VI.

4.4.2 All-Data-At-Once Classifier.

For detection and classification of described human motions with our on-body monitoring network, all-data-at-once classification approach has been employed in this work to achieve multiple candidates classification. The classifier constructs k binary-classification rules where the m^{th} function $\omega_m^T \phi(x) + b_m$ seperates training vectors of class m from all the other available training vectors. Though we created k decision functions, they are all obtained by solving same problem [HL02a].

From the previous future extraction and data recording process, we collected l training data $(x_1, y_1), ..., (x_l, y_l)$, where $x_i \in R^n, i = 1, ..., l$ are training vectors containing empirical features with different candidate motions and $y_i \in \{1, ..., k\}$ represents the labeled class of x_i. In this specific case, we have l as training data size, $n = 10$ as the total number of features and $k = 7$ as all available motions.

Since the ultimate goal of the classifier is to work out the hyperplane that to the greatest scale separates target motion from other candidate motions, the satisfactory hyperplane can be represented by $\omega^T x + b = 0$ where ω is the weighted coefficient vector that is normal to the hyperplane and b is the bias term [Chr98]. As a result, the formulations for this SVM can be given as [HL02a]:

$$\min_{\omega, b, \xi} \qquad \frac{1}{2} \sum_{m=1}^{k} \omega_m^T \omega_m + C \sum_{i=1}^{l} \sum_{m \neq y_i} \xi_i^m$$

$$\text{subject to} \quad \omega_{y_i}^T \phi(x_i) + b_{y_i} \geq \omega_m^T \phi(x_i) + b_m + 2 - \xi_i^m$$

$$\xi_i^m \geq 0, i = 1, ..., l, m \in \{1, ..., k\} \backslash y_i \tag{4.12}$$

where the function $\phi(\bullet)$ is defined as $\phi(\bullet) : R^n \longmapsto \Psi^z, n < z$ to map x_i into higher dimensional Euclidean space when the problem is not linearly solvable and $C \sum_{i=1}^{l} \sum_{m \neq y_i} \xi_i^m$ is a panelty term which can reduce the number of training errors. Minimizing $\frac{1}{2}\omega_m^T \omega_m$ means we would like to maximize the margin between two groups of data based on a balance between regularization term $\frac{1}{2}\omega_m^T \omega_m$ and training errors. The decision function of above mentioned quadratic programming problem is

$$\arg\max_{m=1,...,k} \ (\omega_m^T \phi(x) + b_m) \tag{4.13}$$

which represents x is in the class that has the largest value of available decision functions.

Similar to binary SVM, in practical applications we solve the dual problem of (12) whose number of variables is the same as number of data in (12). The dual formulation of (12) can be obtained by Lagrangian method as [HL02a][HL02b]

$$\min_{\alpha} \qquad \sum_{i,j} (\frac{1}{2} c_j^{y_i} A_i A_j - \sum_m \alpha_i^m \alpha_j^{y_i} + \frac{1}{2} \sum_m \alpha_i^m \alpha_j^m) K_{i,j}$$

$$-2 \sum_{i,m} \alpha_i^m \sum_{i=1}^{l} \alpha_i^m = \sum_{i=1}^{l} c_i^m A_i, \ \ i = 1, ..., l, \ \ m = 1, ..., k$$

$$0 \leq \alpha_i^m \leq C, \ \alpha_i^{y_i} = 0, \ A_i = \sum_{m=1}^{k} \alpha_i^m, \ c_i^{y_i} = \begin{cases} 1, & y_i = y_j \\ 0, & y_i \neq y_j \end{cases} \tag{4.14}$$

where $\alpha_i^{y_i}$ is a dummy variable of Lagrangian, $c_i^{y_i}$ is the class indicator; c_i^m, A_i and α_i^m are actual variables of Lagrangian, and $K_{i,j} = \phi(x_i)^T \phi(x_j)$ is the Kernel function to return the inner product for higher dimensional matrix. Derivation of

equation (14) can be found at [HL02a][HL02b], details of all-data-at-once SVM will not be further expanded in this section. Since $\omega_m = (c_i^m A_i - \alpha_i^m)\phi(x_i),\ \ m = 1, ..., k$, we introduce the Gaussian Kernal $K(x_i, x) = exp(-\frac{||x_i - x||}{\sigma^2})$ into ω_m and the final decision function is

$$\arg\max_{m=1,...,k} \ (\sum_{i=1}^{l}(c_i^m A_i - \alpha_i^m)K(x_i, x) + b_m) \tag{4.15}$$

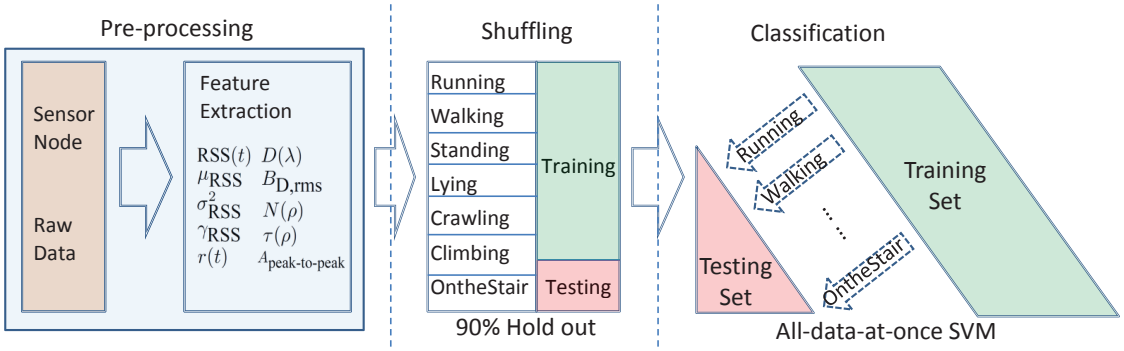

Figure 4.8: Data flow of the entire motion classification scheme. Raw data is collected by on-body sensors and RF features are extracted in pre-processing phase. Then feature samples are randomly shuffled and partitioned into training and testing set. Finally SVM is trained and tested.

The overall data flow of the proposed approach has been shown in Fig 4.8. Note that the following description focus on fixed sensor location and the entire classification process are iterated four times to traverse the *location* set. As mentioned in previous sections, raw data is collected by our measurement system and 10 available features are extracted in the pre-processing phase. As for training set preparation, we employed 3 human subjects performing every candidate motions in the *motion* set repeatedly. Each particular motion lasts for 10s and the total number of samples obtained for each motion is 20(sample/s) $\times$ 10(seconds) $\times$ 3(subjects) = 600. Considering a window length of $L = 32$, the actual number of valid samples is slightly

smaller. Note that small L may result in a distortion of RF signal statistics and large L may lead to inaccuracy of temporal RF signal measurement. A range between 20 and 40 is recommended and the classification performance in such range is almost identical. Empirical results for 7 motions are forwarded into shuffling phase after pre-processing. In that phase, the entire data set of 600(samples) $\times$ 7(motions) = 4200 samples are randomly shuffled to avoid any possible sequential effects. The shuffling process is necessary due to the fact that the involvement of randomness helps to mitigate the effect of human error such as variety of subject body sizes, habitually difference of subject postures and etc. 20% samples in the data set are reserved as testing set for future performance validation and the remaining 80% samples are used for training the SVM.

$LibSVM$, the open source SVM library implemented by Chang and Lin [CL11] has been utilized in this research. Given proper Kernel function and penalty term, $LibSVM$ helps construct decision boundary between each candidate motion. The optimal values of penalty term and Kernel width of SVM are manually determined by employing a tenfold cross-validation over the training set and calculating the average classification error. It results in an average classification error of 0.029 (97.1% accuracy) and variance of 0.011 with the optimized values. Such SVM tuning result is superior to similar implementations in [SSS$^+$14][KL09] and is satisfactory. The above mentioned data flow leads to the classification performance with specific sensor location. In the remaining 3 iterations, we follow the exactly same process and change the Rx location.

4.5 Performance Evaluation.

4.5.1 Evaluation Metrics.

To determine the performance of the SVM discussed in the previous section, we calculate the percentage of true classification and false classification. The output of individual classification case can be either target motion or other motion. The true classification rate is computed as the ratio of correctly classified target motion samples to the total number of target motion samples. The false classification rate denotes to the ratio of mistakenly classified other motion samples to the total number of other motion samples. Based on the confusion matrix shown in Table 4.2, the two metrics can be defined as:

$$\text{True classification rate} = \frac{TP}{TP + FP} \tag{4.16}$$

$$\text{False classification rate} = \frac{FN}{FN + TN} \tag{4.17}$$

Table 4.2: Confusion matrix employed in this study.

		Actual motion	
		Target motion	Other motion
Classified motion	Target motion	True Positive (TP)	False Positive (FP)
	Other motion	True Negative (TN)	False Negative (FN)

The ideal performance of multi-candidates classifier is to have a high true classification rate and a low false classification rate. The true classification rate in the real world application represents the probability to detect abnormal motion which is vital for the safety of firefighters. Inadequate true classification rate is absolutely not tolerable. The false classification rate represents the probability of false alarm-

ing which may cost extra attention on the monitoring of firefighters. Therefore, in the following subsection, we evaluate the performance of SVM classifier using both raw classification rate and Receiver Operating Characteristic (ROC) curve, which plot the true classification rate against the false classification rate.

4.5.2 Result Analysis.

Investigation of the performance of the SVM classifier has been applied from three different perspective including typical classification results, effects of human motions and effects of sensor locations. As a plus, we also considered subset of the entire feature set to seek for more efficient combination of support vectors. Such investigation results in less computational cost and faster speed when implementing the posted scheme on real-world on-body health monitoring system.

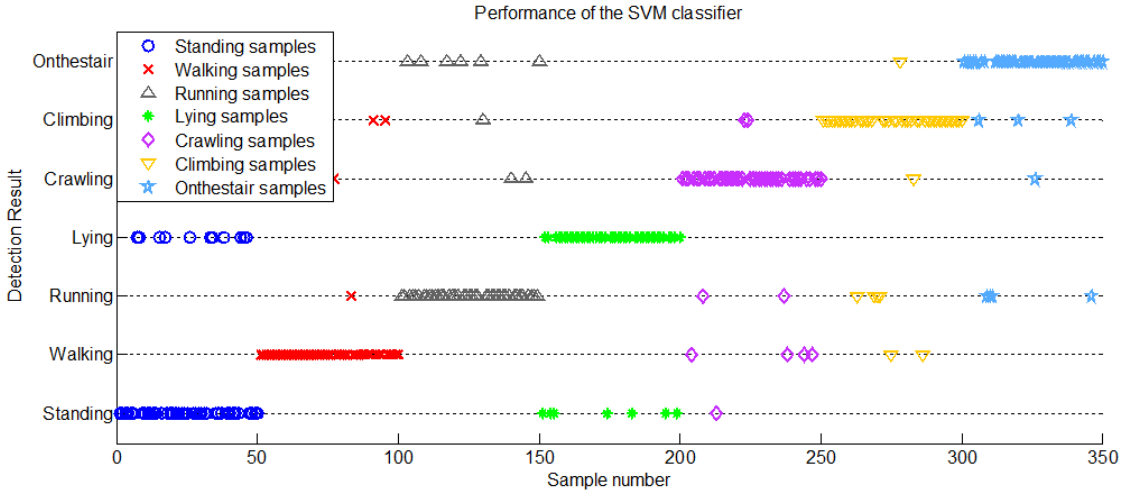

Figure 4.9: Sample results of SVM classifier performance evaluation. Only the beginning 50 classification results for each human motion are plotted for clarity of illustration.

Typical testing results for wrist mounted sensor cases has been plotted in Fig 4.9, first 50 testing results for specific motion are displayed to guarantee the clarity.

All seven human motions included in *Motion* set have been labeled with different symbols. Several observations can be obtained from Fig 4.9 as following: 1): All mis-classifications of standing cases end up to be classified as lying. Similarly, all of the mis-classifications of lying cases are classified as Standing. We conclude that this phenomenon is caused by the similar RF characteristics of these two motions. Further investigation on that phenomenon is necessary because in the real world application, standing can be regarded as normal activity but lying is significantly abnormal for firefighters or patients. It is essential to clearly distinct these two motions. 2): The best performance occurs on the walking case for which only four classification failures appear. That is most likely because the doppler spread for walking case is relatively isolated from other motions. 3): Crawling and climbing can be mis-classified as multiple other motions, however, they are hardly ever detected as standing or lying. Moreover, classification of crawling and climbing does not interference with each other very often. Such result is caused by the distance between transmitter and receiver. In crawling cases, the transmitter-receiver distance is smaller than that of climbing cases, resulting in more drastic change of received signal strength. 4): The running cases are relatively easier to be mis-classified as on-the-stair because of the similar doppler spread, however, the on-the-stair cases are mis-classified into multiple different motions.

Apart from the previously mentioned observations, it is also important to numerically and visually analyze the SVM classifier performance for specific human motions. Table 4.3 details the classification accuracy of our proposed scheme. From the highest overall true classification rate, the seven candidate motions can be sorted as lying (91.72%), walking (90.71%), standing (90.11%), running (89.56%), climbing (88.16%), on the stair (86.91%) and crawling (83.89%). There is trivial part of standing samples classified as walking and part of lying samples classified as walking

Table 4.3: Classification of candidate human motions conducted at all available sensor locations.

Actual Motion	Receiver Location	Predicted Human Motion							Overall (%)
		Standing (%)	Walking (%)	Runing (%)	Lying (%)	Crawing (%)	Climbing (%)	OnTheStair (%)	
Standing	Chest	**90.96**			9.04				**90.11**
	Forehead	**89.68**	0.03		10.29				
	Wrist	**89.47**	0.12		10.41				
	Ankle	**90.33**			9.67				
Walking	Chest	0.53	**92.54**	3.15		1.67		2.11	**91.49**
	Forehead	0.64	**90.09**	4.24		1.59	0.37	3.07	
	Wrist	0.25	**91.79**	0.97	0.12	4.17	0.25	2.45	
	Ankle	0.37	**91.53**	1.79	0.09	3.93	0.56	1.73	
Running	Chest	0.64	2.21	**89.47**	0.12	1.17	0.77	5.62	**89.56**
	Forehead		3.38	**88.18**		2.03	0.40	6.01	
	Wrist	0.06	0.83	**90.96**	0.06	0.98		7.11	
	Ankle	0.09	0.34	**89.63**		1.55	0.65	7.74	
Lying	Chest	9.23			**90.77**				**90.71**
	Forehead	8.47			**91.28**	0.25			
	Wrist	8.21	0.37		**90.36**	1.06			
	Ankle	8.97	0.25		**90.42**	0.37			
Crawling	Chest	1.09	3.21	3.55	0.42	**81.45**	5.62	4.66	**83.89**
	Forehead	0.97	3.31	2.83		**82.78**	5.98	4.13	
	Wrist	1.11	2.97	2.76	0.30	**86.97**	1.87	4.02	
	Ankle	1.17	4.11	3.88		**84.34**	1.92	4.58	
Climbing	Chest	0.93	4.16	0.68	0.37	3.34	**86.75**	3.77	**88.16**
	Forehead	0.77	5.33	0.15	0.03	2.40	**87.89**	3.43	
	Wrist		4.96	0.09		1.26	**89.74**	3.95	
	Ankle	0.09	5.15			2.81	**88.28**	3.67	
OnTheStair	Chest	0.03	1.25	9.41		3.38	1.28	**84.65**	**86.91**
	Forehead	0.09	0.97	9.87		2.98	0.37	**85.72**	
	Wrist		1.13	8.25	0.12	1.89	0.15	**88.46**	
	Ankle		1.67	6.77	0.22	2.51		**88.83**	

and crawling due to the subconsciously movement of subjects. However, since the number of such samples is small enough, we conclude that the previously mentioned four observations still hold for general trend.

The effect of different human motions and sensor locations has been analyzed separately by ROC curve as following. We select all seven motions for wrist mounted sensor as typical case to investigate the effect of different motions. The ROC curve for seven human motions in *Motion* set has been presented in Fig 4.10, and the closest point to the upper left corner has been marked. A gap in Fig 4.10 can be found that partitioned the seven motions into two groups. Since the SVM classifier has a better performance when the ROC curve is closer to upper left corner [SC13], we conclude from visual inspection that the group with better performance includes standing, lying and walking, while the group with worse performance includes running, crawling, climbing and on the stair. Exploiting the grouping results, we hereby

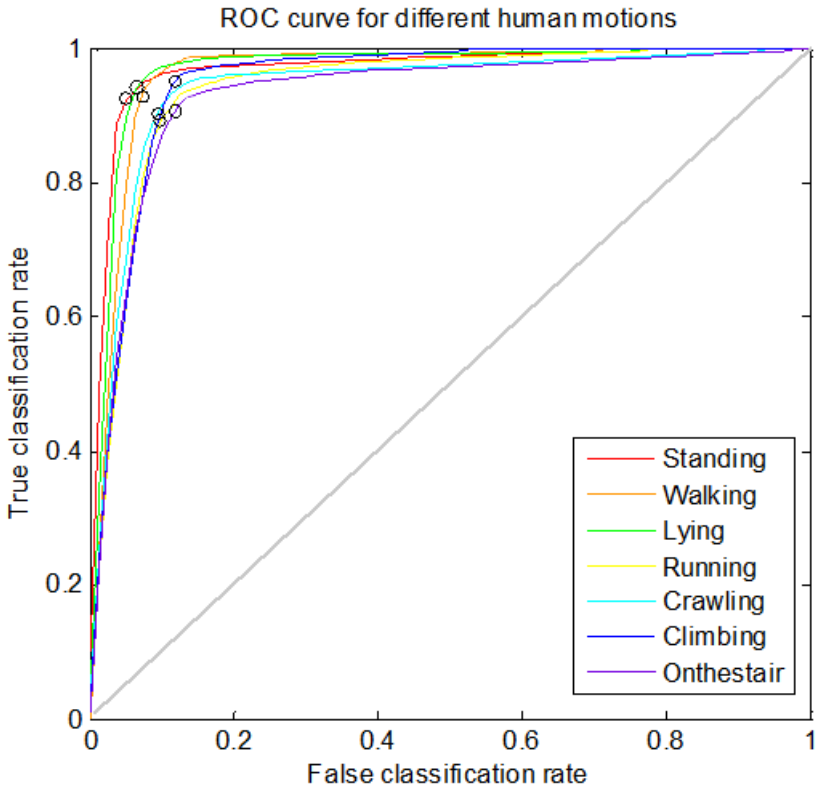

Figure 4.10: ROC curve for all seven target motions, $Location = \{Wrist\}$.

define standing, lying, and walking (group I) as static motions for their gentle and small scale relative movement between on-body transceivers, while define running, crawling, climbing and on the stair (group II) as dynamic motions for their faster and large scale relative movement. We believe that the static motions are easier to predict because of the stability and large weight of higher order statistic features such as σ^2_{RSS} and γ_{RSS}.

The effect of receiver sensor location has been depicted in Fig 4.11 which illustrates the performance of running motion for all four sensor locations in *Location* set. The ROC curve shows that for running motion, wrist mounted sensor has the highest true classification rate, followed by ankle mounted sensor and chest mounted sensor. The forehead mounted sensor shows the worst classification ac-

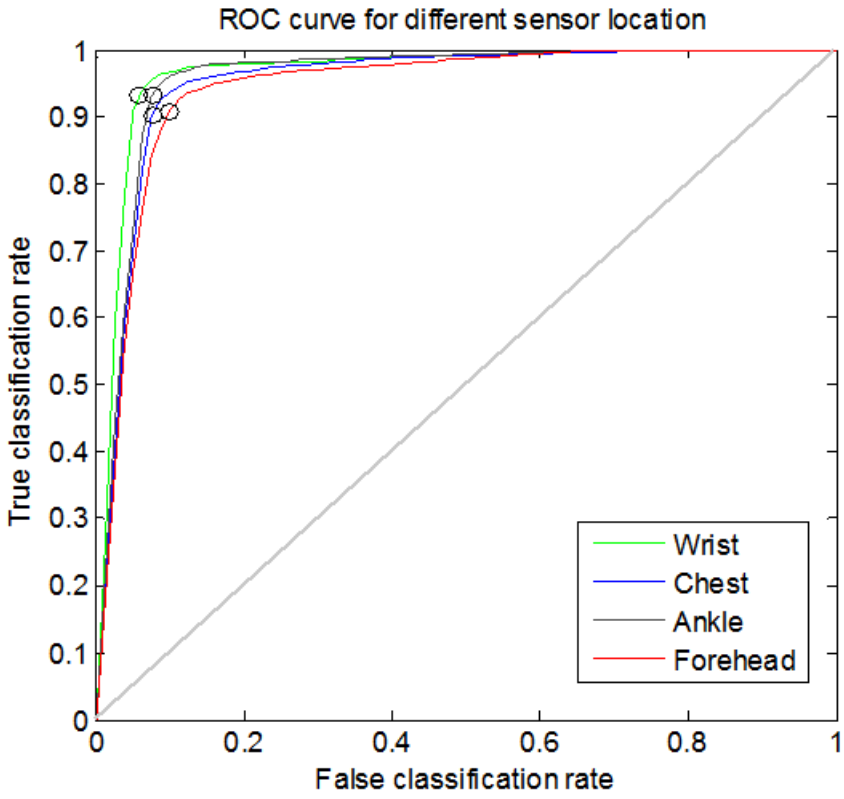

Figure 4.11: ROC curve for all seven target motions, $Motion = \{running\}$.

curacy. Similar results can be also observed in crawling, climbing and on-the-stair cases, indicating that for those dynamic motions, the effect of sensor location should not be ignored. According to the true classification rate, sensor locations with more significant movement such as wrist and ankle benefit the accurate classification of relatively fierce motion. In the contrast, the subconsciously movement of wrist and ankle may influence the true classification rate for static motions such as lying and standing. Since the chest and forehead mounted sensor benefits the measurement of physiological signal for on-body health monitoring sensors, such observation should be taken into consideration as the trade-off between health monitoring and motion classification.

As the further investigation for applicability of our proposed scheme, we evalu-

Table 4.4: Classification of candidate human motions with RF features take-away one at a time, for wrist mounted sensor only.

Selected feature	Available combination of RF features										Classification rate for specific motion(%)						
	RSS	μ	σ^2	γ	$r(t)$	A_{pp}	$D(\lambda)$	B_D	$N(\rho)$	$\tau(\rho)$	Standing	Walking	Runing	Lying	Crawing	Climbing	OnTheStair
3		×	×				×				54.07	26.48	18.86	49.98	15.23	13.34	16.55
4		×	×	×			×				57.52	40.97	19.72	51.45	12.39	14.78	23.82
5		×	×	×			×			×	64.95	50.82	31.26	59.84	25.18	33.56	29.85
6		×	×	×			×	×		×	76.46	61.33	54.48	74.09	48.04	51.41	50.09
7		×	×	×	×		×	×		×	80.09	76.96	70.37	82.25	67.17	69.09	71.84
8		×	×	×	×	×	×	×		×	85.25	86.33	84.22	87.67	83.09	84.48	82.85
9	×	×	×	×	×	×	×	×		×	88.98	88.74	86.04	89.46	86.27	85.56	84.71
10	×	×	×	×	×	×	×	×	×	×	89.47	91.79	90.96	90.36	86.97	89.74	88.46

ate the combined effect of all available features by take-away one feature at a time based on the result of correlation check[3]. The take-away order we employed is given as $N(\rho)$, RSS, A_{pp}, $r(t)$, B_D, $\tau(\rho)$ and γ_{RSS}. Since the classification rate for all candidate motions approaches the baseline, remaining features of the above mentioned take-away process are considered as minimum set for effective classification. We repeat both training and testing process each time we take away a feature, and record the remaining feature combination and respective classification rate in Table 4.4. To isolate the effect of different sensor location, this investigation is also limited with wrist mounted sensor, results of other sensor locations are reserved for later analysis. The classification accuracy change is also plotted in Fig 4.12. As expected, less number of features results in lower classification accuracy in general. However, the first two features, namely, $N(\rho)$ and RSS influence the classification rate very marginally. Therefore, acceptable accuracy can be still achieved with only eight most important features.

Fig 4.12 also shows the distinction between static and dynamic motions. Previously mentioned four dynamic motions still group together and suffer from a severer performance drop with the decrement of available feature number and they end up

[3]Note that since the features can interact in a complex way in the classification process, it is not easy to predict the exact effect of combining features. we focus on the general change of classification rate instead of the detailed mechanism that feature combinations apply their influence.

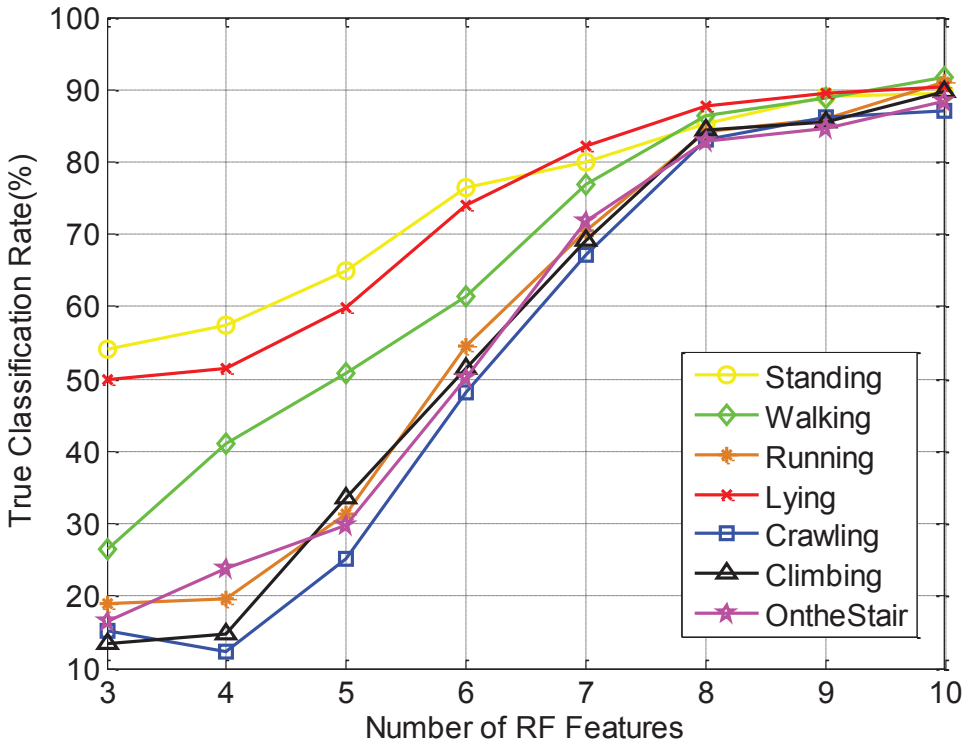

Figure 4.12: Relationship between available RF feature number and SVM true classification rate for seven human motions, $Location = \{Wrist\}$.

at a baseline classification rate around 18%. The classification rate of standing and lying samples drops much slower than dynamic motions and results in a baseline of approximately 52%. Accuracy of walking classification stays in the middle with different drop rate and baseline due to its semi-dynamic nature, that is, even though we define it as static motion, relative movement still exists and has to be considered to some degree. It is questionable whether it's fair to compare static and dynamic motions in that way due to their different baseline[4]. However, the comparison indicates that the influence of candidate motion selection should not be totally ignored, at a minimum.

[4]If we regard walking as dynamic motion and have 2 static motions and 5 dynamic motions in total, baseline of randomly selection from a specific category will be 20% and 50% respectively. That baseline agrees with our observation.

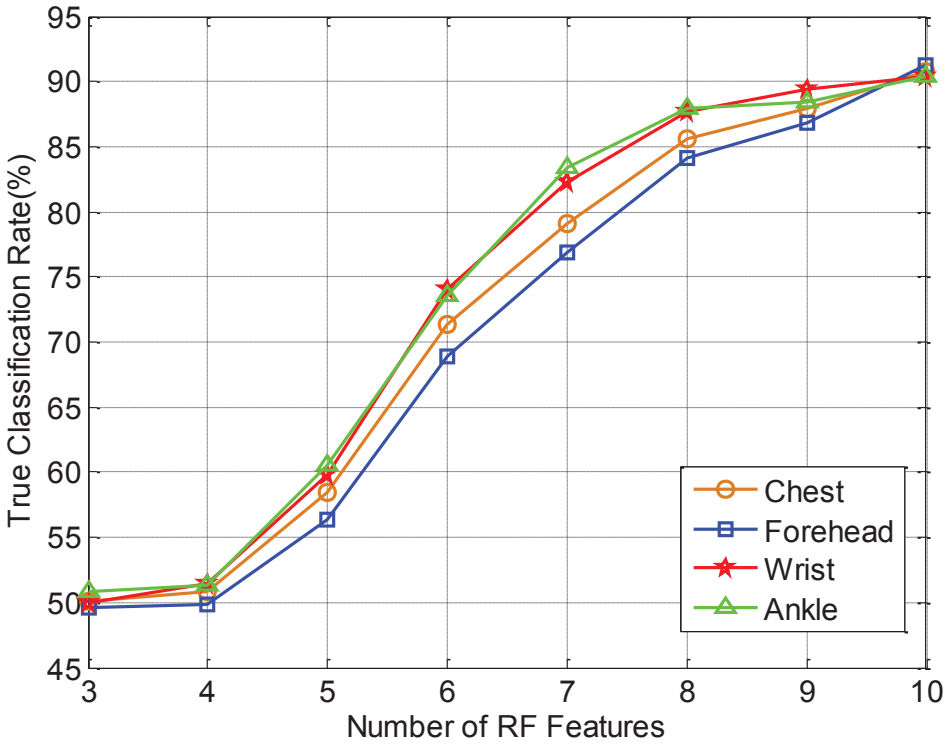

Figure 4.13: Relationship between available RF feature number and SVM true classification rate for four receiver locations, $Motion = \{Lying\}$.

Study of applicability regarding various sensor locations has been also conducted in respect to typical cases of both static and dynamic motions. We take the results from previous feature take-away process and focus on lying and running motions with all available sensor locations. Classification rate of lying and running cases has been presented in Table 4.5 and Table 4.6 respectively and we plot them in Fig 4.13 and Fig 4.14. For lying case, the trend of performance drop for each sensor location is quite similar to others while for running case, classification rate for chest and forehead mounted sensors drops below 60% with seven available RF features. We conclude that for chest and forehead mounted sensors, the frequency domain RF features are less effective since the relative movement between transceivers is smaller by nature, so that when dealing with dynamic motions, wrist and ankle mounted

sensors are recommended.

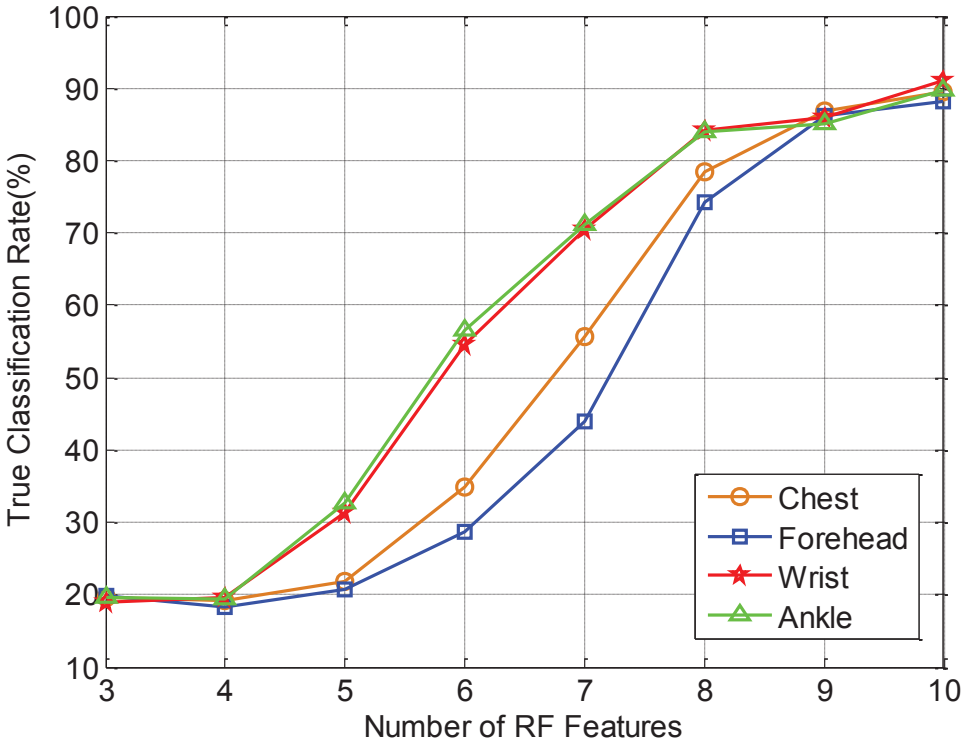

Figure 4.14: Relationship between available RF feature number and SVM true classification rate for four receiver locations, $Motion = \{Running\}$.

To sum up the general analysis on classification performance, key features for different candidate motions have been investigated as well. It is difficult to mathematically work out the importance of different features due to the complexity of SVM, however, experiments have been conducted with single feature excluded method. We exclude RSS(t) from the overall data set, repeat the entire classification process with the new data set, and then perform the same exclusive operation on other features one at a time. With single feature excluded, the performance drop has been computed in terms of average classification rate for all available sensor locations. The feature with maximum performance drop is considered to have the strongest influence. Empirical results are listed in Table 4.7.

Table 4.5: Classification of candidate human motions with RF features take-away one at a time, for lying motion only.

Selected	Available combination of RF features										Classification rate for specific motion(%)			
feature	RSS	μ	σ^2	γ	$r(t)$	A_{pp}	$D(\lambda)$	B_D	$N(\rho)$	$\tau(\rho)$	Chest	Forehead	Wrist	Ankle
3		×	×				×				50.13	49.61	49.98	50.86
4		×	×	×			×				50.78	49.91	51.45	51.23
5		×	×	×			×			×	58.50	56.35	59.84	60.53
6		×	×	×			×	×		×	71.31	68.92	74.09	73.57
7		×	×	×	×		×	×		×	79.10	76.87	82.25	83.40
8		×	×	×	×	×	×	×		×	85.63	84.08	87.67	87.95
9	×	×	×	×	×	×	×	×		×	87.89	86.80	89.46	88.48
10	×	×	×	×	×	×	×	×	×	×	90.77	91.28	90.36	90.42

Table 4.6: Classification of candidate human motions with RF features take-away one at a time, for running motion only.

Selected	Available combination of RF features										Classification rate for specific motion(%)			
feature	RSS	μ	σ^2	γ	$r(t)$	A_{pp}	$D(\lambda)$	B_D	$N(\rho)$	$\tau(\rho)$	Chest	Forehead	Wrist	Ankle
3		×	×				×				19.57	19.82	18.86	19.61
4		×	×	×			×				19.09	18.21	19.72	19.49
5		×	×	×			×			×	21.82	20.73	31.26	32.70
6		×	×	×			×	×		×	34.91	28.66	54.48	56.45
7		×	×	×	×		×	×		×	55.62	43.97	70.37	71.14
8		×	×	×	×	×	×	×		×	78.36	74.28	84.22	83.91
9	×	×	×	×	×	×	×	×		×	86.84	86.07	86.04	85.18
10	×	×	×	×	×	×	×	×	×	×	89.47	88.18	90.96	89.63

Three different key features have been detected for seven candidate motions. For standing, walking and lying, σ^2_{RSS} has been found to be the key feature. Such result indicate that for static motions, the most significant characteristic could be a low variance on RSS due to its steady nature. For intensively dynamic motions such as running and on the stair, $D(\lambda)$ leads to largest performance drop. It is also expected because such intensive motions often results in over 10Hz of doppler power spectrum between TX and RX[FYP12]. The last key feature is the peak-to-peak amplitude for Crawling and Climbing. Note that various features are almost evenly important and peak-to-peak amplitude only takes a slightly lead on performance drop. Such phenomenon may come from the body stretch with crawling and climbing motions. Such three key features also validated the previous intuitions in feature extraction

Table 4.7: Classification of candidate human motions with excluded features.

	Excluded feature									
	RSS	μ	σ^2	γ	$r(t)$	A_{pp}	$D(\lambda)$	B_D	$N(\rho)$	$\tau(\rho)$
Standing	6.21	2.59	**9.75**	0.27	2.26	3.31	0.73	0.35	0.49	0.26
Walking	5.47	3.79	**5.62**	1.94	2.07	4.27	3.66	5.41	3.05	2.19
Running	5.39	1.80	5.07	4.37	3.65	2.29	**12.25**	7.73	4.92	3.77
Lying	5.83	3.73	**9.14**	0.88	1.86	6.06	0.52	0.98	0.09	0.31
Crawling	3.26	1.92	4.71	3.71	3.11	**5.64**	5.24	4.39	0.70	2.50
Climbing	2.19	2.04	6.09	3.16	4.83	**4.85**	4.27	4.76	4.18	2.94
OnTheStair	5.44	4.67	4.48	6.65	3.54	2.77	**14.51**	5.91	3.75	4.43

section.

4.5.3 Effect of Multipath.

The above mentioned results provide a general view on the performance of RF based human motion classification and help understand the characteristics of different RF features. However, in order to apply such method to practical wearable sensor network applications, it is still necessary to take the multipath effect into consideration. To further analyze the effect of multipath, we repeated the entire experiment in two most frequently appeared multipath scenario including empty corridor and typical office room. Note that the room we selected is medium size with dimension of 18x12 square meters and is equipped with desks, chairs, large windows and blackboards.

Table 4.8 illustrates the classification accuracy in multipath scenario. Results from both repetitive experiments have been combined so that for each cell in Table 4.8, the former number shows the classification rate for empty corridor scenario while the later number is the classification rate for office room scenario. In the corridor scenario, the classification rate of seven candidate motions can be sorted as lying (90.73%), walking (90.29%), standing (89.97%), climbing (87.43%), running (87.27%), on the stair (86.05%) and crawling (83.16%). On the other hand, in the typical office room scenario, it can be sorted as lying (90.42%), standing (89.44%),

Table 4.8: Classification of candidate human motions in multipath scenario.

Actual Motion	Receiver Location	Predicted Human Motion: Standing (%)	Walking (%)	Runing (%)	Lying (%)	Crawing (%)	Climbing (%)	OnTheStair (%)	Overall (%)
Standing	Chest	**90.36/89.27**	0.06/0.15	/	9.58/10.56	/	/	/	**89.97/89.44**
	Forehead	**89.85/89.03**	0.06/0.18	/	10.09/10.73	/	/0.06	/	
	Wrist	**89.21/89.15**	0.12/0.15	/	10.76/10.67	/	/0.03	/	
	Ankle	**90.44/90.30**	0.12/0.21	/	9.44/9.49	/	/	/	
Walking	Chest	0.90/0.75	**90.98/89.68**	3.75/4.85	0.06/0.03	1.67/1.78	0.41/0.55	2.23/2.36	**90.29/89.18**
	Forehead	0.67/0.67	**89.44/88.83**	4.43/4.89	0.12/0.09	1.62/1.84	0.37/0.44	3.35/3.24	
	Wrist	0.55/0.67	**90.36/89.09**	1.19/1.78	0.12/0.15	4.58/4.92	0.33/0.41	2.87/2.98	
	Ankle	0.61/0.78	**90.36/89.12**	1.97/1.91	0.09/0.12	4.17/4.43	0.75/0.78	2.05/2.86	
Running	Chest	0.69/0.09	2.43/2.35	**87.14/86.86**	0.12/0.06	1.33/1.43	0.89/0.76	7.40/8.45	**87.27/86.77**
	Forehead	0.12/0.12	3.49/3.79	**86.43/86.01**	0.06/0.03	1.79/1.69	0.68/1.05	7.43/7.31	
	Wrist	0.12/0.09	1.45/1.67	**87.89/87.22**	0.06/0.09	1.48/1.98	0.29/0.48	8.71/8.56	
	Ankle	0.15/0.43	1.14/2.14	**87.61/86.97**	0.03/0.23	1.55/1.67	0.72/0.98	8.79/7.75	
Lying	Chest	9.18/9.64	/	/	**90.82/90.33**	/0.03	/	/	**90.73/90.42**
	Forehead	8.61/9.30	/	/	**91.39/90.67**	/0.03	/	/	
	Wrist	8.69/8.77	0.12/0.15	/	**90.44/90.33**	0.75/0.75	/	/	
	Ankle	9.51/9.19	0.03/0.12	/	**90.28/90.36**	0.18/0.33	/	/	
Crawling	Chest	0.89/0.33	4.03/3.98	1.60/2.21	0.61/0.61	**80.74/80.31**	8.39/8.58	3.74/3.98	**83.16/82.72**
	Forehead	0.81/0.47	4.15/3.82	1.37/2.16	0.30/0.44	**82.08/81.87**	7.21/6.93	4.08/4.31	
	Wrist	0.67/0.37	3.77/3.17	1.21/1.94	0.42/0.15	**85.69/85.21**	4.32/5.01	3.92/4.15	
	Ankle	0.72/0.44	4.58/4.29	1.65/2.08	0.12/0.15	**84.14/83.47**	4.64/5.39	4.15/4.22	
Climbing	Chest	0.37/0.79	5.25/5.32	0.42/0.67	0.09/0.15	6.11/6.06	**85.92/84.87**	1.84/2.14	**87.43/86.87**
	Forehead	0.44/0.28	5.67/6.08	0.12/0.33	0.12/0.06	4.56/5.20	**87.11/86.29**	1.98/1.76	
	Wrist	0.12/0.33	5.78/5.97	0.25/0.25	0.15/0.12	5.60/2.52	**89.05/88.89**	2.05/1.92	
	Ankle	0.25/0.41	5.94/6.11	0.54/0.64	0.12/0.03	3.37/3.30	**87.67/87.44**	2.11/2.37	
OnTheStair	Chest	/0.03	1.34/1.76	9.22/8.88	0.12/0.15	4.73/4.66	0.75/1.07	**83.84/83.45**	**86.05/85.80**
	Forehead	0.06/0.03	1.16/1.79	9.09/7.91	0.03/0.12	3.54/4.12	1.04/1.24	**85.08/84.79**	
	Wrist	0.09/0.12	1.13/1.58	8.28/6.03	/0.15	2.76/3.73	0.68/0.96	**87.74/87.43**	
	Ankle	/0.06	1.58/1.64	7.45/6.64	0.18/0.21	2.98/3.21	0.25/0.73	**87.56/87.51**	

walking (89.18%), climbing (86.87%), running (87.77%), on the stair (85.80%) and crawling (82.72%). Both of them highly agree with the trend of result from isolated chamber. Three major observations remain as: 1) As static and semi-dynamic motions, lying, standing and walking still have higher classification rate compared with dynamic motions. 2) Static motions are usually misclassified as static motion. 3) Dynamic motions can be misclassified into multiple other motions.

The overall classification rate for corridor scenario is 87.84%, which is 0.85% lower than 88.69% in isolated chamber case. Office room scenario has an overall classification rate of 87.28%, which is 0.56% worse compared with corridor scenario. Since typical office room obviously suffers from more severe multipath effect, such result is expected. As a conclusion, slightly performance drop can be seen in multipath scenario, but such performance decrement is limited to small scale and our proposed method still achieve 87.28% classification rate.

The above analysis shows that a weaker but still satisfactory classification perfor-

Table 4.9: Classification of candidate human motions in multipath scenario (with human).

Actual Motion	Receiver Location	Predicted Human Motion							Overall (%)
		Standing (%)	Walking (%)	Runing (%)	Lying (%)	Crawing (%)	Climbing (%)	OnTheStair (%)	
Standing	Chest	**89.27/89.29**	0.15/0.15	/	10.56/10.50	/0.03	/0.03	/	**89.44/89.43**
	Forehead	**89.03/89.06**	0.18/0.21	/	10.73/10.65	/0.03	0.06/0.06	/	
	Wrist	**89.15/89.11**	0.15/0.15	/	10.67/10.67	/	0.03/0.06	/	
	Ankle	**90.30/90.27**	0.21/0.21	/	9.49/9.49	/	/0.03	/	
Walking	Chest	0.75/1.09	**89.68/89.70**	4.85/4.21	0.03/0.09	1.78/1.66	0.55/1.15	2.36/2.10	**89.18/89.19**
	Forehead	0.67/0.87	**88.83/88.86**	4.89/4.33	0.09/0.09	1.84/1.84	0.44/0.98	3.24/2.93	
	Wrist	0.67/0.84	**89.09/89.12**	1.78/1.69	0.15/0.12	4.92/4.27	0.41/0.87	2.98/3.09	
	Ankle	0.78/0.61	**89.12/89.09**	1.91/1.77	0.12/0.17	4.43/4.47	0.78/0.94	2.86/2.95	
Running	Chest	0.09/0.12	2.35/1.96	**86.86/86.89**	0.06/0.03	1.43/2.02	0.76/1.15	8.45/7.84	**86.77/86.77**
	Forehead	0.12/0.21	3.79/2.21	**86.01/86.24**	0.03/0.03	1.69/2.24	1.05/0.97	7.31/8.10	
	Wrist	0.09/0.09	1.67/2.42	**87.22/87.03**	0.09/0.15	1.98/2.21	0.48/0.88	8.56/7.21	
	Ankle	0.43/0.37	2.14/2.57	**86.97/86.92**	0.23/0.03	1.67/1.97	0.98/1.06	7.75/7.09	
Lying	Chest	9.64/9.57	/0.03	/	**90.33/90.36**	0.03/	/0.03	/	**90.42/90.44**
	Forehead	9.30/9.24	/	/	**90.67/90.68**	0.03/0.03	/0.06	/	
	Wrist	8.77/8.81	0.15/0.18	/	**90.33/90.33**	0.75/0.57	/0.12	/	
	Ankle	9.19/9.07	0.12/0.09	/	**90.36/90.41**	0.33/0.41	/0.03	/	
Crawling	Chest	0.33/0.47	3.98/4.67	2.21/2.44	0.61/0.85	**80.31/80.27**	8.58/6.67	3.98/4.62	**82.72/82.64**
	Forehead	0.47/0.65	3.82/4.45	2.16/2.86	0.44/0.82	**81.87/81.67**	6.93/5.58	4.31/3.97	
	Wrist	0.37/0.58	3.17/3.98	1.94/1.88	0.15/0.47	**85.21/85.54**	5.01/3.50	4.15/4.05	
	Ankle	0.44/0.61	4.29/4.23	2.08/2.97	0.15/0.74	**83.47/83.11**	5.39/4.51	4.22/3.83	
Climbing	Chest	0.79/0.58	5.32/5.32	0.67/0.92	0.15/0.47	6.06/6.49	**84.87/84.25**	2.14/1.97	**86.87/86.40**
	Forehead	0.28/0.44	6.08/5.58	0.33/0.75	0.06/0.43	5.20/5.29	**86.29/85.57**	1.76/1.94	
	Wrist	0.33/0.41	5.97/4.29	0.25/0.67	0.12/0.39	2.52/3.50	**88.89/88.66**	1.92/2.09	
	Ankle	0.41/0.52	6.11/4.26	0.64/0.86	0.03/0.47	3.30/4.55	**87.44/87.13**	2.37/2.21	
OnTheStair	Chest	0.03/0.12	1.76/1.39	8.88/7.55	0.15/0.37	4.66/4.91	1.07/2.37	**83.45/83.29**	**85.80/85.35**
	Forehead	0.03/0.15	1.79/1.27	7.91/6.93	0.12/0.41	4.12/4.69	1.24/2.11	**84.79/84.43**	
	Wrist	0.12/0.12	1.58/1.18	6.03/7.02	0.15/0.12	3.73/3.84	0.96/1.09	**87.43/86.64**	
	Ankle	0.06/0.09	1.64/1.46	6.64/6.61	0.21/0.18	3.21/3.47	0.73/1.13	**87.51/87.07**	

mance can be obtained from static multipath scenario, however, in order to validate the adaptability to dynamic multipath scenario, we repeated the experiment of office environment with 7 people randomly moving inside the room. Empirical results are depicted in Table 4.9, where the former number shows the classification rate for empty office room while the later number is the classification rate with 7 randomly moving human subjects. It is clear that classification rate does not change dramatically with the involvement of moving humans and we believe that can be explained by human shadowing theory in [GHDP13][GHWP13].

4.5.4 Comparison with Accelerometer Based Approaches.

The proposed approach achieves an average classification rate of 87.28% in the worst case (82.72%∼90.42%). In order to provide a horizontal comparison with existing accelerometer based motion classification approaches, we browsed the mostly cited works and listed them in Table 4.10.

Table 4.10: Comparison between accelerometer based approaches and the proposed approach.

Literature	Sensor	Classifier	Candidate Motion Number	Accuracy Range(%)
J. Kwapisz[KWM10]	Single Accl.	Logistic Regression	5	61.5 $\sim$ 98.3
S. Zhang[ZMNZ10]	Single Accl.	SVM	4	49.1 $\sim$ 87.2
J. Mantyjarvi[MHS01]	Multiple Accl.	MLP Neural Network	4	83.0 $\sim$ 90.0
X. Long[LYA09]	Single Accl.	Principle Component Analysis	6	71.3 $\sim$ 92.9
Our Approach	RF	SVM	7	82.7 $\sim$ 90.4

Considering classification accuracy, existing accelerometer based approaches as high as 98.3% for specific candidate motions. However, both Kwapisz's and Zhang's work suffers from low accuracy when classifying static cases such as standing and sitting. The proposed approach in this chapter may not score over 98% classification rate, but its accuracy range is relatively small, resulting in more stable performance. Apart from that, most of the accelerometer based approaches are capable to classify standing, sitting, walking and running. Kwapisz's and Long's work also covered on the stair cases. The proposed approach supports a broader candidate motion set, which is suitable for first responder applications. Last but not the least, it worth mentioning that in general classification problems, additional information usually improves the classification accuracy as long as it's tightly coupled with the problem itself. The hybrid of accelerometer based approach and RF based approach may further improve the performance.

4.6 Summary.

In this chapter, we investigated the feasibility of classifying different human motions based on RF features collected by on-body health monitoring system. Empirical data of 3 human subjects performing seven different candidate motions were obtained by VNA based measurement system. A set of 10 most significant RF features are derived and their pair wise correlation were examined. All-data-at-once

SVM was trained utilizing extracted RF features to classify the candidate motions. Classification accuracy based on entire 10 features was found to be around 88.69%.

To thoroughly understand the performance of our approach, effect of both human motion and sensor location has been investigated. We divided the motion set into static and dynamic categories and showed how these two aspects influence the detailed classification accuracy. While the results shown in this study are promising, we also analyzed the potential of decreasing necessary feature number to simplify the implementation of overall approach. With 8 most important RF features, the proposed scheme still achieved over 80% classification rate for all candidate motions. That number may be further reduced if less candidate motions are considered.

Our proposed scheme was fully capable for accurate human motion classification on a real-time, continuous basis. Such approach can be regarded as the first step toward realizing motion classification functionality on on-body monitoring networks. With the presented investigation results, it could be shown that the proposed scheme can support applications such as first responder survival system or smart healthcare system. Since SVM is only one of the available supervised learning algorithm in the open literature, the future work may include the implementation and comparison of multiple algorithms such as K-nearest algorithm, Neural network algorithm and etc.

Chapter 5

In-Body Radio Propagation and Wireless Capsule Endoscopy Hybrid Localization.

Wireless Capsule Endoscopy (WCE) is progressively emerging as the most popular non-invasive imaging tool for the diagnostic of Gastrointestinal (GI) tract diseases such as inflammatory bowel disease, ulcerative colitis and colorectal cancer. The WCE is a swallowable, pill-like micro-robot equipped with a tiny camera and a LED illuminating system for capturing images of the inside of GI tract [IMGS00][KZS+12][KB11]. A Radio Frequency (RF) transmission module is embedded in the WCE for sending the captured images wirelessly to the external on-body receivers [CMD11]. Theoretically, the transmitted RF signals and captured images should allow us to localize the capsule and reconstruct its 3D movement path inside the human small intestine. Precise 3D reconstruction of the movement path helps physicians to associate the absolute location information with the intestinal abnormality upon observation. Apart from that, the path reconstruction also enables other micro-robotic surgeries

and at the same time unfolds the mysterious interior small intestine environment to the research community for educational purposes. Due to the complex and non-homogeneous environment of inside human body, fourteen years after the invention of WCE [IMGS00], 3D reconstruction of the WCE movement path inside the small intestine is still in its infancy.

The key to implement 3D reconstruction is the precision of localization inside the small intestine, an organ with an average length of seven meters randomly curled and concentrated in the several hundreds cm^3 of cramped space inside human abdomen [TAZL12][PBY+12]. To meet the demand on WCE location information, many attempts have been made during the past few years to localize the WCE, and thus, reconstruct the 3D path. Existing literatures investigated various WCE localization approaches including radiological imaging, magnetic localization, image processing, RF localization, and even inertial sensing [KK15][TAZL12], but these location estimations are crude and the accuracy does not exceed a few centimeters [PBY+12][FC08][KPM11]. Without adequate localization accuracy, any kind of 3D reconstruction loses its fidelity. To further enhance the WCE localization performance and enable 3D reconstruction of the path, a very intuitive solution is to develop hybrid localization systems that benefit from the combination of multiple independent measurements of capsule location [PBM13][PFJ12].

In our most recent research we proposed a prototype WCE hybrid localization approach that combines the received signal strength (RSS) based RF localization with the image processing based movement tracking [BPM15]. In this chapter, we investigate the problem from the analytical perspective and derive the 3D Posterior Cramer-Rao Lower Bound (PCRLB) for the WCE hybrid localization. The PCRLB serves as the fundamental framework for performance analysis of the hybrid localization approach and it can be applied to RF localization with both RSS ranging

and Time-of-Arrival (TOA) ranging. Using the PCRLB framework and existing models in the literature, we demonstrate that 2.4cm accuracy is achievable using image and RF hybrid localization with RSS ranging and 4.1mm accuracy is achievable with TOA ranging. The millimetric level of accuracy proves the feasibility of precise 3D reconstruction of the WCE movement path inside the small intestine. We also carried out *monte carlo* simulation on the PCRLB to discuss the effects of WCE movement estimation, the effects of system bandwidth as well as the effects of on-body sensor numbers and sensor placements.

Our further discussions are structured as follows. Existing literatures toward WCE localization with a particular focus on RF based and image processing based techniques are reviewed in section 5.1. Description of our WCE hybrid localization algorithm is introduced in section 5.2. The derivation of 3D posterior Cramer-Rao lower bound for the WCE hybrid localization approach is proposed in section 5.3. Most significantly, the effects of movement measurement accuracy, on-body RF receiver number, on-body RF receiver placement and RF localization system parameters are carefully investigated and reported in section 5.4. Section 5.5 summarizes the overall work and closes our discussion.

5.1 Background.

5.1.1 Existing Camera/RF Based Localization Techniques.

The initial exploration for WCE localization system starts from intuitive radiological medical imaging technologies including planar X-Ray [SHK+05][BRS10], Computed Tomography (CT) [JSH+08][SJL+14], Gamma Ray [TAH+12] and Magnetic Resonance Imaging (MRI) [MMF+09][KSM+05]. However, such procedures are not easily combined with capsule endoscopy and the continuous radiological imaging over sev-

eral hours ends up with a contradiction between better localization performance and higher health risk caused by radiation overdose [TAZL12]. To avoid such health risk, magnetic field based approaches with low-frequency and low-power magnetic signals have been considered promising alternatives [HLS+10][AGV08][WHP+08]. The interaction between magnetic field and human body is negligible and the actuation system for WCE can be implemented potentially. The major obstacle that prevents the magnetic field based approach from clinical applications is that the embedded permanent magnet or secondary coil enhance the dimension and weight of the capsule, which violates the miniaturization principle of implantable devices to some scale [HMM09].

The physical limitations placed on the WCE localization system also encourage the exploration of technologies that can obtain location information from existing infrastructures, which include video from the small intestine and the Radio Frequency (RF) signals emitted from the capsule. During the treatment, the WCE continuously takes photos of inside GI tract at a rate of up to 6 frames per second and the photos eventually form the video [IMA+09]. Considering each photo as a specific step of the capsule, there are image processing based approaches in our previous work, tracking the capsule by comparing adjacent photos and modeling its movement step by step [BYK+12][BP12]. Such approaches perform well at the initial period but gradually lose its accuracy due to the accumulation of error [BP12]. Apart from the image based approach, RF signals have been employed in localization science and technology since the era of global positioning system (GPS). However, RF localization inside human body is not trivial. Inside human body is an extremely complex medium for RF propagation since it is a non-homogeneous, liquid-like environment with irregularly shaped boundaries and severe propagation loss [SYHT09][AY09][GWHP13]. It is reported that conventional RSS based RF localization approach for WCE ap-

plications results in a few centimeters inaccuracy [YKA+11][WFY+11], which still needs further improvement before clinical practices.

5.1.2 Evolution of RF Localization Inside Human Body.

The initial phase of any range based RF localization process is to estimate the distance between an target with unknown location and a reference with known location. After that, a triangulation algorithm can be performed with more than 3 range estimation to calculate the location of the target. Amount the various available ranging techniques, only RSS and TOA has been selected as ranging metric between the capsule pill and on-body RF receivers [TAZL12]. There is no report using Angle-of-Arrival (AOA) based technique due to the fact that the RF signal suffers from refraction and scattering caused by irregularly shaped boundaries of human organs [PBY+12].

The conventional RSS based RF localization appeared even before the standard channel model for implantable devices was published. Fisher et, al. measured the signal strength of WCE emitted signals and proposed a localization algorithm simply use the intuition that the closer WCE is to the on-body receiver, the stronger signal can be caught [FSM+01][FSLE04]. Later on, with the available Medical Implant Communication Service (MICS) band pathloss model for in-body radio propagation channel, a number of different algorithms have been tried to implement a better RF localization system using RSS ranging [LGP12][AA07][SAV07]. However, none of these approaches can achieve better than 10cm accuracy and thus, making the localization system not applicable to clinical treatments. In the seek for better localization approaches, RF localization with TOA ranging comes into the picture. The first attempt of TOA based RF localization for WCE applications was proposed by Khan et, al., in [KPM11] where the Finite Difference Time Domain (FDTD) method

has been adopted to simulate the propagation of radio wave through the human body and achieved around 4cm localization accuracy. The computational approach using FDTD was validated by [LCK+13] using homogeneous liquid and human shape phantom, which reinforced the possibility of using TOA based RF localization inside human body. Clearly, existing researches shows that the conventional WCE localization fails to provide enough localization accuracy to reliably support the WCE clinical application and people are constantly trying to hybrid multiple possible sources to provide precise WCE location information [SVQ+10][LWLM11]. All existing hybrid approaches are dwelling at the laboratory experimental phase and it is urgent to bring it one step further to clinical applications.

5.1.3 Cramer-Rao Lower Bound for WCE Localization.

In estimation theory and statistics, the Cramer-Rao Lower Bound (CRLB) expresses a lower bound on the variance of estimators of a deterministic parameter [Tre68][Poo94]. In its simplest form, the bound states that the variance of any unbiased estimator is at least as high as the inverse of the Fisher information [Poo94]. Since the CRLB develops the lowest possible root-mean-square (RMS) error among all unbiased methods, it has been soon applied to navigation and geolocation science and technology [PAK+05][GG05]. CRLB has been discovered to be able to estimating the max possible performance of certain localization system or evaluating the potential improvement of specific localization algorithm. Both aspects help avoiding unnecessary implementation of the actual localization approach [PHP+03][MPG14].

During the evolution of in-body RF localization, 3D CRLB for WCE location estimation has been also derived, calculated and analyzed. The pioneer work of investigating the WCE localization accuracy inside the human body is proposed by Wang et, al. in [WFY+11], in which approximately 12.5cm CRLB has been observed

using the conventional RF localization with RSS ranging. This work expanded the 2D CRLB calculation into 3D space and exploit the channel model provided in the first draft of IEEE 802.15.6 [Tg610][CSSK$^+$13]. Wang's work only considered a fixed topology of on-body sensors, that is, 4 RF receivers uniformly deployed on the front side of human body and another 4 receivers mirroring at the rear side. Soon after, Ye et al., brought Wang's work one step further to multiple on-body sensors and various formations of sensor deployments [YSPG12]. Three different organs including stomach, small intestine and large intestine are investigated in [YSPG12][SYGP12] and it is reported that with more than 60 on-body receivers, approximately 4.5cm of localization accuracy can be achieved with conventional RF localization using RSS ranging. The performance of RF localization with TOA ranging has been also analyzed in [YPB$^+$14], in which ray-tracing technique was employed to obtain average relative permittivity and the propagation velocity of signals can be estimated. Also, TOA ranging achieved 2.3cm localization accuracy with 8 on-body sensors and little less than 1cm accuracy with more than 60 sensors. The TOA ranging system in [YPB$^+$14] is fixed to the UWB channel provided in IEEE 802.15.3a standard [Tg303][MFP03] and the CRLB in [YPB$^+$14] has no flexibility to be expanded to other wideband channels. Obviously, there is no existing work investigating the CRLB for any possible WCE hybrid localization approach and we believe this study can fulfill the blank and promote relative theoretical analysis to the next level.

5.2 Hybrid Localization System for WCE.

In this section, we provide the general description of our hybrid localization algorithm, which includes image processing based movement tracking and RF based localization. Since the time interval between two adjacent states of WCE is trivial,

we assume that the WCE moves at a constant velocity in the state transition. With the constant velocity model, a classic Kalman Filter has been used to hybrid the available information.

5.2.1 Image Processing Based Movement Tracking.

The movement trajectory of WCE can be calculated by analyzing the displacements of unique portion of the scene between consecutive frames. The unique portion is referred as feature points (FPs). Transformation between frames such as rotation, translation and scaling can be extracted from the behavior of FPs, and therefore, used in quantitative calculation of the WCE movement for each step. Since the endoscopic images suffer from geometric distortions and illumination variations, it is important to guarantee that the FPs extracted from reference frame can be accurately detected in the following frame. Affine Scale Invariant Feature Transform (ASIFT) algorithm has been reported outperforming other existing methodologies in the above mentioned environment [FM11][HLL11] and it has been selected as the FPs detection method in this approach. Typical FPs matching process is depicted in Fig 5.1. Note that it is not necessary that all FPs are correctly matched, bad matching can be easily filtered out by applying a neighboring feature vector comparison.

Given reliable matching of FPs, a physical procedure has been employed to quantitatively estimate the step length[1] and moving direction of the capsule. As shown in Fig 5.2, let G_p, ($p \in [1, P]$) be the pth selected FP out of the totally P FPs, C_k be the camera's position at kth state, D be the distance between G_p and C_k. The angular depth of point G_p can be estimated as p_k. With the camera moving

[1]If a constant velocity model is used to describe the movement of capsule, step length shares the similar concept of velocity and they can be linked as distance equals to velocity times the time interval.

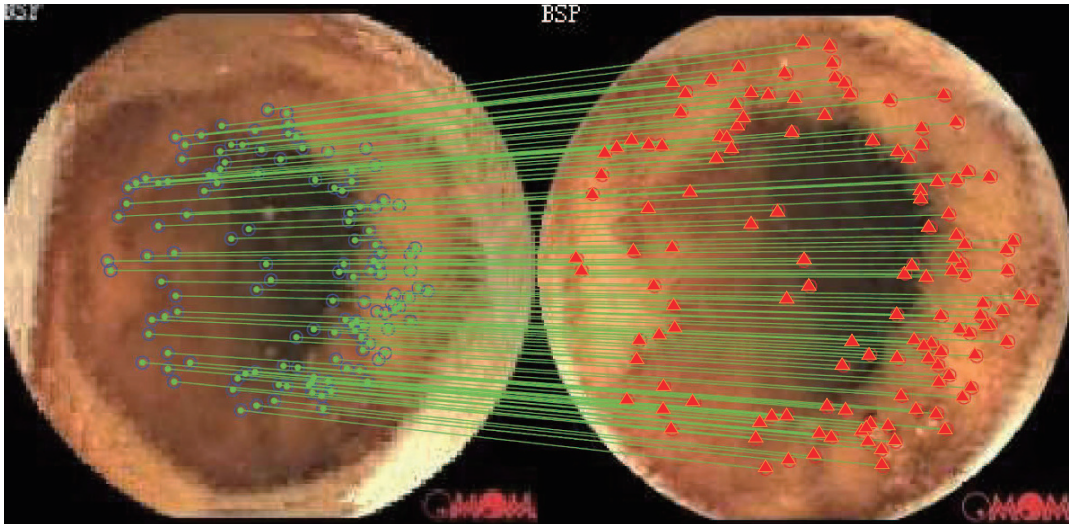

Figure 5.1: Feature points matching between consecutive frames using ASIFT. Blue "O" represents the selected FPs in the reference frame and red "Δ" represents the matched FPs in the following frame.

forward by a distance d_p to reach a new position C_{k+1} at the next state, another angular depth of G_p at $(k+1)$th state can be estimated as p_{k+1}. These angular depths can be represented by

$$p_k = \tan^{-1}\frac{R}{D} \;\;,\;\; p_{k+1} = \tan^{-1}\frac{R}{D-d_p} \tag{5.1}$$

By substitution, for any selected FP, the step length d_p between consecutive frames can be given as

$$d_p = \frac{R}{\tan p_{k+1}}\left(1 - \frac{\tan p_{k+1}}{\tan p_k}\right) \tag{5.2}$$

Applying an averaging to the step length estimation from multiple FPs, the final WCE step length estimates for the transition from kth to $(k+1)$th states can be calculated by

$$\hat{d}_k = \sum_{p\in[1,P]} d_p = \sum_{p\in[1,P]} \frac{R}{\tan p_{k+1}}\left(1 - \frac{\tan p_{k+1}}{\tan p_k}\right) \tag{5.3}$$

Note that the averaging process not only gives a better estimate of $\hat{d}_k$, it also provides generality of the calculation and make the calculation valid no matter the small intestine is straight or bent.

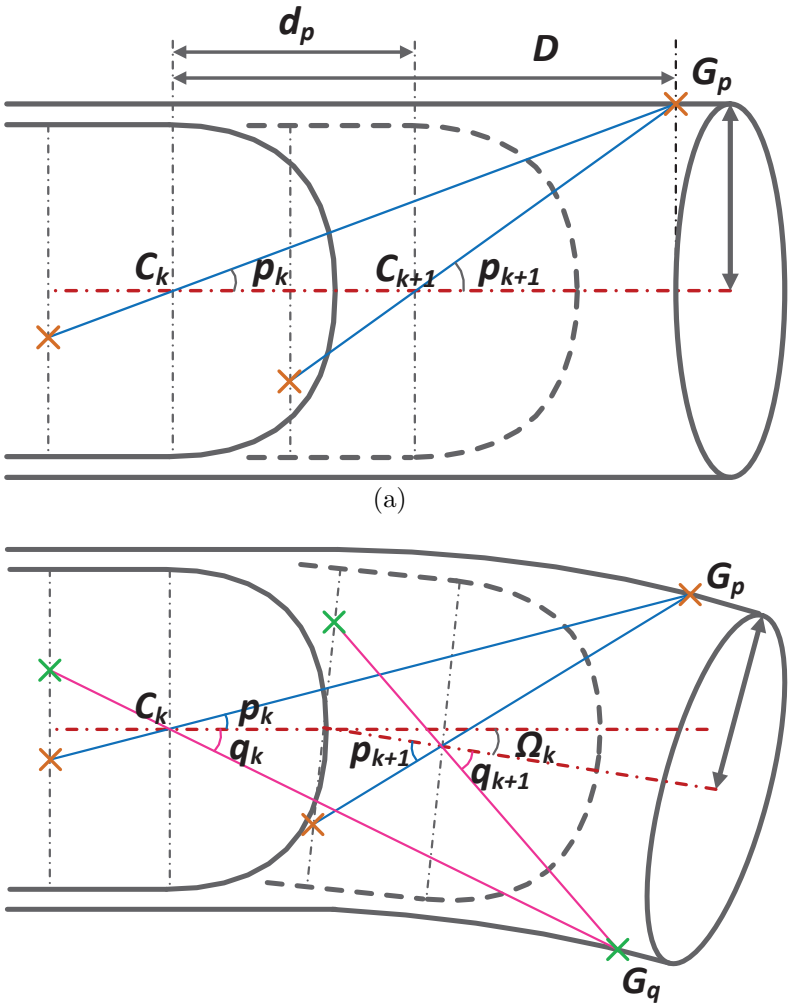

Figure 5.2: Geographic model for WCE movement estimation. (a):Estimation of WCE step length. (b):Estimation of WCE heading direction.

The moving direction of the capsule can be also calculated as shown in Fig 5.2. Define the magnitude of the tilting angle of the transition from the kth state to the $(k+1)$th state as Ω_k, selecting FP G_p and G_q with the same distance from capsule's position C_k, we obtain angular depths p_k and q_k for the kth state. After that, the

capsule moves to C_{k+1} with a tilt of Ω_k and we measure p_{k+1}, q_{k+1}, $\delta_p = p_{k+1} - p_k$ and $\delta_q = q_{k+1} - q_k$. Then the magnitude of tilting can be roughly estimated by

$$\hat{\Omega}_k = \min_{p,q \in [1,P] \text{ and } p \neq q} \left(\frac{\delta_q - \delta_p}{\max(\delta_q, \delta_p)} \right) \tag{5.4}$$

We also record the FP $G_{\text{arg},k} = (x_{\text{arg},k}, y_{\text{arg},k})$ as the argument that provides the minimum $\hat{\Omega}_k$, where $(x_{\text{arg},k}, y_{\text{arg},k})$ is its coordinate in the kth video frame. So that the direction of tilting $\phi_{\text{arg},k}$ can be represented by

$$\phi_{\text{arg},k} = \tan^{-1} \left(\frac{y_{\text{arg},k} - y_0}{x_{\text{arg},k} - x_0} \right) \tag{5.5}$$

where (x_0, y_0) is the center of the frame. With the direction $\phi_{\text{arg},k}$, $\hat{\Omega}_k$ can be further decomposed into pitch angle $\hat{\alpha}_k = \hat{\Omega}_k \cos \phi_{\text{arg},k}$ and yaw angle $\hat{\beta}_k = \hat{\Omega}_k \sin \phi_{\text{arg},k}$. The estimation of roll angle $\hat{\gamma}_k$ is trivial and can be easily calculated by image unrolling technique [BYK+12].

The above mentioned direction estimation is based on the yaw-pitch-roll description in the camera coordinate and it can be transformed into the heading-elevation-bank description in the world coordinate by a standard rotation matrix. Define the capsule's direction at the kth state by a norm vector $(n_{x,k}, n_{y,k}, n_{y,k})^T$ in the world coordinate, it can be updated to the $(k+1)$th state by

$$\begin{bmatrix} n_{x,k+1} \\ n_{y,k+1} \\ n_{z,k+1} \end{bmatrix} = \mathbb{R} \begin{bmatrix} n_{x,k} \\ n_{y,k} \\ n_{z,k} \end{bmatrix} \tag{5.6}$$

where $\mathbb{R} = \mathbb{R}\mathbb{R}_k\mathbb{R}^{-1}$ is the accumulative rotation matrix and $\mathbb{R}_k$ is the standard rotation matrix that contains yaw-pitch-roll information. With all above analyzed

information as well as the step time interval as the metadata of WCE, conventional localization with image processing based technique can be achieved given a initial position of the capsule.

5.2.2 Radio Frequency Based WCE Localization.

In the conventional RF localization approaches, a bunch of calibrated external antennas are attached to the abdominal wall surface of the human to detect the wireless signal emitted by the WCE. Upon the reception of the signal, either the RSS or the TOA can be employed to identify the distance between the capsule and a specific body mounted receiver. As for RSS based ranging, the statistical radio propagation channel model can be used to provide the relationship between RSS and distance estimate. The standard channel model of IEEE 802.15.6 at MICS band [Tg610] has been employed in this study as

$$\mathrm{RSS}(\hat{l}_{k,n}) = \mathrm{P}_t - \mathrm{L}_p(l_0) - 10\alpha \log_{10} \frac{l_{k,n}}{l_0} + \zeta,\ n \in [1, N] \tag{5.7}$$

where $l_{k,n}$ denotes to the actual distance between the capsule endoscopy and nth on-body RF receiver, N is the total number of on-body RF receiver, P_t is the constant transmit power of capsule endoscopy, $\mathrm{L}_p(l_0)$ is the path-loss at reference distance l_0 (i.e. 50mm in this work), α denotes to the distance-power gradient and ζ denotes to the shadow fading effect. The ranging estimate can be shown as

$$\hat{l}_{k,n} = 10^{\left(\frac{\mathrm{RSS}(\hat{l}_{k,n}) - \mathrm{P}_t + \mathrm{L}_p(l_0)}{10\alpha}\right)} \times l_0,\ n \in [1, N] \tag{5.8}$$

Note that all necessary parameters are shown in Table 5.1.

The TOA based ranging technique uses the time of flight of the signal to estimate

Implant to Body Surface	$L_p(l_0)$ (dB)	α	ζ (dB)
Deep tissue	47.14	4.26	7.85
Near surface	49.81	4.22	6.81

Table 5.1: Parameters for IEEE 802.15.6 in-body radio propagation channel, from implant to body surface.

the actual distance between the capsule endoscopy and nth on-body RF receiver and the range estimate can be given as

$$\hat{l}_{k,n} = \frac{c \times \hat{t}_{k,n}}{\sqrt{\varepsilon_{\text{ave}}}},\ n \in [1, N] \tag{5.9}$$

where c is the speed of light, ε_{ave} [KK09] is the average relative permittivity inside small intestine and $\hat{t}_{k,n}$ denotes the propagation time of the signal.

With more than 3 estimated ranging between the capsule and body mounted RF sensors, the 3D position of the capsule can be solved by minimizing the following function

$$\mathcal{F}_k(x, y, z) = \sum_{n=1}^{N} \left(\sqrt{(x - x_{n,k})^2 + (y - y_{n,k})^2 + (z - z_{n,k})^2} - l_{k,n}^2 \right)^2 \tag{5.10}$$

5.2.3 Hybrid Localization for WCE.

Based on the discussion of previous sections, let $\boldsymbol{m}_k = [x_k, y_k, z_k, n_{x,k}, n_{y,k}, n_{z,k}]^T$, $(k = 1, ..., K)$ be the state vector at the kth state, where (x_k, y_k, z_k) is the 3D location coordinate of the capsule in world coordinate space and $[n_{x,k}, n_{y,k}, n_{z,k}]^T$ is the norm vector indicating direction of capsule movement. K is the total number of frames in the video taken by WCE camera. We define $\bar{\hat{\boldsymbol{m}}}_k$, as the predicted position of the capsule from image processing based WCE tracking and define $\hat{\boldsymbol{z}}_k$ as the measured capsule position from RF based WCE localization. The system state

transition function can be given as [HGLX14][GCF+16]

$$\begin{cases} \bar{\hat{\boldsymbol{m}}}_{k+1} = \boldsymbol{A}_k \hat{\boldsymbol{m}}_k + \boldsymbol{q}_k \\ \boldsymbol{z}_{k+1} = \boldsymbol{H}_k \bar{\hat{\boldsymbol{m}}}_k + \boldsymbol{r}_k \end{cases} \tag{5.11}$$

where $\boldsymbol{q}_k$ is the inaccuracy of movement estimation that follows Gaussian distribution with covariance $\boldsymbol{Q}$ and $\boldsymbol{r}_k$ is the inaccuracy of RF based location estimation that follow Gaussian distribution with covariance $\boldsymbol{R}$. The matrix $\boldsymbol{A}_k$ and matrix $\boldsymbol{H}_k$ can be given as

$$\boldsymbol{A}_k = \begin{bmatrix} 1 & 0 & 0 & \hat{d}_k & 0 & 0 \\ 0 & 1 & 0 & 0 & \hat{d}_k & 0 \\ 0 & 0 & 1 & 0 & 0 & \hat{d}_k \\ 0 & 0 & 0 & & & \\ 0 & 0 & 0 & & [\mathbb{R}] & \\ 0 & 0 & 0 & & & \end{bmatrix}, \quad \boldsymbol{H}_k = \begin{bmatrix} 1 & 0 & 0 & 0 & 0 & 0 \\ 0 & 1 & 0 & 0 & 0 & 0 \\ 0 & 0 & 1 & 0 & 0 & 0 \end{bmatrix} \tag{5.12}$$

If we define the priori estimate error covariance as $\bar{\boldsymbol{P}}_k = E[(\boldsymbol{m}_k - \bar{\hat{\boldsymbol{m}}}_k)(\boldsymbol{m}_k - \bar{\hat{\boldsymbol{m}}}_k)^T]$ and define the posteriori estimate error covariance as $\boldsymbol{P}_k = E[(\boldsymbol{m}_k - \hat{\boldsymbol{m}}_k)(\boldsymbol{m}_k - \hat{\boldsymbol{m}}_k)^T]$, a classic Kalman filter can be exploited to hybrid the information from both image processing based and RF based localization. The mathematical description of the WCE hybrid localization approach is shown in *Algorithm* 1 and the performance of the hybrid approach will be discussed later in Section V.

Algorithm 1 Kalman filtering for WCE hybrid localization

Initialize $\hat{\boldsymbol{z}}_1$ upon detection of Pylorus;
Initialize $\hat{\boldsymbol{m}}_1 = \hat{\boldsymbol{z}}_1$;
Initialize $\boldsymbol{P}_1$;
for $k = 2$ to K, **do**
  predict the state, $\bar{\hat{\boldsymbol{m}}}_k = \boldsymbol{A}\hat{\boldsymbol{m}}_{k-1}$;
  predict state error covariance, $\bar{\boldsymbol{P}}_k = \boldsymbol{A}\boldsymbol{P}_{k-1}\boldsymbol{A}^T + \boldsymbol{Q}$;
  update the rotation matrix, $\mathbb{R} = \mathbb{R}\mathbb{R}_k\mathbb{R}^{-1}$;
  compute Kalman gain, $\boldsymbol{K}_k = \bar{\boldsymbol{P}}_k\boldsymbol{H}^T(\boldsymbol{H}\bar{\boldsymbol{P}}_k\boldsymbol{H}^T + \boldsymbol{R})^{-1}$;
  update the state $\hat{\boldsymbol{m}}_k = \bar{\hat{\boldsymbol{m}}}_k + \boldsymbol{K}_k(\boldsymbol{z}_k - \boldsymbol{H}\bar{\hat{\boldsymbol{m}}}_k)$
  update state error covariance, $\boldsymbol{P}_k = (\boldsymbol{I} - \boldsymbol{K}_k\boldsymbol{H})\bar{\boldsymbol{P}}_k$
end

5.3 Fundamental Limits for WCE Localization.

Originally, the fundamental limits on the performance of RF localization are carried out by Cramer-Rao Lower Bound (CRLB), in which all the observations are independent from each other. However, in the image processing based movement tracking, the independency among observations no longer exists due to the fact that the posterior information from previous status is required. To properly represent the best possible performance of the hybrid localization, PCRLB has been employed. We only present the mathematical derivations in this section and leave all performance evaluation and related analysis to the following sections.

In terms of notations, we define $\nabla_{\boldsymbol{a}} = [\frac{\partial}{\partial a_1}, ..., \frac{\partial}{\partial a_M}]^T$ as the first-order derivatives and $\Delta_{\boldsymbol{b}}^{\boldsymbol{a}} = \nabla_{\boldsymbol{b}}\nabla_{\boldsymbol{a}}^T$ as the second-order derivatives. $p(\boldsymbol{a})$ is the probability density function (p.d.f) of random vector $\boldsymbol{a}$, where $[\boldsymbol{a}]_i$ is the ith element in vector $\boldsymbol{a}$. Kronecker product is denoted by $\otimes$, matrix trace is given as $\mathrm{Tr}\{\bullet\}$ and diagonal matrix is given as $\mathrm{diag}\{\bullet\}$. These notations serve for the remainder of this chapter.

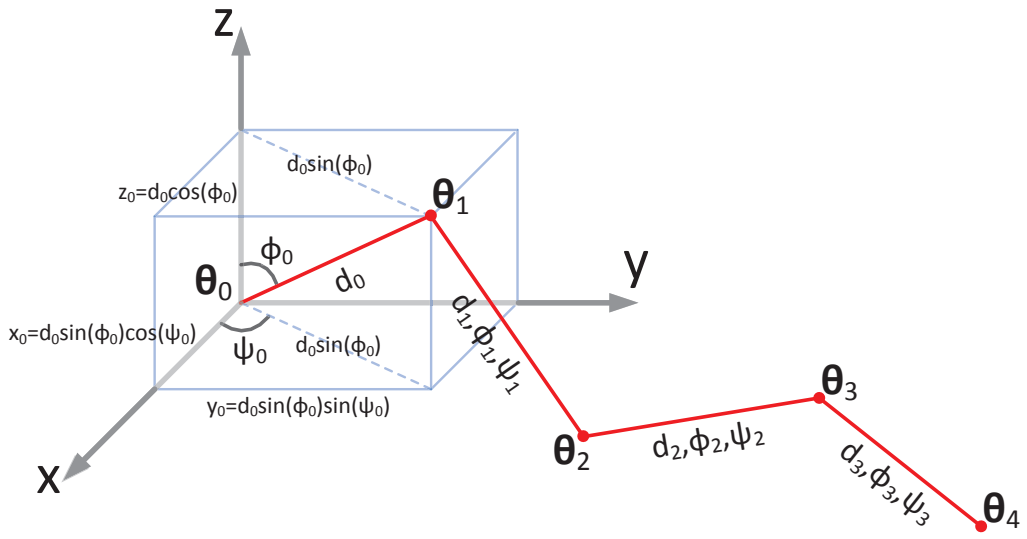

Figure 5.3: Illustration of WCE state transition. Camera consecutively takes picture at 4 different states $\boldsymbol{\theta}_k$, $(k \in [0,4])$. The step length d_k $(k \in [0,3])$, horizontal heading ψ_k $(k \in [0,3])$ and vertical elevation ϕ_k $(k \in [0,3])$ are recorded. Given the initial state $\boldsymbol{\theta}_0$, capsule's location at states $\boldsymbol{\theta}_k$ $(k \in [1,4])$ can be determined, respectively.

5.3.1 Sources of Uncertainty.

Fig 5.3 depicts the 3D scenario that a capsule endoscopy moving along the small intestine, sequentially taking pictures every 0.5s to form K different states step by step. We label the capsule's location at kth state as a vector $\boldsymbol{\theta}_k = [x_k,\ y_k,\ z_k]^T$ $(k \in [0, K-1])$, to represent the 3D coordinate. The entire state information can be formed as a vector $\boldsymbol{\theta} = [\boldsymbol{\theta}_0, \boldsymbol{\theta}_1, ..., \boldsymbol{\theta}_{K-1}]^T$ to model the movement of capsule endoscopy inside small intestine, for which each element $\boldsymbol{\theta}_{k+1}$ can be given as

$$\boldsymbol{\theta}_{k+1} = \boldsymbol{\theta}_k + d_k \mathbf{w}_k + \boldsymbol{\gamma}_k \tag{5.13}$$

where d_k is the actual step length between kth and $(k+1)$th step.

$\mathbf{w}_k = [\sin\phi_k \cos\psi_k,\ \sin\phi_k \sin\psi_k,\ \cos\phi_k]$ shows the capsule moving direction from kth step to $(k+1)$th step (See Fig 5.3). $\boldsymbol{\gamma}_k$ is the combined inaccuracy from

estimates of step length d_k, horizontal heading ψ_k and vertical elevation ϕ_k.

Step length estimates from image processing based approach in section 5.3 reads

$$\hat{d}_k = d_k + e_k,\ e_k \sim N(0, \sigma_k^2) \tag{5.14}$$

where d_k is the actual distance given as

$$d_k = \sqrt{(x_{k+1} - x_k)^2 + (y_{k+1} - y_k)^2 + (z_{k+1} - z_k)^2} \tag{5.15}$$

e_k is the measurement noises that can be modeled as uncorrelated zero-mean Gaussian random variable with variances σ_k^2. Vector $\hat{\boldsymbol{d}} = [\hat{d}_0, \hat{d}_1, ..., \hat{d}_{K-2}]^T$ is introduced to collect $\hat{d}_k$.

Horizontal heading estimates from image processing based approach reads

$$\hat{\psi}_k = \psi_k + u_k,\ u_k \sim N(0, \epsilon_k^2) \tag{5.16}$$

where ψ_k is the actual horizontal heading given as

$$\psi_k = \tan^{-1} \frac{y_{k+1} - y_k}{x_{k+1} - x_k} \tag{5.17}$$

u_k is uncorrelated zero-mean Gaussian random variable with variances ϵ_k^2, which is independent from z direction and is also uncorrelated with $\hat{\boldsymbol{d}}$. Vector $\hat{\boldsymbol{\psi}} = [\hat{\psi}_0, \hat{\psi}_1, ..., \hat{\psi}_{K-2}]^T$ is introduced to collect $\hat{\psi}_k$.

Vertical elevation estimates from image processing based approach reads

$$\hat{\phi}_k = \phi_k + v_k,\ v_k \sim N(0, \xi_k^2) \tag{5.18}$$

where ϕ_k is the actual vertical elevation given as

$$\phi_k = \tan^{-1} \frac{\sqrt{(x_{k+1} - x_k)^2 + (y_{k+1} - y_k)^2}}{z_{k+1} - z_k} \tag{5.19}$$

v_k is uncorrelated zero-mean Gaussian random variable with variance ξ_k^2, which is uncorrelated with both $\hat{\boldsymbol{\psi}}$ and $\hat{\boldsymbol{d}}$. Vector $\hat{\boldsymbol{\phi}} = [\hat{\phi}_0, \hat{\phi}_1, ..., \hat{\phi}_{K-2}]^T$ is introduced to collect $\hat{\phi}_k$.

In addition to all these location information obtained from image processing technique, at each state, the capsule endoscopy can also obtain a range-based RF location estimate $\hat{\boldsymbol{r}}_k$ with p.d.f. $p(\hat{\boldsymbol{r}}_k|\boldsymbol{\theta}_k)$, which can be obtained from multiple pair-wise range estimates. Note that $\hat{\boldsymbol{r}}_k$ are assumed to be uncorrelated with $\hat{\boldsymbol{d}}$, $\hat{\boldsymbol{\psi}}$ and $\hat{\boldsymbol{\phi}}$. It is also assumed to be independent among different states.

For RSS based technique, at the kth state, the pair-wise range estimate between the capsule endoscopy and nth on-body RF receiver, $\hat{l}_{k,n}$, can be derived from the path-loss model in Equation (8) Then the inaccuracy of RSS based ranging can be given as a zero-mean Gaussian random variable with a variance $\lambda_{k,n}$ as [PAK+05]

$$\lambda_{k,n} = \frac{(\zeta l_{k,n} \ln 10)^2}{(10\alpha)^2} \tag{5.20}$$

For TOA based technique, the range estimate is provided in Equation (9) and the variance of pair-wise range estimate can be given as [SW10]

$$\lambda_{k,n} = \frac{c_{\text{ave}}^2}{[8\pi^2\beta^2(1 - \chi_{k,n})\text{SNR}_{k,n}]} \tag{5.21}$$

where $\text{SNR}_{k,n}$ is the signal-to-noise ratio for line-of-sight (LOS) path, c_{ave}^2 denotes to the average speed of light inside human body, $(1 - \chi_{k,n}), \chi \in [0, 1)$ scales the effect of multipath phenomenon, which is 0 in the condition that multipaths can be

completely resolved. β is the effective bandwidth as [SW10]

$$\beta^2 = \frac{\int f^2 |S(f)|^2 df}{\int |S(f)|^2 df} \tag{5.22}$$

where $S(f)$ is the Fourier transform of the transmitted waveform $s(t)$. With all the properly modeled source of error, the fundamental limit on hybrid localization accuracy can be calculated accordingly.

5.3.2 Posterior Cramer-Rao Lower Bound Calculation.

As is mentioned at the beginning of this section, regarding the time-variant statistical system models for hybrid WCE localization, CRLB is most frequently used to provide the performance lower bound. With posterior information of random parameters such as step length, heading and elevation, CRLB can be extended to PCRLB. In this subsection, we introduce the mathematical basis for PCRLB calculation.

The best place to start PCRLB derivation is the joint p.d.f. as follow

$$p(\hat{\boldsymbol{r}}, \hat{\boldsymbol{d}}, \hat{\psi}, \hat{\phi}, \hat{\boldsymbol{\theta}}) = p(\hat{\boldsymbol{r}}_0|\boldsymbol{\theta}_0) \prod_{k=0}^{K-2} p(\hat{d}_k|\boldsymbol{\theta}_{k+1}, \boldsymbol{\theta}_k) p(\hat{\psi}_k|\boldsymbol{\theta}_{k+1}, \boldsymbol{\theta}_k)$$

$$p(\hat{\phi}_k|\boldsymbol{\theta}_{k+1}, \boldsymbol{\theta}_k) p(\hat{\boldsymbol{r}}_k|\boldsymbol{\theta}_{k+1}) \tag{5.23}$$

for which the PCRLB of estimating WCE location $\boldsymbol{\theta}$ can be given as [Tre68]

$$\mathbf{E}_{\hat{\boldsymbol{r}}, \hat{\boldsymbol{d}}, \hat{\psi}, \hat{\phi}}[(\hat{\boldsymbol{\theta}} - \boldsymbol{\theta})(\hat{\boldsymbol{\theta}} - \boldsymbol{\theta})^T] \geq \mathbf{J}(\boldsymbol{\theta})^{-1} \tag{5.24}$$

where $\hat{\boldsymbol{\theta}}$ denotes to estimated WCE location and $\boldsymbol{\theta}$ denotes the actual WCE location as given in (13). $\mathbf{J}(\boldsymbol{\theta})$ is the Fisher information matrix (FIM) given as

$$\mathbf{J}(\boldsymbol{\theta}) = \mathbf{E}_{\hat{\boldsymbol{r}}, \hat{\boldsymbol{d}}, \hat{\psi}, \hat{\phi}}[-\Delta_{\boldsymbol{\theta}}^{\boldsymbol{\theta}} \ln p(\hat{\boldsymbol{r}}, \hat{\boldsymbol{d}}, \hat{\psi}, \hat{\phi}, \hat{\boldsymbol{\theta}})] \tag{5.25}$$

Denote the overall state information as $\boldsymbol{\theta}_{0:k} = [\boldsymbol{\theta}_0^T, ..., \boldsymbol{\theta}_k^T]$, the dimension of $\mathbf{J}(\boldsymbol{\theta}_{0:k})$ will increases to $mk \times mk$ at kth step (m denotes the dimension of localization system. For the 3D hybrid localization in this study, $m = 3$.), and the computational cost of matrix inversion is not affordable. As an alternative, it is found that the posterior information for $(k+1)$th step can be calculated from existing knowledge of kth step in a recursive manner. Let $\mathbf{J}_k$ be the bottom-right $m \times m$ block of $[\mathbf{J}(\boldsymbol{\theta}_{0:k})]^{-1}$, then the lower bound on the RMSE of WCE localization at step k can be therefore calculated by $\boldsymbol{\Theta}_k = \sqrt{\mathrm{Tr}\{\mathbf{J}_k^{-1}\}}$.

To calculate the FIM at kth step $\mathbf{J}(\boldsymbol{\theta}_{0:k})$, we define $p_k = p(\hat{\boldsymbol{r}}_{0:k}, \hat{\boldsymbol{d}}_{0:k}, \hat{\boldsymbol{\psi}}_{0:k}, \hat{\boldsymbol{\phi}}_{0:k}, \hat{\boldsymbol{\theta}}_{0:k})$ where $\hat{\boldsymbol{r}}_{0:k} = [\hat{\boldsymbol{r}}_0^T, ..., \hat{\boldsymbol{r}}_0^T]$, $\hat{\boldsymbol{d}}_{0:k} = [\hat{\boldsymbol{d}}_0^T, ..., \hat{\boldsymbol{d}}_0^T]$, $\hat{\boldsymbol{\psi}}_{0:k} = [\hat{\boldsymbol{\psi}}_0^T ..., \hat{\boldsymbol{\psi}}_0^T]$, $\hat{\boldsymbol{\phi}}_{0:k} = [\hat{\boldsymbol{\phi}}_0^T, ..., \hat{\boldsymbol{\phi}}_0^T]$ and $\hat{\boldsymbol{\theta}}_{0:k} = [\hat{\boldsymbol{\theta}}_0^T, ..., \hat{\boldsymbol{\theta}}_0^T]$. Then $\mathbf{J}(\boldsymbol{\theta}_{0:k})$ can be given as

$$\begin{aligned}\mathbf{J}(\boldsymbol{\theta}_{0:k}) &= \begin{bmatrix} \mathbf{E}(-\Delta^{\boldsymbol{\theta}_{0:k-1}}_{\boldsymbol{\theta}_{0:k-1}} \ln p_k) & \mathbf{E}(-\Delta^{\boldsymbol{\theta}_k}_{\boldsymbol{\theta}_{0:k-1}} \ln p_k) \\ \mathbf{E}(-\Delta^{\boldsymbol{\theta}_{0:k-1}}_{\boldsymbol{\theta}_k} \ln p_k) & \mathbf{E}(-\Delta^{\boldsymbol{\theta}_k}_{\boldsymbol{\theta}_k} \ln p_k) \end{bmatrix} \\ &= \begin{bmatrix} \boldsymbol{A}_k & \boldsymbol{B}_k \\ \boldsymbol{B}_k^T & \boldsymbol{C}_k \end{bmatrix} \end{aligned} \tag{5.26}$$

and the submatrix $\mathbf{J}_k$ can be obtained by block matrix pseudoinverse as

$$\mathbf{J}_k = \boldsymbol{C}_k - \boldsymbol{B}_k^T \boldsymbol{A}_k^{-1} \boldsymbol{B}_k \tag{5.27}$$

Also, the joint p.d.f for $(k+1)$th step p_{k+1} can be written as

$$\begin{aligned} p_{k+1} = p_k p(\hat{d}_k|\boldsymbol{\theta}_{k+1}, \boldsymbol{\theta}_k) p(\hat{\psi}_k|\boldsymbol{\theta}_{k+1}, \boldsymbol{\theta}_k) p(\hat{\phi}_k|\boldsymbol{\theta}_{k+1}, \boldsymbol{\theta}_k) \\ p(\hat{\boldsymbol{r}}_{k+1}|\boldsymbol{\theta}_{k+1}) \end{aligned} \tag{5.28}$$

With p_{k+1}, the FIM at $(k+1)$th step $\mathbf{J}(\boldsymbol{\theta}_{0:k+1})$ can be calculat- ed with the same

approach as

$$\mathbf{J}(\boldsymbol{\theta}_{0:k+1}) = \left[\begin{array}{cc|c} \boldsymbol{A}_k & \boldsymbol{B}_k & \mathbf{0} \\ \boldsymbol{B}_k^T & \boldsymbol{C}_k + \boldsymbol{H}_k^{11} & \boldsymbol{H}_k^{12} \\ \hline \mathbf{0} & \boldsymbol{H}_k^{12} & \boldsymbol{\mathcal{P}}_{k+1} + \boldsymbol{H}_k^{22} \end{array}\right] \tag{5.29}$$

where $\mathbf{0}$ is zero matrices with proper dimension. $\boldsymbol{H}_k^{11}$, $\boldsymbol{H}_k^{12}$, $\boldsymbol{H}_k^{21}$ and $\boldsymbol{H}_k^{22}$ carries the posterior information from the difference between $(k+1)$th and kth step, which is referred to as the knowledge of step length, heading and elevation measurements. They can be written as

$$\boldsymbol{H}_k^{11} = \mathbf{E}_{\hat{\boldsymbol{d}},\hat{\boldsymbol{\psi}},\hat{\boldsymbol{\phi}}}[-\Delta_{\boldsymbol{\theta}_k}^{\boldsymbol{\theta}_k} \ln p(\hat{d}_k|\boldsymbol{\theta}_{k+1},\boldsymbol{\theta}_k) p(\hat{\psi}_k|\boldsymbol{\theta}_{k+1},\boldsymbol{\theta}_k)$$

$$p(\hat{\phi}_k|\boldsymbol{\theta}_{k+1},\boldsymbol{\theta}_k)] \tag{5.30}$$

$$\boldsymbol{H}_k^{12} = \mathbf{E}_{\hat{\boldsymbol{d}},\hat{\boldsymbol{\psi}},\hat{\boldsymbol{\phi}}}[-\Delta_{\boldsymbol{\theta}_k}^{\boldsymbol{\theta}_{k+1}} \ln p(\hat{d}_k|\boldsymbol{\theta}_{k+1},\boldsymbol{\theta}_k) p(\hat{\psi}_k|\boldsymbol{\theta}_{k+1},\boldsymbol{\theta}_k)$$

$$p(\hat{\phi}_k|\boldsymbol{\theta}_{k+1},\boldsymbol{\theta}_k)] \tag{5.31}$$

$$\boldsymbol{H}_k^{21} = \mathbf{E}_{\hat{\boldsymbol{d}},\hat{\boldsymbol{\psi}},\hat{\boldsymbol{\phi}}}[-\Delta_{\boldsymbol{\theta}_{k+1}}^{\boldsymbol{\theta}_k} \ln p(\hat{d}_k|\boldsymbol{\theta}_{k+1},\boldsymbol{\theta}_k) p(\hat{\psi}_k|\boldsymbol{\theta}_{k+1},\boldsymbol{\theta}_k)$$

$$p(\hat{\phi}_k|\boldsymbol{\theta}_{k+1},\boldsymbol{\theta}_k)] = [\boldsymbol{H}_k^{12}]^T \tag{5.32}$$

$$\boldsymbol{H}_k^{22} = \mathbf{E}_{\hat{\boldsymbol{d}},\hat{\boldsymbol{\psi}},\hat{\boldsymbol{\phi}}}[-\Delta_{\boldsymbol{\theta}_{k+1}}^{\boldsymbol{\theta}_{k+1}} \ln p(\hat{d}_k|\boldsymbol{\theta}_{k+1},\boldsymbol{\theta}_k) p(\hat{\psi}_k|\boldsymbol{\theta}_{k+1},\boldsymbol{\theta}_k)$$

$$p(\hat{\phi}_k|\boldsymbol{\theta}_{k+1},\boldsymbol{\theta}_k)] \tag{5.33}$$

Note that $\boldsymbol{\mathcal{P}}_{k+1}$ denotes to the knowledge of range-based RF localization for WCE, which is given as

$$\boldsymbol{\mathcal{P}}_{k+1} = \mathbf{E}_{\hat{\boldsymbol{r}}}[-\Delta^{\boldsymbol{\theta}_{k+1}}_{\boldsymbol{\theta}_{k+1}} \ln p(\hat{r}_{k+1}|\boldsymbol{\theta}_{k+1})] \tag{5.34}$$

The knowledge of RF-based location estimation can be also derived from the inaccuracy of RF-based range estimation in (7) and (9) as $\boldsymbol{\mathcal{P}}_k = \boldsymbol{\mathcal{G}}_k^T \boldsymbol{\Lambda}_k^{-1} \boldsymbol{\mathcal{G}}_k$ where $\boldsymbol{\mathcal{G}}_k = \boldsymbol{\nabla}_k^T \otimes \boldsymbol{l}_k$ and the diagonal matrix $\boldsymbol{\Lambda}_k = \text{diag}\{\lambda_{k,1}, ..., \lambda_{k,N}\}$ is introduced to collect the variance of pair-wise range estimates with different on-body receivers at the kth step. Note that $\boldsymbol{l}_k = [l_{k,1}, ..., l_{k,N}]$ denotes to the vector of actual distance between WCE and each on-body receiver, $\lambda_{k,n}$ denotes to the variance of range estimate between WCE and nth on-body receiver. Both of the definitions have mentioned in previous sections.

With the FIM for entire $(k+1)$ steps $\mathbf{J}(\boldsymbol{\theta}_{0:k+1})$ in (17), the posterior information submatrix for estimating $\boldsymbol{\theta}_{k+1}$ reads

$$\begin{aligned}\mathbf{J}_{k+1} &= \boldsymbol{\mathcal{P}}_{k+1} + \boldsymbol{H}_k^{22} - \begin{bmatrix} \mathbf{0} & \boldsymbol{H}_k^{21} \end{bmatrix} \begin{bmatrix} \boldsymbol{A}_k & \boldsymbol{B}_k \\ \boldsymbol{B}_k^T & \boldsymbol{C}_k + \boldsymbol{H}_k^{11} \end{bmatrix}^{-1} \begin{bmatrix} \mathbf{0} \\ \boldsymbol{H}_k^{12} \end{bmatrix} \\ &= \boldsymbol{\mathcal{P}}_{k+1} + \boldsymbol{H}_k^{22} - \boldsymbol{H}_k^{21} (\mathbf{J}_k + \boldsymbol{H}_k^{11})^{-1} \boldsymbol{H}_k^{12} \end{aligned} \tag{5.35}$$

Since the noises of step length, heading and elevation measurements e_k, u_k and v_k are modeled as zero-mean Gaussian random variables, $\boldsymbol{H}_k^{11}$, $\boldsymbol{H}_k^{12}$ and $\boldsymbol{H}_k^{22}$ can be calculated as [Tre68]

$$\boldsymbol{H}_k^{11} = -\boldsymbol{H}_k^{12} = \boldsymbol{H}_k^{22} = \boldsymbol{\mathcal{Q}}_k \tag{5.36}$$

where

$$\boldsymbol{\mathcal{Q}}_k = \frac{\boldsymbol{\mathcal{J}}_{\hat{d}}(\psi_k, \phi_k)}{\sigma_k^2} + \frac{\boldsymbol{\mathcal{J}}_{\hat{\psi}}(\psi_k, \phi_k)}{\epsilon_k^2 \sin^2(\phi) d^2} + \frac{\boldsymbol{\mathcal{J}}_{\hat{\phi}}(\psi_k, \phi_k)}{\xi_k^2 d^2} \tag{5.37}$$

Note that $\boldsymbol{\mathcal{J}}_{\text{a}}(\text{b})$ denotes the numerator of Jacobian matrix, which can be written

as

$$\boldsymbol{\mathcal{J}}_{\hat{d}}(\psi_k, \phi_k) =$$

$$\begin{bmatrix} \cos^2\psi\sin^2\phi & \sin\psi\cos\psi\sin^2\phi & \cos\psi\sin\phi\cos\phi \\ \sin\psi\cos\psi\sin^2\phi & \sin^2\psi\sin^2\phi & \sin\psi\sin\phi\cos\phi \\ \cos\psi\sin\phi\cos\phi & \sin\psi\sin\phi\cos\phi & \cos^2\phi \end{bmatrix} \tag{5.38}$$

$$\boldsymbol{\mathcal{J}}_{\hat{\psi}}(\psi_k, \phi_k) =$$

$$\begin{bmatrix} \sin^2\psi & -\sin\psi\cos\psi & 0 \\ -\sin\psi\cos\psi & \cos^2\psi & 0 \\ 0 & 0 & 0 \end{bmatrix} \tag{5.39}$$

$$\boldsymbol{\mathcal{J}}_{\hat{\phi}}(\psi_k, \phi_k) =$$

$$\begin{bmatrix} \cos^2\psi\cos^2\phi & \sin\psi\cos\psi\cos^2\phi & -\cos\psi\sin\phi\cos\phi \\ \sin\psi\cos\psi\cos^2\phi & \sin^2\cos^2\phi & -\sin\psi\sin\phi\cos\phi \\ -\cos\psi\sin\phi\cos\phi & -\sin\psi\sin\phi\cos\phi & \sin^2\phi \end{bmatrix} \tag{5.40}$$

Therefore, the posterior information submatrix $\mathbf{J}_{k+1}$ for estimating the WCE's location $\boldsymbol{\theta}_{k+1}$ can be recursively calculated by

$$\mathbf{J}_{k+1} = \boldsymbol{\mathcal{P}}_{k+1} + \boldsymbol{\mathcal{Q}}_k - \boldsymbol{\mathcal{Q}}_k(\mathbf{J}_k + \boldsymbol{\mathcal{Q}}_k)^{-1}\boldsymbol{\mathcal{Q}}_k \tag{5.41}$$

Applying Sherman Morrison Woodbury formula with identity matrices of proper

dimension, it can be simplified as

$$\mathbf{J}_{k+1} = \boldsymbol{\mathcal{P}}_{k+1} + (\boldsymbol{\mathcal{Q}}_k^{-1} + \mathbf{J}_k^{-1})^{-1} \tag{5.42}$$

where $\boldsymbol{\mathcal{Q}}_k$ shows the effect of image processing based step, heading and elevation measurements and $\boldsymbol{\mathcal{P}}_{k+1}$ illustrates the effect of RF based location estimation. Note that with the absence of z dimension and vertical elevation measurements $\hat{\boldsymbol{\phi}}$, the above approach can be still apply to 2D general hybrid localization with RF signals and inertial sensing. The inertial based measurement can be equivalent to image processing based estimation in WCE localization.

5.4 Simulations and Numerical Results.

In this section, the hybrid localization approach has been implemented and the PCRLB has been calculated to evaluate the accuracy of the proposed approach. Even though there are elegant expressions to recursively calculate the FIM, the expressions in equation (30)$\sim$(33) usually do not have analytical close-form solution. In order to deal with that, we employ the *monte carlo* approach to convert those continuous integrals into discrete summations, and finally work out the PCRLB.

The Root-Mean-Square (RMS) of PCRLB is given by $\frac{1}{\boldsymbol{\mathcal{I}}} \sum_{i=1}^{\boldsymbol{\mathcal{I}}} \boldsymbol{\Theta}_k^i$, where $\boldsymbol{\Theta}_k^i$ is the PCRLB on the Root-Mean-Square Error (RMSE) of WCE at step k in the ith *monte carlo* trial. i denotes the index for *monte carlo* trials and $\boldsymbol{\mathcal{I}}$ is the total *monte carlo* trial number, which is selected as 2000 in this work. Note that the trajectory for PCRLB calculation is generated from the 3D path of small intestine as shown in Fig 5.4. For RSS based location estimation, we regard the wireless channel between WCE and on-body receiver as deep tissue propagation channel model if $\hat{l}_{k,n} \geq 10$cm and let $\alpha = 4.26$, $\zeta = 7.85$dB. Otherwise, we take the body

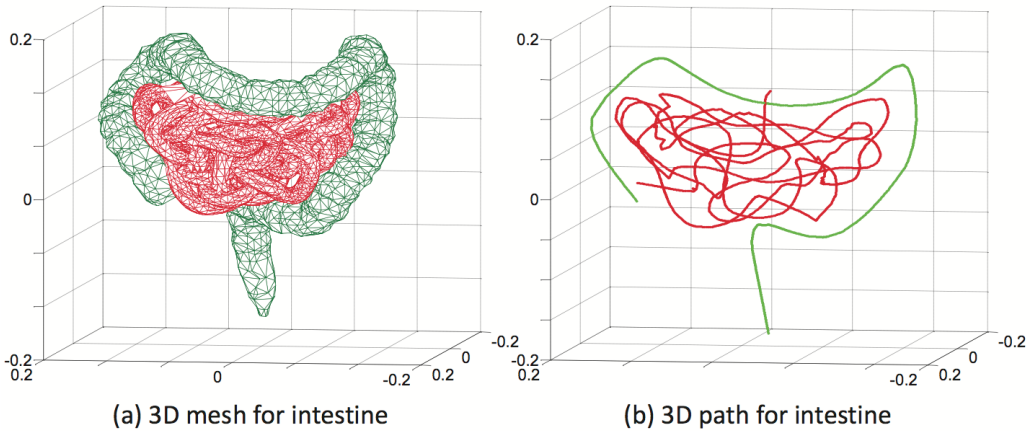

Figure 5.4: Trajectory of WCE inside human GI tract. (a) 3D mesh for human intestine; (b) 3D path for human intestine obtained by skeletonization of 3D mesh.

surface channel model, which is $\alpha = 4.22$ and $\zeta = 6.81$dB. For TOA based approach, the signal propagation velocity inside human small intestine is given as $c/\sqrt{\varepsilon_{\text{ave}}} = 2.14 \times 10^8$m/s. Note that for each *monte carlo* trial, we randomly select the initial location for PCRLB calculation in order to get a fair average of entire small intestine.

5.4.1 Performance of the WCE Hybrid Localization Approach.

The proposed WCE hybrid localization approach has been implemented together with the conventional image processing based WCE tracking and conventional RF based WCE localization. The restrictions on *vivo* experiments inside human body make it very challenging to validate these approaches. In this work, a pre-defined virtual test-bed has been selected to provide the ground truth [MBP13]. Note that the test-bed shares the same size and shape of small intestine and the interior surface

is rendered with a clinical WCE video[2].

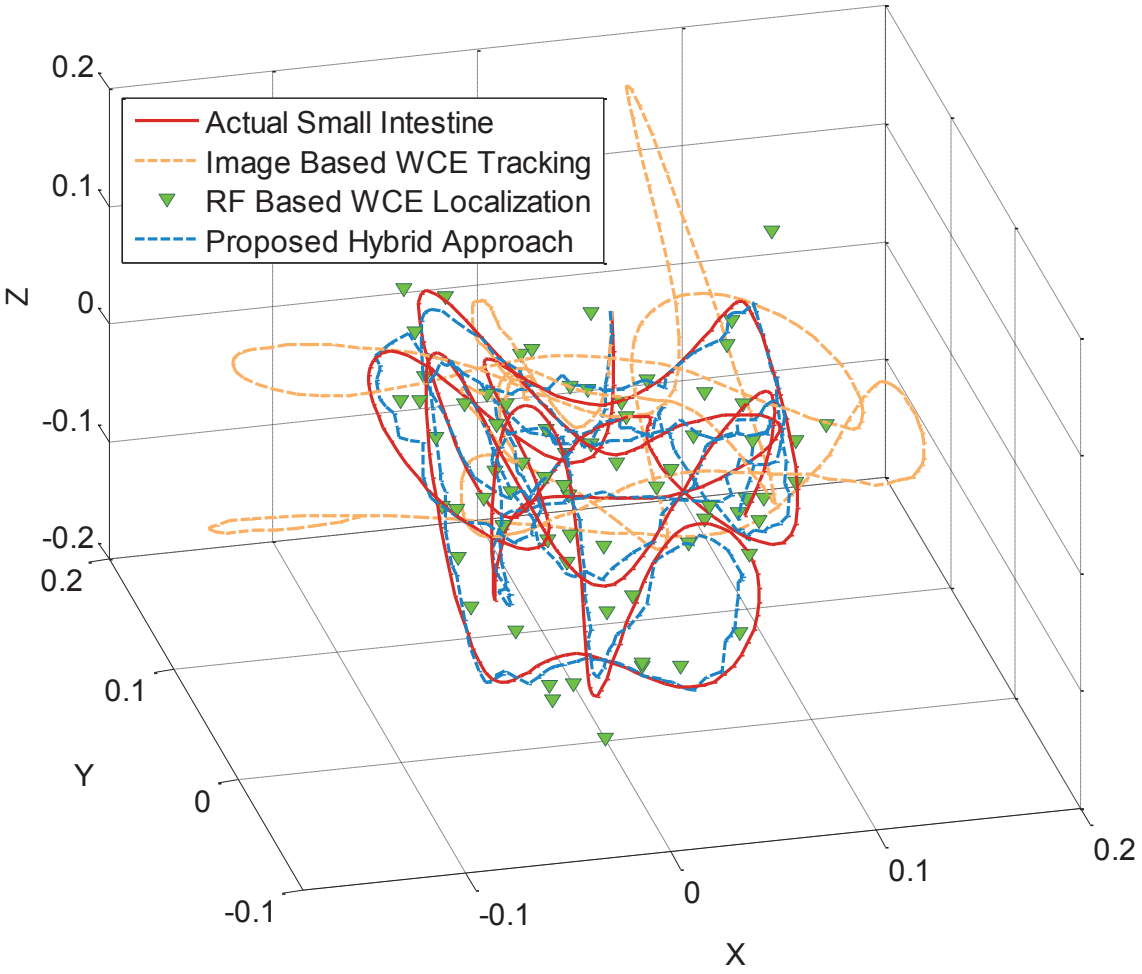

Figure 5.5: Typical output of the proposed WCE hybrid localization approach. The unit is in meter for all axis. Note that for the sake of clarity, the RF based location estimation has been plotted in a discrete manner.

Fig 5.5 shows the output of a single trial of the proposed hybrid localization approach. We select 32 on-body receivers with 16 of them uniformly distributed on the front of human body within a 0.4m×0.4m area[3] and another 16 mirroring on the

[2]Since this study focuses on the system level of WCE hybrid localization, we will not further expand the details of test-bed design. Further description of the test-bed can be found in [MBP13]

[3]Explanation of the deployment can be also found in the following sections and the selected on-body sensor deployment can be found in Fig 5.5.

rear of human body. It is clear that image processing based WCE tracking suffers severe drift from accumulated estimation errors. Apart from that, scatter plot of RF based WCE localization results is also displayed in Fig 5.5. It does not have the drifting issue but the localization accuracy is not satisfactory. The proposed hybrid localization algorithm outperforms both above mentioned conventional approaches and the general trend of the proposed algorithm achieves a highly agreement with the ground truth.

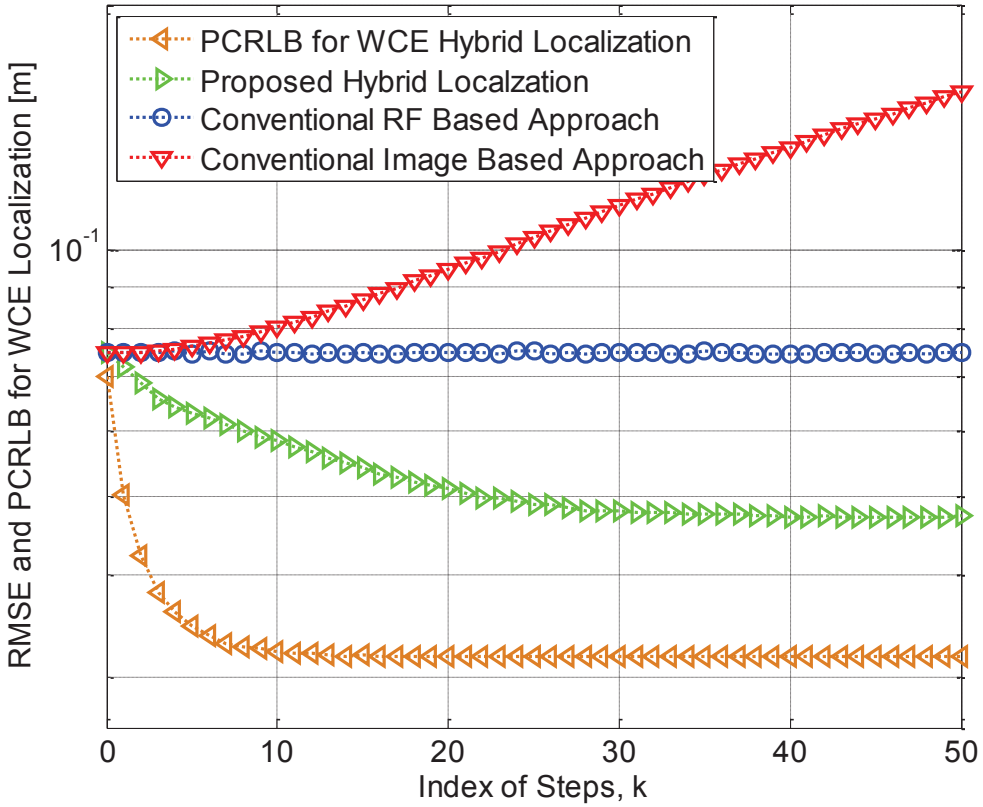

Figure 5.6: Performance evaluation of the proposed WCE hybrid localization approach. The hybrid approach starts from arbitrary place and use RF measurement for initialization.

2000 runs of *monte carlo* simulation has been also applied to the proposed hybrid approach to evaluate its localization accuracy. Fig 5.6 illustrates the localization RMSE for image processing based, RF based and hybrid approaches as well as the

PCRLB for hybrid localization. Major observation includes (1) The drifting issue of image processing based WCE tracking appears after the beginning 5 steps and it soon becomes severe enough to make the tracking result no longer reliable. (2) The hybrid approach stabilize at the accuracy of 4.7cm with the selected scenario, which is much more accurate than the 7.4cm accuracy of conventional RF localization. (3) The PCRLB for the proposed hybrid approach stabilize at the accuracy of 3.2cm, showing that the proposed algorithm can be potentially improved. Note that all above analysis is for RSS based ranging technique. TOA based approach results in identical trend but better accuracy and is carefully investigated in following sections.

5.4.2 Effect of Step Length, Heading and Elevation.

In this section, we study how the image processing based estimation accuracy affects the performance of proposed WCE hybrid localization approach using the PCRLB. The experimental scenario is given as follows. Inaccuracy on step length measurement are considered to be proportion of the actually step length d as $\sigma_k = \eta d_k$, heading and elevation measurements are considered to have identical variance as $\epsilon_k = \xi_k = \omega$. PCRLB $\mathbf{J}_k$, $\mathbf{J}_{k+1}$ are calculated with η varying from 10% to 30% and ω varying from 10^o to 30^o to illustrate the minimum achievable RMSE $\mathbf{\Theta}_k$ in hybrid WCE localization. CRLB for pure RF based localization $\boldsymbol{\mathcal{P}}_k$ has been also calculated to provide a comparison against PCRLB. Note that to isolate the effect of combined RF and image processing based measurement, 8 on-body receivers are fixed at $[D, D, D]$, $[D, -D, D]$, $[D, D, -D]$, $[D, -D, -D]$, $[-D, D, D]$, $[-D, -D, D]$, $[-D, D, -D]$ and $[-D, -D, -D]$(as shown in Fig 5.9), where $D = 0.2$m is selected to fit in the size of general human torso and coordinate space is originated at the geometric center of small intestine.

Simulation results on PCRLB with various η and ω have been plotted in Fig

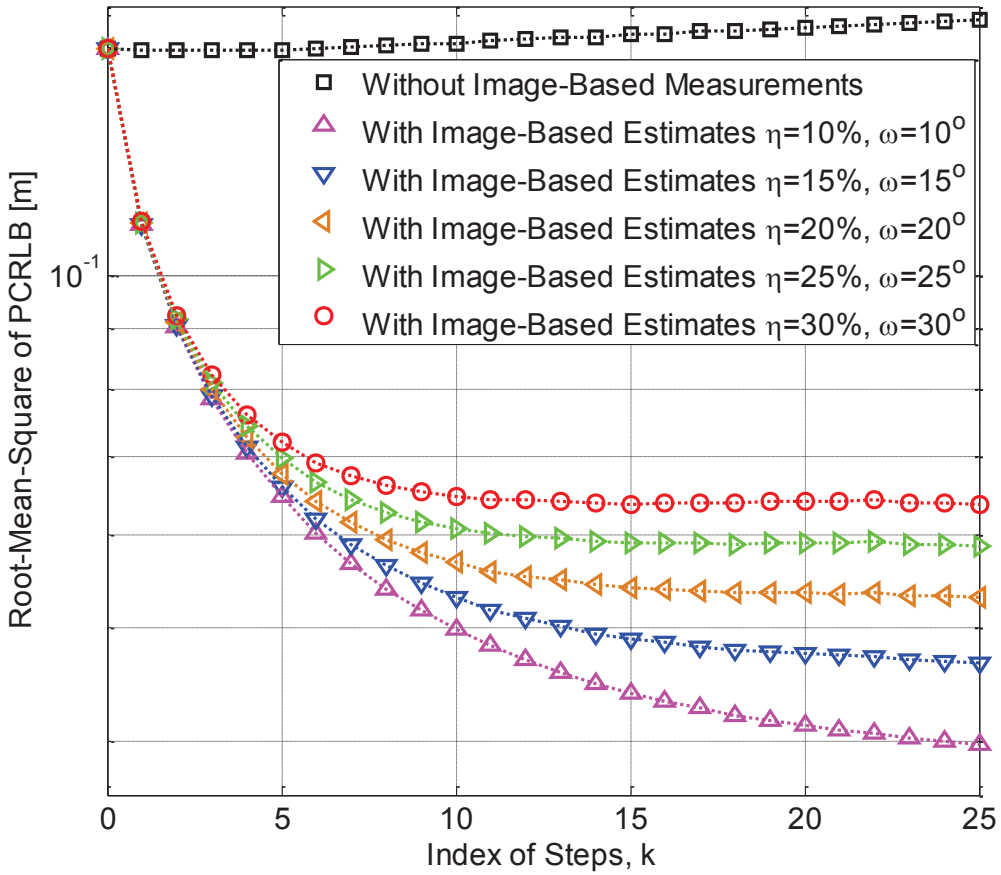

Figure 5.7: PCRLB of the proposed WCE hybrid localization approach as a function of step index. (a) Using RSS as ranging metric.

5.7 and Fig 5.8, in which the CRLB with the absence of image processing based estimates is also provided for comparison. Fig 5.7 shows the PCRLB when RSS based ranging technique is selected. It can be seen that (1) The knowledge of step length, heading and elevation measurements significantly increases the accuracy of WCE localization. With the RMSE for conventional RF based localization dwelling at around 12.5cm, the PCRLB for hybrid localization drops to 4.4cm even in the worst case with $\eta = 30\%$ and $\omega = 30^o$. (2) The hybrid localization accuracy is directly proportional with the accuracy of step length, heading and elevation measurements, that is, with the increment of η and ω, obvious decrement of RMSE can

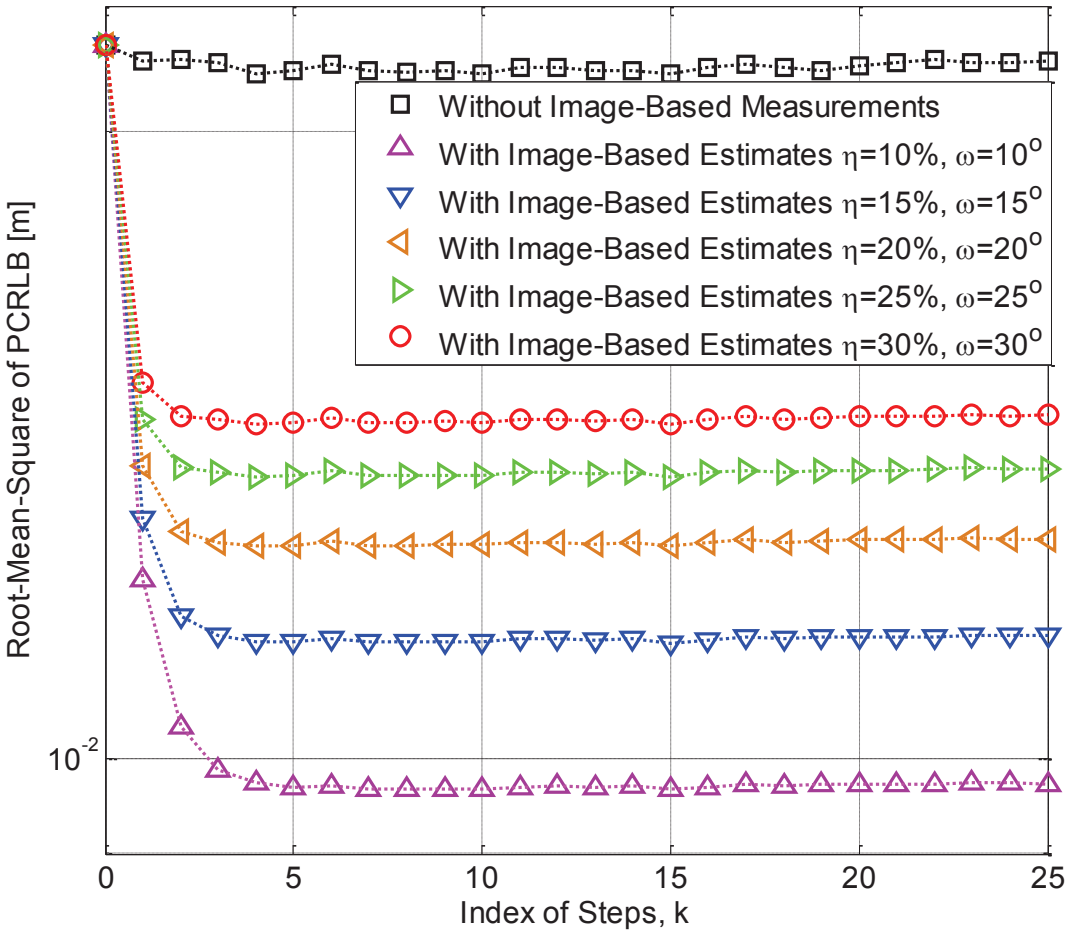

Figure 5.8: PCRLB of the proposed WCE hybrid localization approach as a function of step index. (b) Using TOA as ranging metric.

be seen from the PCRLB plot. (3) PCRLB for hybrid WCE localization stabilizes after certain steps regardless of the beginning point and following trajectory. With better posterior knowledge of step length and headings, the PCRLB stabilize slower. However, with poor step length, heading and elevation measurements, the hybrid localization approach reaches the maximum achievable performance very fast. For the best case with $\eta = 10\%$ and $\omega = 10^o$, it takes 25 steps for PCRLB to stabilize at 2.5cm, while for the worst case with $\eta = 30\%$ and $\omega = 30^o$ it stabilize in only 10 steps at 4.4cm.

Fig 5.8 shows the PCRLB when TOA based ranging technique is selected. UWB signal with flat spectrum over the channel from 370MHz to 630MHz with a SNR of 30dB has been employed for simulation [YKN10]. Compared with the RSS based ranging technique, couple of differences can be found as (1) The hybrid localization with TOA ranging technique has a much better accuracy compared with RSS ranging technique. It achieves 2.16cm of accuracy when there is no support from image based knowledge of WCE location information, 1.46cm in the worst case with $\eta = 30\%$ and $\omega = 30^o$ and 0.97cm in the best case with $\eta = 10\%$ and $\omega = 10^o$. (2) With TOA based range estimate, the improvement obtained from the image based knowledge is less than that with RSS based ranging technique. In the worst case with $\eta = 30\%$ and $\omega = 30^o$, hybrid localization with RSS ranging obtained 8.1cm accuracy improvement (from 12.5cm to 4.4cm). However, hybrid localization with TOA ranging only has 0.76cm of improvement (from 2.16cm to 1.4cm). Such observation is intuitive due to the fact that TOA based range estimate results in better RF based location estimation so that image based knowledge gets less weighted in the calculation of Kalman Gain. (3) Hybrid localization with TOA ranging technique stabilize much faster than that of RSS ranging technique. It stabilizes in 3 steps in the worst case and 5 steps in the best case. That phenomenon also shows that the support from image based knowledge is limited when the RF based location estimation is extraordinarily accurate.

5.4.3 Effect of On-Body Receiver Numbers.

To analyze the impact of on-body RF receiver number on the RMSE for RF and image processing based hybrid WCE localization, the previously used *monte carlo* simulation has been repeated with different receiver numbers. To maintain the symmetry of on-body sensor placement, we investigate receiver numbers of 8(2x2x2),

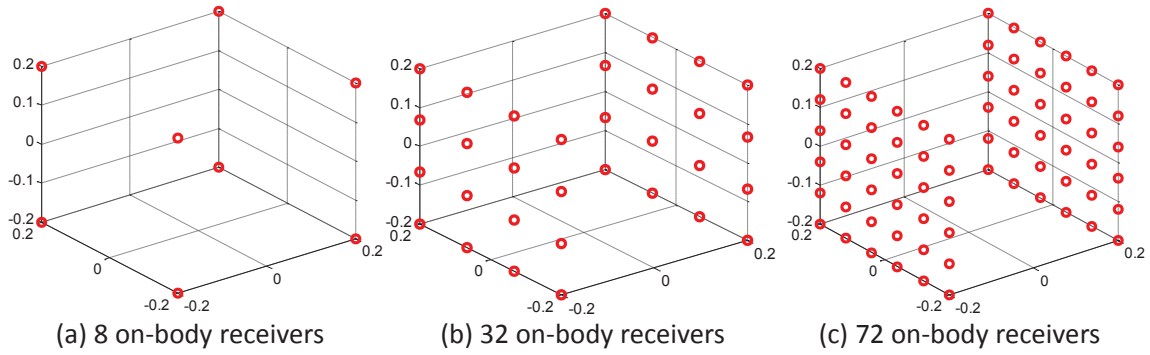

Figure 5.9: Actual on-body receiver placement. The unit is in meter for all axis. (a) Totally 8 on-body receivers, 4(2x2) in the front and 4 mirroring on the back; (b) Totally 32 on-body receivers, 16(4x4) in the front and 16 mirroring on the back; (c) Totally 72 on-body receivers, 36(6x6) in the front and 36 mirroring on the back.

18(3x3x2), 32(4x4x2), 50(5x5x2) and 72(6x6x2). 8-receiver, 32-receiver and 72-receiver cases are depicted in Fig 5.9. Plots of 18-receiver and 50-receiver cases have been waived for the purpose of simplicity. Inaccuracy for step length, heading and elevation measurements are fixed as $\eta = 20\%$, $\epsilon = 20^o$ and $\xi = 20^o$. Note that, half of on-body sensors are uniformly distributed on the front plane of the jacket that patient wears and the other half on the rear plane of the jacket. Both planes have fixed size of 0.4x0.4m.

The simulation result of hybrid localization with RSS and TOA ranging has been plotted in Fig 5.10 and Fig 5.11, respectively. Clearly, Hybrid localization approaches with either RSS ranging or TOA ranging shares identical trend. Take the RSS based ranging as an example, the effects of on-body sensor number can be seen as (1) The number of on-body receivers has significant influence on the accuracy of both pure RF based and hybrid localization. 8 receivers achieve 12.5cm CRLB for RF based localization and 3.5cm PCRLB for hybrid approach. With 72 receivers, the CRLB for RF based localization drops to 2.8cm and the PCRLB for hybrid approach goes down to 1.8cm. It is clear that the increment of receiver

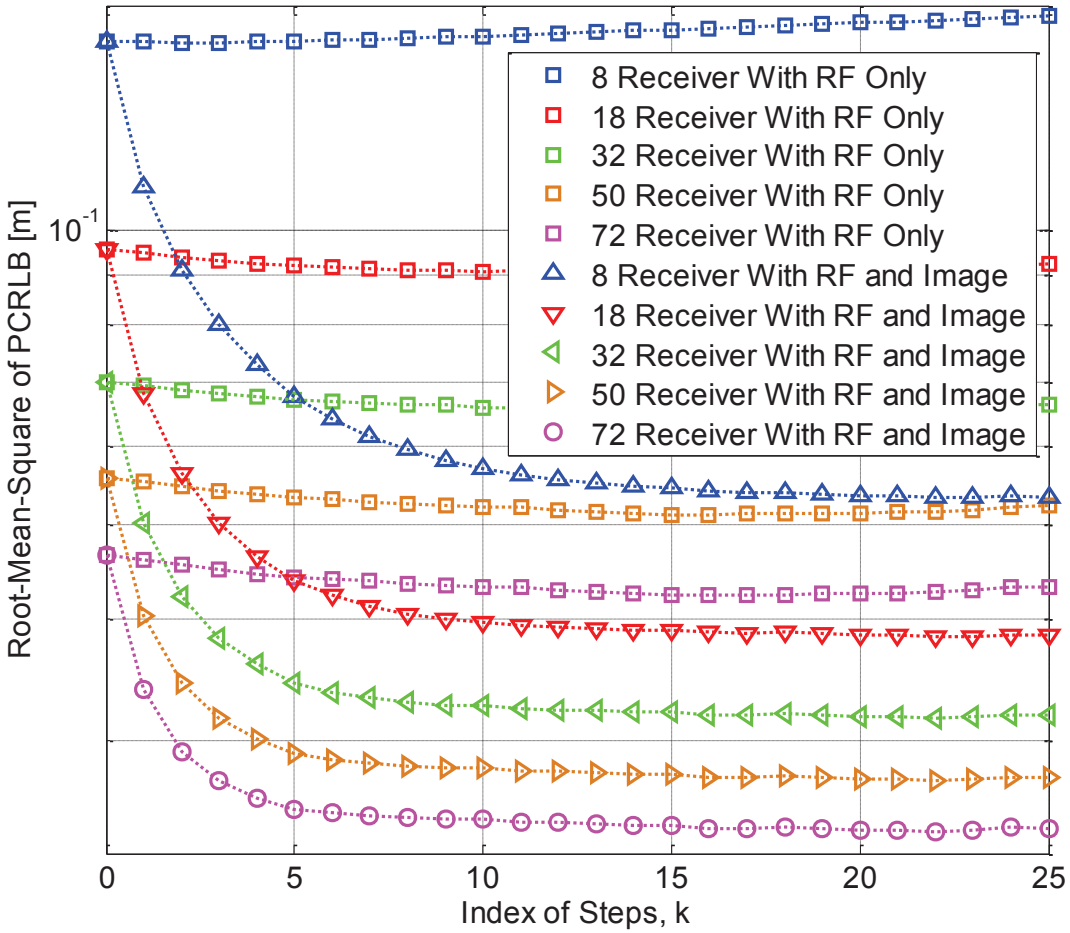

Figure 5.10: PCRLB of the proposed WCE hybrid localization approach with number of on-body receivers varies from [8, 18, 32, 50, 72]. (a) Using RSS as ranging metric.

number significantly improves the performance of both RF based and hybrid WCE localization. (2) The difference of PCRLB between 8-receiver case and 16-receiver case is 1.1cm while the difference between 50-receiver case and 72 receiver case is only 1mm. Both differences indicate that with the receiver number becomes larger, the scale of performance improvement on PCRLB gets smaller. Similar trend can be seen from the CRLB of pure RF based localization. (3) The difference between CRLB and PCRLB for 8-receiver case is around 9cm while for 72-receiver case, this difference is only 0.7cm, meaning that with fewer number of receivers, the hybrid

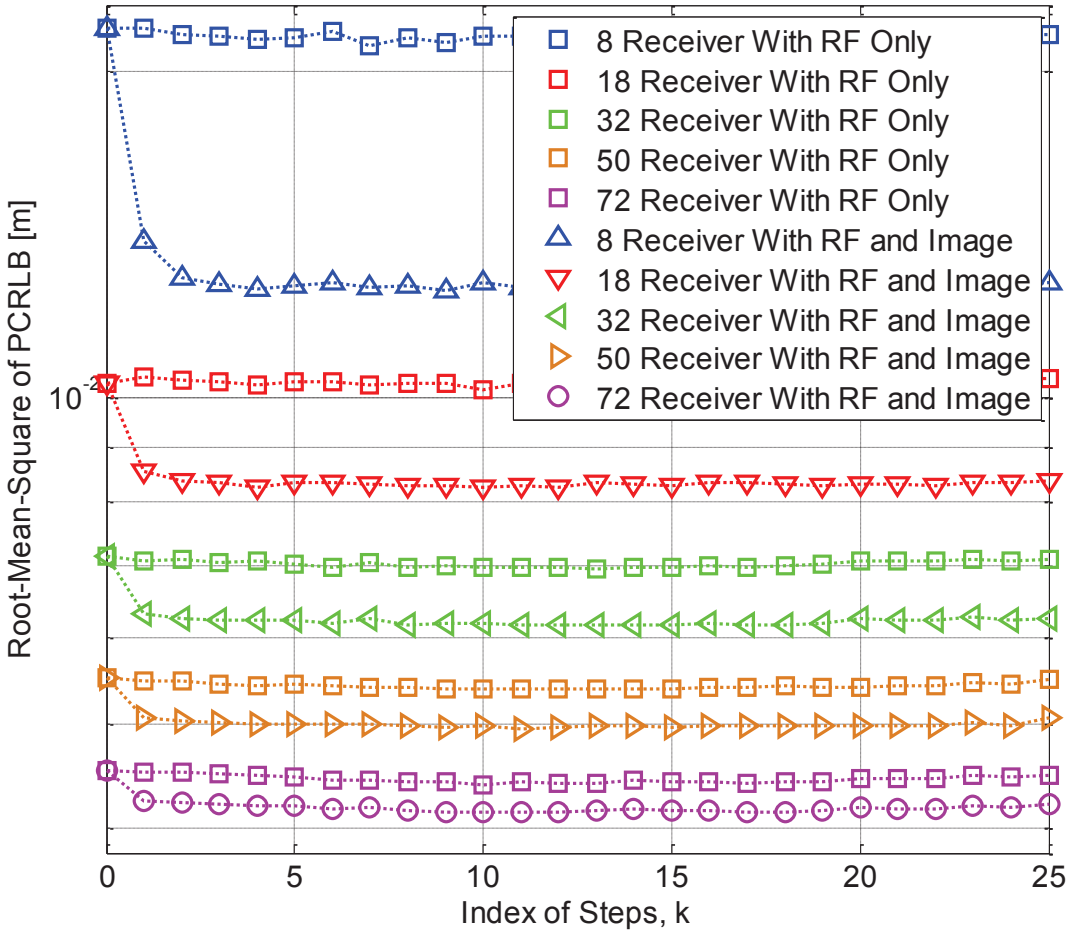

Figure 5.11: PCRLB of the proposed WCE hybrid localization approach with number of on-body receivers varies from [8, 18, 32, 50, 72]. (b) Using TOA as ranging metric.

approach improve the localization accuracy dramatically. However, with enough on-body sensors, the advantage of hybrid WCE localization can be compressed. Note that due to the ultra-high requirement on WCE localization accuracy, the compressed advantage of hybrid approach is still desired. (4) For 8-receiver case, it takes 20 steps for the hybrid WCE localization to stabilize, however, for 50-receiver and 72-receiver cases, it takes only 10 steps to reach stabilization. We can easily draw the conclusion that for larger number of receivers, the hybrid approach stabilizes much faster. Note that all above observation can be also applied to hybrid

localization with TOA ranging and the only two differences are faster stabilization and better localization accuracy.

5.4.4 Effect of System Bandwidth.

It can be seen from Equation (21) that the performance of TOA based ranging is related to both SNR and effective bandwidth β. The SNR is usually determined by the WCE metadata and the background noise of radio propagation inside the human body, but the effective bandwidth β has to be regarded as an aspect of system design and implementation. Apart from the fixed system we employed in previous sections, in this section, we analyze the effect of system effective bandwidth.

The simulation results for the effect of system effective bandwidth have been plotted in Fig 5.12. Note that although the performance of hybrid localization with RSS ranging is not related to the effective bandwidth, we still plot them as a comparison against the hybrid localization with TOA ranging. Major observation from the simulation results is that the RMS of PCRLB has a logarithmic decrement with the logarithmic increment of system effective bandwidth β, indicating that larger effective bandwidth results in better localization performance when TOA ranging is employed. Take the 72 on-body sensor case as an example, the hybrid localization reach the accuracy of 2.4cm when $\beta = 30$MHz and it goes up to 0.37mm when $\beta = 3$GHz. Such accuracy fulfills the requirement of millimeter level localization approach we claimed earlier at the beginning of this study.

It is worth mentioning that the 3GHz effective bandwidth only appears in UWB systems with several GHz of actual bandwidth, and such high bandwidth or high center frequency make it extremely difficult for the signals to propagate through the human body. Apart from that, the communication coverage of such systems can be short as approximately 20cm. Considering the realistic factor, we stop our

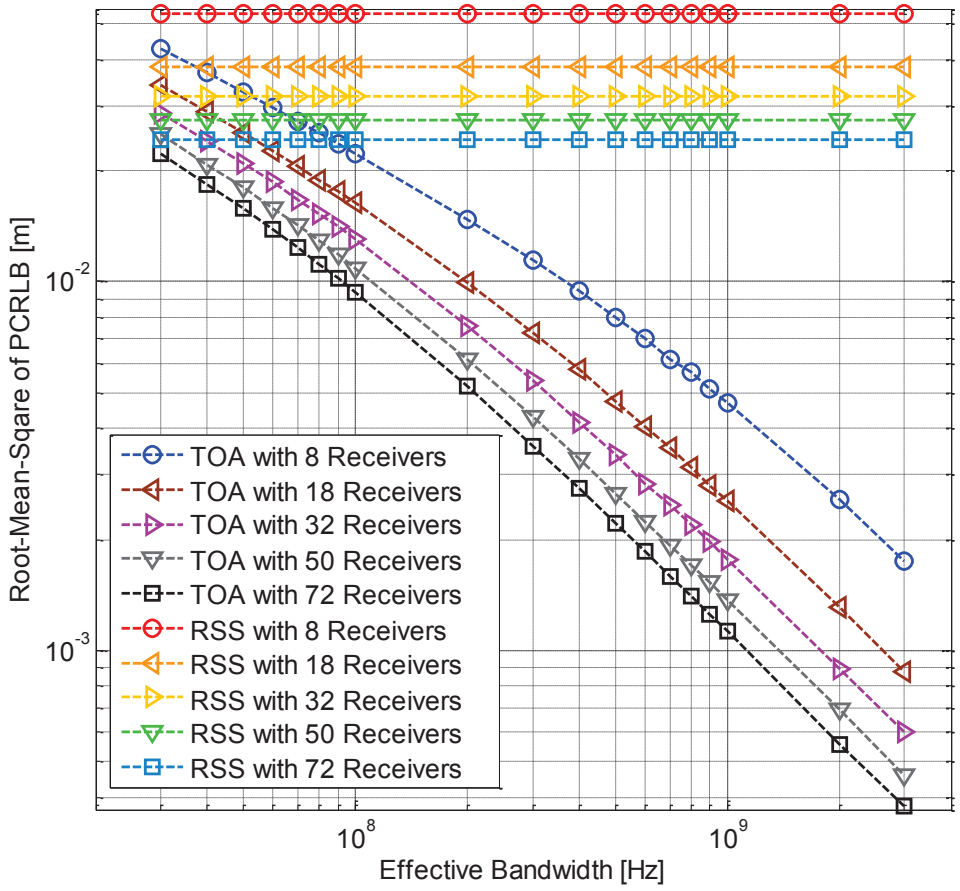

Figure 5.12: Effects of the system effective bandwidth β. performance of hybrid localization with RSS ranging is also plotted for comparison.

exploration at $\beta = 3$GHz, which covers the radio propagation channel introduced in [AK10] when a flat spectrum is used for TOA ranging.

5.4.5 Effect of On-Body RF Receiver Placement.

Different placements for on-body RF receivers are also considered, which potentially represent the RF sensor arrangement in practical applications. Again, we simulate the performance of hybrid localization with both RSS and TOA ranging under the condition of various topologies. The number of on-body sensor has been fixed as 32, still with half of them on the front plane of the jacket and the other half

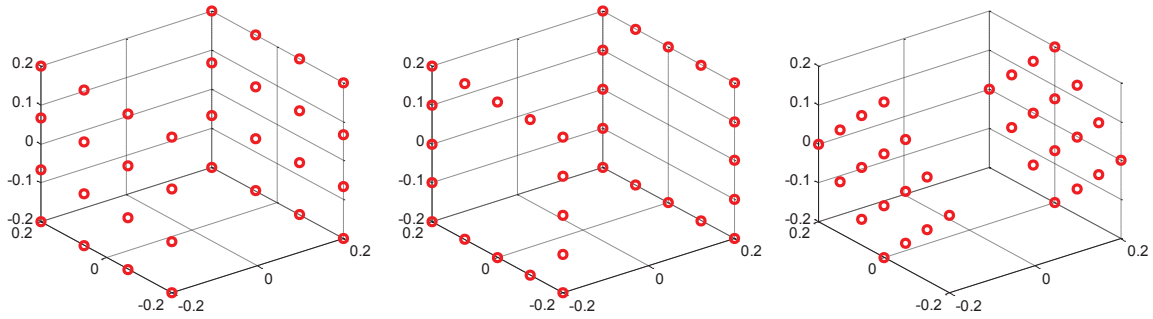

Figure 5.13: Actual on-body receiver placement. The unit is in meter for all axis. (a) Topology1, a parallel line configuration; (b) Topology2, a rectangular border configuration; (c) Topology3, a parallel line configuration with 45^o rotation.

on the rear plane of the jacket. Again, for inaccuracy of posterior information of step length, heading and elevation measurements, we let $\eta = 20\%$, $\epsilon = 20^o$ and $\xi = 20^o$ to isolate the effect of movement tracking accuracy. Note that both planes are again bounded by 0.4x0.4m to fit the general human torso and small intestine. Three distinct topologies have been introduced, namely, (1) Topology1, a parallel line configuration that all RF receivers uniformly distributed on both plane. (2) Topology2, a rectangular configuration that all RF receivers evenly distributed on a rectangular border line on both plane. (3) Topology3, a 45^o rotated parallel line configuration that RF receivers concentrated at the center of both plane. All topologies are depicted in Fig 5.13.

Both pure RF based and hybrid location estimation using RSS ranging has been investigated and results are plotted in Fig 5.14. It is shown that: (1) Comparing CRLB and PCRLB, with the posterior information of step length and heading estimates, the improvement on localization accuracy remains identical for different topologies. (2) The hybrid localization with different topologies shares the same number of steps to stabilize. (3) Topology2 suffers the largest RMSE, followed by

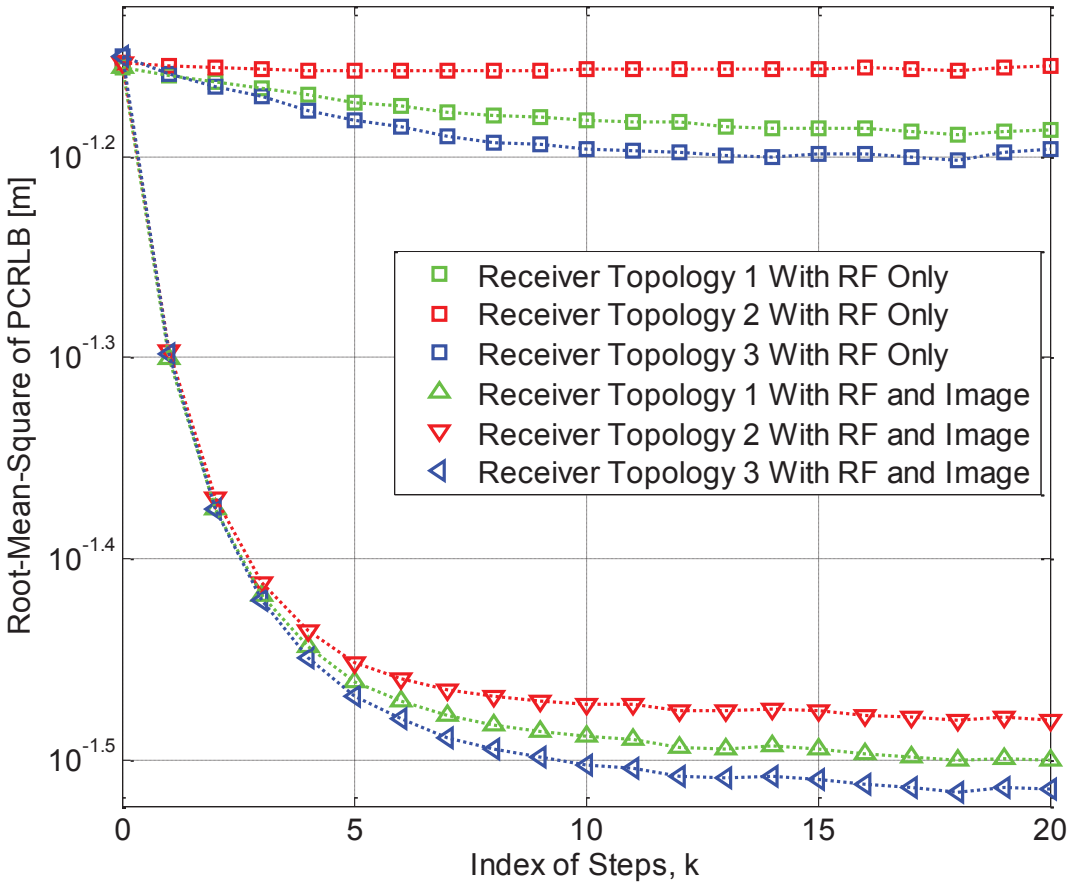

Figure 5.14: Root-mean-square of PCRLB as a function of index of steps. Different receiver topologies are considered including topology 1,2 and 3. Each topology has 32 on-body receivers in total. Both pure RF case and hybrid case are considered.

topology1 with around 1.9mm less RMSE. Topology3 is preferred for its minimum RMSE, which is 1.1mm less than topology2. The hybrid location estimation with TOA ranging shares identical trend results with that of RSS ranging, we do not repetitively display it the for the sake of simplicity.

5.5 Summary.

In this chapter, we investigated the feasibility of implementing a WCE hybrid localization system using real-time image processing based WCE movement tracking

and RF based WCE localization. 3D PCRLB has been derived as the theoretical limits for the proposed approach. With *monte carlo* simulation of the PCRLB, we demonstrated that the proposed approach can achieve millimeter level of localization accuracy inside human body with proper system setup. We observed that with better image processing based movement estimation, more on-body RF receivers, larger system effective bandwidth or better on-body sensor deployment, the performance of the proposed hybrid approach can be further enhanced. Since the image processing based movement estimation shares very similar formulation with inertial based movement tracking, the PCRLB derivation in this study can be also used in regular hybrid indoor localization with inertial sensor and RF signals.

Chapter 6

Conclusion.

In this dissertation, we presented three challenging problems in the field of body area network related precise and accurate localization and motion classification. All three challenging problems can be regarded as emerging fundamental areas for scientific research and engineering developments.

Firstly we worked on the radio propagation channel from body mounted sensors to the external access points and presented a TOA ranging model that takes shadowing effect of human body and the creeping wave phenomenon into consideration. The model was developed from empirical measurement data and it can be used to improve the performance of indoor positioning systems and calculate the theoretical performance bound of such systems.

Secondly we focused on the radio propagation channel between a pair of body mounted sensors and presented a motion detection system that can detect and classifiy multiple frequently appeared human motions. The classification system is firstly designed for first responders who work in dangerous environment and then expanded to elder person and hospital patients. Such system employ RF signal only and avoid the requirements on pre-deployed infrastructure or extra inertial sensors.

Our classification rate can be as high as 92 percent.

Thirdly we investigated the radio propagation channel from in-body micro-robots to body mounted sensors and proposed RF based localization scheme for Wireless Capsule Endoscopy. We calculated the theoretical PCRLB for hybrid WCE localization and proved that given enough bandwidth, milli-meter level of localization accuracy is achievable. With such high accuracy, it is possible to perform 3D reconstruction for the interior of human small intestine.

As one of booming research field, there are much more important body area network related problems remain unsolved. I wish this dissertation can serve as an inspiration to other researchers and encourage more devotion to the area.

Bibliography

[AA07] K. Arshak and F. Adepojum. Adaptive linearized methods for tracking a moving telemetry capsule. *IEEE International Symposium on Industrial Electronics (ISIE)*, 2007.

[AAP09] N. Alsindi, B. Alavi, and K. Pahlavan. Measurement and modeling of ultrawideband toa-based ranging in indoor multipath environments. *IEEE Transactions on Vehicular Technology*, 58(3):1046–1058, 2009.

[AGV08] S.M. Aziz, M. Grcic, and T. Vaithianathan. A real-time tracking system for an endoscopic capsule using multiple magnetic sensors. *Smart Sensors and Sensing Technology*, 20(5):201–218, 2008.

[AK10] X. Liang and A. Khaleghi, R.Chvez-Santiago. On ultra wideband channel modeling for in-body communications. *2010 5th International Symposium on Wireless Pervasive Computing (ISWPC)*, 2010.

[AKKM14] F. Adib, Z. Kabelac, D. Katabi, and R.C. Miller. 3d tracking via body radio reflections. *2014 11th USENIX Symposium on Networked Systems Design and Implementation (NSDI14)*, 2014.

[ALK09] A.W. Astrin, H.B. Li, and R. Kohno. Standardization for body area networks. *IEICE Transaction on Communications*, E92-B(2):366–372, 2009.

[AMSA+11] E. Auvinet, F. Multon, A. Saint-Arnaud, J. Rousseau, and J. Meunier. Fall detection with multiple cameras: An occlusion-resistant method based on 3-d silhouette vertical distribution. *IEEE Transactions on Information Technology in Biomedicine*, 15(2):290–300, 2011.

[AP06] B. Alavi and K. Pahlavan. Modeling of the toa based distance measurement error using uwb indoor radio measurements. *IEEE Communication Letters*, 10(4):275–277, 2006.

[ARZ+13] A. Ariani, S.J. Redmond, Z. Zhang, M.R. Narayanan, and N.H. Lovell. Design of an unobtrusive system for fall detection in multiple occupancy residences. *2013 IEEE 35th Annual International*

Conference of Engineering in Medicine and Biology Society (EMBC), 2013.

[ASSC02] I.F. Akyildiz, W. Su, Y. Sankarasubramaniam, and E. Cayirci. Wireless sensor networks: A survey. *Computer Networks*, 38(1):393422, 2002.

[AY09] A. Alomainy and H. Yang. Modeling and characterization of biotelemetric radio channel from ingested implants considering organ contents. *IEEE Transactions on Antennas and Propagation*, 57(4):999–1005, 2009.

[BI04] L. Bao and S.S. Intille. Activity recognition from user-annotated acceleration data. *Proceeding of Springer Second International Conference*, 2004.

[BKKS09] M. Bessho, N. Koshizuka, S. Kobayashi, and K. Sakamura. Location systems for ubiquitous computing. *Jounal of IEICE*, 92(4):249–255, 2009.

[BLA08] D. Bannach, P. Lukowicz, and O. Amft. Rapid prototyping of activity recognition applications. *IEEE Transactions on Pervasive Computing*, 7(2):22–31, 2008.

[BP12] G. Bao and K. Pahlavan. Motion estimation of the endoscopy capsule using region-based kernal svm classifier. *IEEE International Conference on Electro/Information Technology (EIT)*, 2012.

[BPM15] G. Bao, K. Pahlavan, and L. Mi. Hybrid localization of micro-robotic endoscopic capsule inside small intestine by data fusion of vision and rf sensors. *IEEE Sensors Journal*, 15(5):2669–2678, 2015.

[BRS10] J. Boese, N. Rahn, and B. Sandkamp. Method for determining the position and orientation of an object, especially of a catheter, from two-dimensional x-ray images. *U.S. Patent, 7-801-342*, 2010.

[BYK+12] G. Bao, Y. Ye, U. Khan, X. Zheng, and K. Pahlavan. Modeling of the movement of the endoscopy capsule inside gi tract based on the captured endoscopic images. *2012 9th International Conference on Modeling, Simulation and Visualization Methods (MSV)*, 2012.

[CGV+11] M. Chen, S. Gonzalez, A. Vasilakos, H. Cao, and V. Leung. Body area networks: A survey. *Mobile Networks and Applications*, 16(1):171193, 2011.

[Chr98] J.C. Christopher. A tutorial on support vector machines for pattern recognition. *Data Mining and Knowledge Discovery*, 2(2):121–167, 1998.

[CJ13] W.C. Cheng, , and D.M. Jhan. Triaxial accelerometer-based fall detection method using a self-constructing cascade-adaboost-svm classier. *IEEE Journal of Biomedical and Health Informatics*, 17(2):411–419, 2013.

[CL11] C.C. Chang and C.J. Lin. Libsvm: A library for support vector machines. *ACM Transactions on Intelligent Systems and Technology (TIST)*, 2(3):1–27, 2011.

[CMD11] G. Ciuti, A. Menciassi, and P. Dario. Capsule endoscopy: from current achievements to open challenges. *IEEE Reviews in Biomedical Engineering*, 4(1):59–72, 2011.

[CMP+13] J. Cabestany, J.M. Moreno, C. Perez, A. Sama, A. Catala, A.R. Molinero, and M. Arnal. Fate: One step towards an automatic aging people fall detection service. *2013 IEEE 20th International Conference on Mixed Design of Integrated Circuits and Systems (MIXDES)*, 2013.

[CSSK+13] R. Chaves-Santiago, K. Sayrafian, A. Khaleghi, K. Takizawa, J. Wang, I. Balasingham, and H. Li. Propagation models for ieee 802.15.6 standardization of implant communication in body area networks. *IEEE Communications Magazine*, 51(8):80–87, 2013.

[CV95] C. Cortes and V. Vapnik. Support vector network. *ACM Machine Learning*, 20(3):273–297, 1995.

[DC13] A. Dubois and F. Charpillet. Human activities recognition with rgb-depth camera using hmm. *2013 IEEE 35th Annual International Conference of Engineering in Medicine and Biology Society (EMBC)*, 2013.

[FC08] D.O. Faigel and D.R. Cave. Capsule endoscopy. 2008.

[FDD+06] A. Fort, C. Desset, P. Doncker, P. Wambacq, and L.V. Biesen. An ultra-wideband body area propagation channel modelfrom statistics to implementation. *IEEE Transactions on Microwave Theory and Techniques*, 54(4):1820–1826, 2006.

[FFRV05] C. Flora, M. Ficco, S. Russo, and V. Vecchio. Indoor and outdoor location based services for portable wireless devices. *25th IEEE International Conference on Distributed Computing Systems Workshops*, 2005.

[FM11] Y. Fan and M.Q.H. Meng. 3d reconstruction of the wce images by affine sift method. *IEEE 9th World Congress on Intelligent Control and Automation (WCICA)*, 2011.

[FSLE04] D. Fischer, R. Shreiber, D. Levi, and R. Eliakim. Capsule endoscopy: The localization system. *astrointestinal Endoscopy Clinics of North Amarican*, 14(1):25–31, 2004.

[FSM+01] D. Fischer, R. Shreiber, G. Meron, M. Frisch, H. Jacob, and A. Glukhovsky. Localization of the wireless capsule endoscope in its passage through the gi tract. *Gastrointestinal Endoscopy*, 53(5):AB126, 2001.

[FYP12] R. Fu, Y. Ye, and K. Pahlavan. Characteristic and modeling of human body motions for body area network applications. *Springer International Journal of Wireless Information Networks*, 19(3):219–228, 2012.

[GCF+16] Y. Geng, J. Chen, R. Fu, G Bao, and Kavek Pahlavan. Enlighten wearable physiological monitoring systems: On-body rf characteristics based human motion classification using a support vector machine. *IEEE Transactions on Mobile Computing*, 15(3):656–671, 2016.

[GCP13] Y. Geng, J. Chen, and K. Pahlavan. Motion detection using rf signals for the first responder in emergency operations: A phaser project. *2013 IEEE 24nd International Symposium on Personal Indoor and Mobile Radio Communications (PIMRC)*, 2013.

[GG05] F. Gustafsson and F. Gunnarsson. Mobile positioning using wireless networks, possibilities and fundamental limitations based on available wireless network measurements. *IEEE Signal Processing Magazine*, 22(4):41–53, 2005.

[GHDP13] Y. Geng, J. He, H. Deng, and K. Pahlavan. Modeling the effect of human body on toa ranging for indoor human tracking with wrist mounted sensor. *2013 IEEE 16th International Symposium on Wireless Personal Multimedia Communications (WPMC)*, 2013.

[GHP13] Y. Geng, J. He, and K. Pahlavan. Modeling the effect of human body on toa based indoor human tracking. *Springer International Journal of Wireless Information Networks*, 20(4):306–317, 2013.

[GHWP13] Y. Geng, J. He, Y. Wan, and K. Pahlavan. An empirical channel model for the effect of human body on ray tracing. *2013 IEEE 24nd International Symposium on Personal Indoor and Mobile Radio Communications (PIMRC)*, 2013.

[GJP10] H. Ghasemzadeh, R. Jafari, , and B. Prabhakaran. A body sensor network with electromyogram and inertial sensors: Multimodal interpretation of muscular activities. *IEEE Transactions on Information Technology in Biomedicine*, 14(2):198–206, 2010.

[GLN09] Y. Gu, A. Lo, and I. Niemegeers. A survey of indoor positioning systems for wireless personal networks. *IEEE Communications Surveys and Tutorials*, 11(1):13–32, 2009.

[GLY11] H. Gao, W. Lin, and X. Yang. A new network-based algorithm for multi-camera abnormal activity detection. *2011 IEEE International Symposium on Circuits and Systems (ISCAS)*, 2011.

[GP08] M. Garardine, , and V. Prithiviraj. Uwb localization techniques for precision automobile parking system. *IEEE 10th International Conference on Electromagnetic Interference and Compatibility (INCEMIC)*, 2008.

[GWHP13] Y. Geng, Y. Wan, J. He, and K. Pahlavan. An empirical channel model for the effect of human body on ray tracing. *2013 IEEE 24th International Symposium on Personal, Indoor and Mobile Radio Communications (PIMRC)*, 2013.

[HAP08] M. Heidari, F.O. Akgul, and K. Pahlavan. Identification of the absence of direct path in indoor localization systems. *nternational Journal of Wireless Information Networks*, 15(3-4):117–127, 2008.

[HB01] J. Hightower and G. Borriello. Location sensing techniques. *IEEE Computer*, 34(8):57–66, 2001.

[HGLX14] J. He, Y. Geng, F. Liu, and C. Xu. Cc-kf: Enhanced toa performance in multipath and nlos indoor extreme environment. *IEEE Sensors Journal*, 14(11):3766–3774, 2014.

[HGW+13] J. He, Y. Geng, W. Wan, S. Li, and K. Pahlavan. A cyber physical test-bed for virtualization of rf access environment for body sensor network. *IEEE Sensor Journal*, 13(10):3826–3836, 2013.

[HL02a] C.W. Hsu and C.J. Lin. A comparison of methods for multiclass support vector machines. *IEEE Transactions on Neural Networks*, 13(2):415–425, 2002.

[HL02b] C.W. Hsu and C.J. Lin. A simple decomposition method for support vector machines. *Springer Machine Learning*, 46(1-3):291–314, 2002.

[HLL11] M.K. Choi H.G. Lee and S.C. Lee. Motion analysis for duplicate frame removal in wireless capsule endoscope. *Proceeding of SPIE Medical Imaging*, 2011.

[HLS+10] C. Hu, M. Li, S. Song, W. Yang, R. Zhang, and M.Q.H. Meng. A cubic 3-axis magnetic sensor array for wirelessly tracking magnet position and orientation. *IEEE Sensor Journal*, 10(5):903–913, 2010.

[HMM09] C. Hu, M.Q.H. Meng, and M. Mandal. A linear algorithm for magnetic localization and orientation in capsule endoscopy. *IEEE Transactions on Magnetics*, 43(12):4096–4101, 2009.

[HPB+09] M. Hanson, H. Powell, A. Barth, K. Ringgenberg, B. Calhoun, J. Aylor, and J. Lach. Body area sensor networks: Challenges and opportunities. *Computer*, 42(1):58–65, 2009.

[HWZe11] J. He, Q. Wang, Q. Zhang, and et. al. a practical indoor toa ranging error model for localization algorithm. *2011 IEEE 22nd International Symposium on Personal Indoor and Mobile Radio Communications (PIMRC)*, 2011.

[IJZ04] R.S.H. Istepanian, E. Jovanov, and Y.T. Zhang. M-health: Beyond seamless mobility and global wireless health-care connectivity. *IEEE Transactions on Information Technology in Biomedicine*, 8(4):405–411, 2004.

[IMA+09] F. De Iorio, C. Malagelada, F. Azpiroz, M. Maluenda, C. Violanti, L. Igual, J. Vitria, and J.R. Malagelada. Intestinal motor activity, endoluminal motion and transit. *Neurogastroenterology and Mobility*, 21(12):1264–e119, 2009.

[IMGS00] G. Iddan, G. Meron, A. Glukhovsky, and P. Swain. Wireless capsule endoscopy. *Nature*, 405(6785):417–418, 2000.

[JLT09] H. Jin, H. Li, and J. Tan. Real-time daily activity classification with wireless sensor networks using hidden markov model. *2007 IEEE 29st International Conference on Engineering in Medicine and Biology Society (EMBS)*, 2009.

[JSH+08] T. Jaeckle, G. Stuber, M.H.K. Hoffmann, M. Jeltsch, B.L. Schmitz, and A.J. Aschoff. Detection and localization of acute upper and lower gastrointestinal (gi) bleeding with arterial phase multi-detector row helical ct. *European Radiology*, 18(7):1406–1413, 2008.

[KB11] A. Karargyris and N. Bourbakis. Detection of small bowel polyps and ulcers in wireless capsule endoscopy videos. *IEEE Transactions on Biomedical Engineering*, 58(10):2777–2786, 2011.

[KK09] M. Kawasaki and R. Kohno. A toa based positioning technique of medical implanted devices. *IEICE Transactions on Communications*, E92-B(2):403–409, 2009.

[KK15] A. Karargyris and A. Koulaouzidis. Odocapsule: Next-generation wireless capsule endoscopy with accurate lesion localization and video stabilization capabilities. *IEEE Transactions on Biomedical Engineering*, 19(4):326–340, 2015.

[KL09] Y. Kim and H. Ling. Human activity classification based on micro-doppler signatures using a support vector machine. *IEEE Transactions on Geoscience and Remote Sensing*, 47(5):1328–1337, 2009.

[KPM11] U. Khan, K. Pahlavan, and S. Makarov. Comparison of toa and rss based techniques for rf localization inside human tissue. *33rd Annual International Conference of the IEEE Engineering in Medicine and Biology Society (EMBS)*, 2011.

[KSM+05] A. Krieger, R.C. Susil, C. Menard, J.A. Coleman, G. Fichtinger, E. Atalar, and L.L. Whitcomb. Design of a novel mri compatible manipulator for image guided prostate interventions. *IEEE Transactions on Biomedical Engineering*, 52(2):306–313, 2005.

[KWM10] J.R. Kwapisz, G.M. Weiss, and S.A. Moore. Activity recognition using cell phone accelerometers. *ACM SIGKDD*, 12(2):74–82, 2010.

[KZS+12] R. Kumar, Q. Zhao, S. Seshamani, G. Mullin, G. Hager, and T. Dassopoulos. Assessment of crohns disease lesions in wireless capsule endoscopy images. *IEEE Transactions on Biomedical Engineering*, 59(2):355–362, 2012.

[LBM+11] B. Latre, B. Braem, I. Moerman, C. Blondia, and P. Demeester. A survey on wireless nody area networks. *Wireless Network*, 17(1):1–18, 2011.

[LCK+13] Z. Liu, J. Chen, U. Khan, B. Alkandari, and K. Pahlavan. Wideband characterization of rf propagation for toa localization of wireless video capsule endoscope inside small intestine. *2013 IEEE 24nd International Symposium on Personal, Indoor and Mobile Radio Communications (PIMRC)*, 2013.

[Lew] D. Lewis. 802.15.6 call for applications-response summary. *15-08-0407-00-0006-tg6-applications-summary.doc*.

[LGP12] S. Li, Y. Geng, and K. Pahlavan. Analysis of three-dimensional maximum likelihood algorithm for capsule endoscopy localization. *2012 5th*

International Conference on Biomedical Engineering and Informatics (BMEI), 2012.

[LL07] A. Lin and H. Ling. Doppler and direction-of-arrival (ddoa) radar for multiple-mover sensing. *IEEE Transactions on Aerospace and Electronic Systems*, 43(4):1496–1509, 2007.

[LL13] C.K. Lee and V.Y. Lee. Fall detection system based on kinect sensor using novel detection and posture recognition algorithm. *Proceeding of Springer 11th International Conference on Smart Homes and Health Telematics (ICOST)*, 2013.

[LRE10] B. Longstaff, S. Reddy, and D. Estrin. Improving activity classification for health applications on mobile devices using active and semi-supervised learning. *2010 IEEE 4th International Conference on Pervasive Computing Technologies for Healthcare*, 2010.

[LSH+09] Q. Li, J.A. Stankovic, M.A. Hanson, A.T. Barth, J Lach, and G. Zhou. Fast fall detection using gyroscopes and accelerometer-derived posture information. *Sixth International Workshop on Wearable and Implantable Body Sensor Networks*, 2009.

[LWLM11] L. Liu, C. Hu W. Liu, and M.Q.H. Meng. Hybrid magnetic and vision localization technique of capsule endoscope for 3d recovery of pathological tissues. *2011 9th World Congress on Intelligent Control and Automation (WCICA)*, 2011.

[LYA09] X. Long, B. Yin, and R.M. Aarts. Single-accelerometer-based daily physical activity classification. *2009 IEEE 31st International Conference on Engineering in Medicine and Biology Society (EMBS)*, 2009.

[MBP13] L. Mi, G. Bao, and K. Pahlavan. Design and validation of a virtual environment for experimentation inside the small intestine. *Proceedings of the 8th International Conference on Body Area Networks (BodyNETs)*, 2013.

[MF04] A.F. Molish and J.R. Foerster. Channel models for ultra-wideband personal area networks. *IEEE Wireless Communication*, 10(6):14–21, 2004.

[MFP03] A.F. Molish, J.R. Foerster, and M. Pendergrass. Channel models for ultrawideband personal area networks. *IEEE Wireless Communications Magazine*, 10(6):14–21, 2003.

[MHK06a] T.B. Moeslund, A. Hilton, and V. Kruger. A survey of advances in vision-based human motion capture and analysis. *Computer Vision and Image Understanding*, 104(2):90–126, 2006.

[MHK06b] T.B. Moeslund, A. Hilton, and V. Kruger. A survey of advances in vision-based human motion capture and analysis. *Elsever Computer Vision and Image Understanding*, 104(2-3):90–126, 2006.

[MHS01] J. Mantyjarvi, J. Himberg, and T. Seppanen. Recognizing human motion with multiple acceleration sensors. *2001 IEEE International Conference on Syste*, 2001.

[MMF+09] S. Martel, M. Mohammadi, O. Felfoul, Z. Lu, and Pouponneau P. Flagellated magnetotactic bacteria as controlled mri-trackable propulsion and steering systems for medical nanorobots operating in the human microvasculature. *International Journal of Robotics Researches*, 28(4):571–582, 2009.

[MMTP11] N. Moayeri, J. Mapar, S. Tompkins, and K. Pahlavan. Special issuse on navigation using signals of opportunity. *IEEE Wireless Magazine*, 18(4):. 2011, 2011.

[MPG14] Y. Ma, K. Pahlavan, and Y. Geng. Comparison of poa and toa based ranging behavior for rfid application. *Comparison of POA and TOA Based Ranging Behavior for RFID Application*, 2014.

[MSKS13] B. Mirmahboub, S. Samavi, N. Karimi, and S. Shirani. Automatic monocular system for human fall detection based on variations in silhouette area. *IEEE Transactions on Biomedical Engineering*, 60(2):427–436, 2013.

[Net] Body Sensor Networks. *http://ubimon.doc.ic.ac.uk/bsn/m621.html*.

[OMSJ05] C. Otto, A. Milenkovic, C. Sanders, and E. Jovanov. System architecture of a wireless body area sensor network for ubiquitous health monitoring. *Journal of Mobile Multimedia*, 1(4):307326, 2005.

[Ote05] M. Otero. Application of a continuous wave radar for human gait recognition. *Proceeding of SPIE Signal Processing, Sensor Fusion, and Target Recognition*, 2005.

[PAK+05] N. Patwari, J.N. Ash, S. Kyperountas, A.O. Hero, R.L. Moses, and N.S. Correal. Locating the nodes: Cooperative localization in wireless sensor networks. *IEEE Signal Processing Magazine*, 22(4):54–69, 2005.

[PB10] A. Pantelopoulos and N.G. Bourbakis. A survey on wearable sensor-based systems for health monitoring and prognosis. *IEEE Transactions on Systems, Man, and Cybernetics*, 40(1):1–12, 2010.

[PBM13] K. Pahlavan, G. Bao, and L. Mi. Body-slam: Simultaneous localization and mapping inside the human body. *Keynote speech in 8th International Conference on Body Area Networks (BodyNets)*, 2013.

[PBT+14] N. Patwari, L. Brewer, Q. Tate, O. Kaltiokallio, and M. Bocca. Breathfinding: A wireless network that monitors and locates breathing in a home. *IEEE Journal of Selected Topics in Signal Processing*, 8(1):30–42, 2014.

[PBY+12] K. Pahlavan, G. Bao, Y. Ye, S. Makarov, U. Khan, P. Swar, D. Cave, A. Karellas, P. Krishnamurthy, and K. Sayrafian. Rf localization for wireless video capsule endoscopy. *International Journal of Wireless Information Networks*, 19(4):326–340, 2012.

[PFJ12] M. Pourhomayoun, M. Fowler, and Z. Jin. A novel method for medical implant in-body localization. *34th Annual International Conference of the IEEE Engineering in Medicine and Biology Society (EMBS)*, 2012.

[PHP+03] N. Patwari, A.O. Hero, M. Perkins, S. Correal, and R.J. O'Dea. Relative location estimation in wireless sensor networks. *IEEE Transactions on Signal Processing*, 51(8):2137–2148, 2003.

[PHR+12] T. Ploetz, N.Y. Hammerla, A. Rozga, A. Reavis, and N. Call. Automatic assessment of problem behavior in individuals with developmental disabilities. *2012 14th ACM International Conference on Ubiquitous Computing (Ubicomp)*, 2012.

[Poo94] H.V. Poor. An introduction to signal detection and estimation. *Springer Science and Business Media*, 1994.

[Pop10] R. Poppe. A survey on vision-based human action recognition. *Elsever Image and Vision Computing*, 28(6):976–990, 2010.

[PPK12] S. Pranay, K. Pahlavan, and U. Khan. Accuracy of localization system inside human body using a fast fdtd simulation technique. *Medical Information and Communication Technology (ISMICT)*, 2012.

[PXM02] K. Pahlavan, Li Xinrong, and J. P. Makela. Indoor geolocation science and technology. *IEEE Communications Magazine*, 40(1):112–118, 2002.

[PYFK12] K. Pahlavan, Y. Ye, R. Fu, and U. Khan. Challenges in channel measurement and modeling for rf localization inside the human body. *International Journal of Embedded and Real-Time Communication Systems*, 3(3):1–20, 2012.

[RMSAR11] C. Rougier, J. Meunier, A. St-Arnaud, and J. Rousseau. Robust video surveillance for fall detection based on human shape deformation. *IEEE Transactions on Circuits and Systems for Video Technology*, 21(5):611–622, 2011.

[RXN+11] F. Della Rosa, L. Xu, J. Nurmi, M. Pelosi, C. Laoudias, and A. Terrezza. Hand-grip and body-loss impact on rss measurements for localization of mass market devices. *International Conference on Localization and GNSS (ICL-GNSS)*, 2011.

[SAV07] T. Shah, S.M. Aziz, and T. Vaithianathan. Development of a tracking algorithm for an in-vivo rf capsule prototype. *International Conference on Electrical and Computer Engineering (ICECE)*, 2007.

[SC13] D.L. Streiner and J. Cairney. What's under the roc? an introduction to receiver operating characteristic curves. *A Guide for the Statistically Perplexed: Selected Readings for Clinical Researchers*, 2013.

[SHK+05] K. Schulmann, S. Hollerbach, K. Kraus, J. Willert, T. Vogel, G. Moslein, C. Pox, M. Reiser, A. Reinacher-Schick, and W. Schmiegel. Feasibility and diagnostic utility of video capsule endoscopy for the detection of small bowel polyps in patients with hereditary polyposis syndromes. *The American Journal of Gastroenterology*, 100(1):23–27, 2005.

[SJ04] A. Sixsmith and N. Johnson. A smart sensor to detect the falls of the elderly. *IEEE Pervasive Computing*, 3(2):42–47, 2004.

[SJL+14] H. Sun, Z. Jin, X. Li, J. Qian, J. Yu, F. Zhu, and H. Zhu. Detection and localization of active gastrointestinal bleeding with multidetector row computed tomography angiography: A five-year prospective study in one medical center. *Journal of Clinical Gastroenterology*, 46(1):1–11, 2014.

[SSK13] J. Shotton, T. Sharp, and A. Kipman. Real-time human pose recognition in parts from single depth images. *Communications of the ACM*, 56(1):116–124, 2013.

[SSP08] F. Soldovieri, R. Solimene, , and G. Prisco. A multiarray tomographic approach for through-wall imaging. *IEEE Transactions on Geoscience and Remote Sensing*, 46(4):1192–1199, 2008.

[SSS+14] S. Sigg, M. Scholz, S. Shi, Y. Ji, and M. Beigl. Rf-sensing of activities from non-cooperative subjects in device-free recognition systems using ambient and local signals. *IEEE Transactions on Mobile Computing*, 13(4):907–920, 2014.

[SVQ+10] M. Simi, P. Valdastri, C. Quaglia, A. Menciassi, and P. Dario. Design, fabrication, and testing of a capsule with hybrid locomotion for gastrointestinal tract exploration. *IEEE/ACM Transactions on Mechatronics*, 15(2):170–180, 2010.

[SW10] Y. Shen and M.Z. Win. Fundamental limits of wideband localization part i: A general framework. *IEEE Transactions on Information Theory*, 56(10):4956–4980, 2010.

[SYGP12] P. Swar, Y. Ye, K. Ghaboosi, and K. Pahlavan. On effect of transmit power variance on localization accuracy in wireless capsule endoscopy. *2012 IEEE Wireless Communications and Networking Conference (WCNC)*, 2012.

[SYHT09] K. Sayrafian, W. Yang, J. Hagedorn, and J. Terrill. A statistical path loss model for medical implant communication channels. *2009 IEEE 20th International Symposium on Personal, Indoor and Mobile Radio Communications (PIMRC)*, 2009.

[SYL05] L. Song, C. Yu, and Q. Liu. Through-wall imaging (twi) by radar: 2-d tomographic results and analyses. *IEEE Transactions on Geoscience and Remote Sensing*, 43(12):2793–2798, 2005.

[TAH+12] T.D. Than, G. Alici, S. Harvey, H. Zhou, and W. Li. Concept and simulation study of a novel localization method for robotic endoscopic capsules using multiple positron emission markers. *Medical Physics*, 41(1):31–41, 2012.

[TAZL12] T.D. Than, G. Alici, H. Zhou, and W. Li. A review of localization systems for robotic endoscopic capsules. *IEEE Transactions on Biomedical Engineering*, 59(9):2387–2399, 2012.

[TDM11] S. Thuraiappah, H. David, and H. Mark. Wasp: A system and algorithms for accurate radio localization using low-cost hardware. *IEEE Transactions on Systems, Man, and Cybernetics, Part C: Applications and Reviews*, 41(2):211–222, 2011.

[TFaNTM10] C. Tachtatzis, F. Franco, D. Tracey adn N. Timmons, and J. Morrison. An energy analysis of ieee 802.15.6 scheduled access modes. *IEEE GLOBECOM Workshops*, 2010.

[Tg303] IEEE 802.15 Tg3a. Channel model for high rate wireless personal area network. 2003.

[Tg610] IEEE 802.15 Tg6. Draft of channel model for body area network. 2010.

[Tre68] H.L. Van Trees. Estimation and modulation theory - part i. *Weily*, 1968.

[VRTH09] M.A.E. Valderrama, L.M. Roa, J.R. Tosina, and D.N. Hernandez. Design and implementation of a distributed fall detection system-personal server. *IEEE Transactions on Information Technology in Biomedicine*, 13(6):874–881, 2009.

[VWG+03] M. Vossiek, L. Wiebking, P. Gulden, J. Wieghardt, C. Hoffmann, and P. Heide. Wireless local positioning. *IEEE Microwave Magazine*, 4(4):77–86, 2003.

[WDX07] J. Wu, L. Dong, and W. Xiao. Real-time physical activity classification and tracking using wearable sensors. *2007 IEEE 6th International Conference on Information*, 2007.

[WFY+11] Y. Wang, R. Fu, Y. Ye, U. Khan, and K. Pahlavan. Performance bounds for rf positioning of endoscopy camera capsules. *2011 IEEE Topical Conference on Biomedical Wireless Technologies, Networks, and Sensing Systems (BioWireleSS)*, 2011.

[WHP+08] X. Wu, W. Hou, C. Peng, X. Zheng, X. Fang, and J. He. Wearable magnetic locating and tracking system for mems medical capsule. *Sensors and Actuators A: Physical*, 141(2):432–439, 2008.

[WTK+09] Q. Wang, T. Tayamachi, I. Kimura, , and J. Wang. An on-body channel model for uwb body area communications for various postures. *IEEE Transactions on Antennas and Propagation*, 57(4):991–998, 2009.

[WWL12] J. Wu, G. Wang, and G.Y. Li. Frequency-domain on-off accumulative transmission over frequency-selective fading channels. *2012 IEEE International Conference on Communications (ICC)*, 2012.

[WWZ+13] G. Wang, J. Wu, G. Zhou, , and G.Y. Li. Collision-tolerant media access control for asynchronous users over frequency-selective channels. *IEEE Transactions on Wireless Communications*, 12(10):5162–5171, 2013.

[XFM13] C. Xu, B. Firner, and R.S. Moore. Scpl: Indoor device-free multi-subject counting and localization using radio signal strength. *ACM/IEEE International Conference on Information Processing in Sensor Networks (IPSN)*, 2013.

[YKA+11] Y. Ye, U. Khan, N. Alsindi, R. Fu, and K. Pahlavan. On the accuracy of rf positioning in multi-capsule endoscopy. *2011 IEEE 22nd International Symposium on Personal, Indoor and Mobile Radio Communications (PIMRC)*, 2011.

[YKN10] S. Yun, K. Kim, and S. Nam. Outer-wall loop antenna for ultra-wideband capsule endoscope system. *IEEE Antennas and Wireless Propagation Letters*, 9(1):1135–1138, 2010.

[YPB+14] Y. Ye, K. Pahlavan, G. Bao, P. Swar, and K. Ghaboosi. Comparative performance evaluation of rf localization for wireless capsule endoscopy applications. *International Journal of Wireless Information Networks (IJWIN)*, 21(3):208–222, 2014.

[YSPG12] Y. Ye, P. Swar, K. Pahlavan, and K. Ghaboosi. Accuracy of rss-based rf localization in multi-capsule endoscopy. *International Journal of Wireless Information Networks (IJWIN)*, 19(3):229–238, 2012.

[ZB12] X. Zheng and G. Bao. The performance of simulated annealing algorithms for wi-fi localization using google indoor map. *IEEE 76th Vehicular Technology Conference (VTC)*, 2012.

[ZMNZ10] S. Zhang, P. McCullagh, C. Nugent, and H. Zheng. Activity monitoring using a smart phone's accelerometer with hierarchical classification. *2010 IEEE 6th International Conference on Intelligent Environments (IE)*, 2010.